NUCLEATION INHIBITION AND ENHANCEMENT IN CHEMICAL VAPOR DEPOSITION

BY

ZHEJUN ZHANG

DISSERTATION

Submitted in partial fulfillment of the requirements
for the degree of Doctor of Philosophy in Materials Science and Engineering
in the Graduate College of the
University of Illinois at Urbana-Champaign, 2020

Urbana, Illinois

Doctoral Committee:

Professor John R. Abelson, Chair
Professor Gregory S. Girolami
Associate Professor Qing Cao
Assistant Professor Jessica A. Krogstad

ABSTRACT

Area selective deposition (ASD) is becoming increasingly attractive as a bottom-up approach to nanomanufacturing. Most ASD processes developed so far concern selective deposition of metal on metal (i.e., not on non-metallic surfaces) or oxide on oxide (i.e., not on metallic surfaces), but nanomanufacturing also demands other film-substrate combinations such as deposition of metal on one oxide vs. another oxide or a metal surface.

In this dissertation, I report one example of ASD that affords these new capabilities: chemical vapor deposition (CVD) of cobalt from $Co_2(CO)_8$ is fast on some oxides (Al_2O_3) but slow on others (SiO_2). We also show that the addition of ammonia as an inhibitor improves the selectivity between oxides: a coflow of ammonia strongly inhibits nucleation on SiO_2 (an acidic oxide) but has negligible effect on the nucleation and growth on Al_2O_3 (a basic oxide). We also show that the cobalt deposition process can, in some cases, be tuned to enable nucleation of Co on metal but not on oxide, or Co on oxide but not on metal.

If, however, film growth is required on a relatively unreactive surface (e.g., one otherwise used for nongrowth), then the nucleation step will be kinetically difficult: a relatively small areal density of islands will form over an extended period of time. As a consequence, islands of different sizes populate the surface, and full coalescence (coverage of the substrate) occurs only when a relatively large thickness has been deposited, and the morphology is rough due to the distribution of island heights. To enhance film smoothness on unreactive substrates, I demonstrate that the sequential use of (i) a self-limiting substrate pretreatment by tetrakis-(dimethylamino)metal (TDMA-M) molecules (M = V, Hf, or Ti), followed by (ii) growth inhibition using a co-flow of ammonia during film growth of cobalt. The film grown by the combination of steps has a much smaller roughness than either step alone.

I also investigate the nucleation of HfB_2 from $Hf(BH_4)_4$ on Al_2O_3 vs. on SiO_2 substrates. In both cases nucleation begins rapidly. However, on Al_2O_3 a high density of nuclei forms, and these nuclei rapidly coalesce into a smooth continuous film; by contrast, on SiO_2 the island density remains smaller and coalescence occurs at larger film thickness. The method of pretreatment from self-limiting adsorption of tetrakis(dimethylamino)hafnium can increase nuclei density, and thus, speed up nucleation and reduce film roughness.

Chemical design of a CVD precursor can be used to afford rapid nucleation but slow film growth, thus, smooth ultra-thin films. In a collaborative effort with S. Liu in the group of G. S. Girolami, I demonstrate the CVD of smooth platinum films using the newly-synthesized $Pt[CH_2CMe_2CH_2CH=CH_2]_2$ precursor. This molecule has a rapid nucleation, which is the consequence of the availability of low barrier C-H activation pathways, and slow growth rate due to the formation of carbon-containing species that passivate the Pt surface.

I used reflection IR absorption in real time to analyze the steady-state population of adsorbates during CVD. This information is needed to fully understand the surface kinetics that govern conformal and superconformal growth, as well as nucleation inhibition and enhancement. We show that use of a metal substrate used at high angle of incidence provides enough signal enhancement in p-polarization to observe sub-monolayer coverages. The intrinsic cancellation of the absorption signal in s-polarization means that the unwanted absorption due to gas phase molecules in the beam path, and molecules adsorbed on the IR chamber windows, can be cancelled out by subtraction of the p- and s- signals.

In the last section, I demonstrate a superconformal process for cobalt deposition by adding a consumable inhibitor. The films are, however, contaminated by incorporation of the inhibitor molecules. Therefore, I propose an innovative approach that can potentially achieve superconformal growth of contamination-free films. This method requires two precursors that deposit the same film, but with quite different rates of adsorption and reaction.

To my parents

ACKNOWLEDGEMENT

First, I would like to express my sincere gratitude to my Ph.D. adviser Professor John R. Abelson for his help and support throughout my Ph.D. program. He always gave me insightful suggestions on my research and help me overcome many difficulties. I am also incredibly grateful to Prof. Gregory S. Girolami for his valuable discussions and I learned a lot from him. Besides, I like to thank my other preliminary exam committee members Prof. Qing Cao and Prof. Jessica Krogstad for comments, suggestions and questions, which built a stage for further progress in my research.

I also like to acknowledge our chemistry colleagues at Prof. Girolami group, especially Dr. Sumeng Liu for helpful discussions and supplying me the precursors whenever I needed.

I am thankful to all my previous and current group members, Dr. Pengyi Zhang, Dr. Elham Mohimi, Dr. Tushar Talukdar, Xiaoqing Chu and Kinsey Canova for all collaborative research work and their assistance in lab work.

Ex-situ materials characterization was carried out in part in the Frederick Seitz Materials Research Laboratory Central Facilities. Special thanks to Dr. Rick Haasch, Dr. Mauro Sardela, Doug Jeffers, Dr. Tao Shang, Dr. Fubo Rao, Dr. Julio Soares, Dr. Kathy Walsh, and Dr. Timothy Spila.

I also like to express my sincere gratitude to my parents and Qun Li for always being there for me, supporting and believing in me. I am highly indebted to all of them.

At last, I would like to thank everyone who are working hard to fight the COVID-19 pandemic, especially those in the front lines.

TABLE OF CONTENTS

CHAPTER 1

OVERVIEW

1.1 Introduction

1.1.1 Area-selective deposition: selective nucleation inhibition

Many nanoscale electronic devices are fabricated by a top-down approach involving blanket thin film deposition followed by photolithographic patterning and etching steps. However, as feature sizes shrink towards or below 10 nm, edge placement errors in photolithography make it difficult to avoid unacceptable misalignments between layers. For this reason, bottom-up patterning methods that automatically result in pattern registry are becoming increasingly attractive. One such bottom-up method is area-selective deposition (ASD), in which, for example, growth occurs on metallic surfaces but not on dielectric surfaces [1]. As a result, ASD reduces production costs by obviating the need for additional patterning and etching steps. Another potential application of ASD is in dual damascene metallization, which requires void-free fill of vias with high aspect ratio. ASD can meet this need by bottom-up growth, which occurs when film nucleates on the bottom of the feature but not on the sidewalls [2].

ASD is achieved either by inherent selectivity between substrates, or selective surface modification to inhibit nucleation on some substrates but not others. Inherent selectivity relies on kinetic differences in the adsorption of precursors or co-reactants due to the chemistry of the substrate surface. For example, $TiCl_4$ precursors preferentially react with -OH ligands on SiO_2 but do not react on H-terminated Si, which affords ASD of TiO_2 on hydroxylated SiO_2 against H-terminated Si [3]. Another example is ASD on noble metals against oxide surfaces: noble metals can catalyze dissociative chemisorption of precursors or co-reactants, while adsorption on oxides occurs relatively slowly [4-7].

Surface modification is the most extensively studied method for ASD. Typically, self-assembled monolayers (SAMs) are selectively adsorbed on substrates. For example, SAMs with

thiol end groups selectively adsorb on metal substrates [8,9] while SAMs with silane selectively adsorb on oxides [10]. They sterically block the surface and the tail group of CH_3 or CF_3 in SAMs is not reactive to incoming precursors and reactants; thus, the surface reactivity is deactivated by SAMs. Application of SAMs is mostly done by wet chemistry and the process may take 24 hours [9], which is not practical for mass production. Therefore, vapor-phase SAMs have been developed to address these issues [11,12]. An alternate approach is to expose the surface to small molecules with high vapor pressure, such as acetylacetone [13], to inhibit nucleation on certain oxide surfaces.

However, there are still many challenges for ASD. The first problem is to obtain high selectivity. No deposition process is area-selective indefinitely: even on the most unreceptive surfaces, nucleation and growth will eventually occur. Besides, there are always defects and impurities on non-growth surface, on which nucleation may occur. Many efforts have been made to improve selectivity. For example, it was discovered [14] that SAMs with a larger number of carbon atoms tend to have a better inhibition effect, i.e., better selectivity. Regeneration of SAMs during growth has been investigated to minimize defects that apparently form due to the exposure to precursors [8,13]. Another approach is to add a correction step by periodically etching away unwanted nuclei on the non-growth substrate [15,16].

The second challenge is lateral broadening (“mushroom” growth). Growth from chemical vapor deposition (CVD) or atomic layer deposition (ALD) is relatively isotropic, thus, films will not only grow vertically but also laterally. No solution has been reported yet, though it is plausible to make the growth process more anisotropic or to have an anisotropic etching step.

The third challenge is that some film-substrate combinations do not appear to offer a route for selective growth. Many studies have been reported that afford metal-on-metal or oxide-on-oxide selectivity, however, other combinations are barely explored (except for one report [13]), such as metal deposition on oxide against a metal substrate, or deposition on a specific oxide in the presence of other oxide surfaces.

Finally, other issues can cause complexity. For example, substrate history (whether the substrate was exposed to photoresist, surface cleanliness, etc.) can affect nucleation and selectivity [17]. A thorough understanding of the condition of the substrate surface is needed.

In this dissertation, a new film-substrate combination for ASD is reported. I investigate the ASD of cobalt on different oxides, where the acidity of surface hydroxyl groups varies from acidic to basic, using the precursor dicobalt octacarbonyl, $Co_2(CO)_8$. Nucleation from $Co_2(CO)_8$ is somewhat faster on basic oxides such as Al_2O_3 than on acidic oxides such as SiO_2. Due to different acidity, the precursor has different adsorption and reaction rates. Ammonia is added as a co-flow during the deposition process to improve the selectivity for Co growth. The choice of ammonia as a selectivity enhancer was made because we have recently shown that this molecule enhances metal vs. oxide ASD from $Mo(CO)_6$ [18]. A coflow of ammonia has negligible effect on the nucleation rate for deposition on Al_2O_3 but it strongly inhibits nucleation and growth on SiO_2. The net result is that ammonia enables highly selective ASD of Co from $Co_2(CO)_8$ on some oxide surfaces over others. In addition, the cobalt deposition process can in some cases be tuned to enable nucleation of Co on metal but not on oxide, or Co on oxide but not on metal, by taking advantage of thin native oxide, or ozone-generated oxide, overlayers which block nucleation as well as thick oxides, and can later be removed by reduction or etching to restore a metallic surface.

1.1.2 Ultra-smooth metallic films on oxide: nucleation enhancement and growth inhibition

When a film is deposited on a relatively unreactive substrate, the surface roughness can be several nm or larger; examples include the growth of HfB_2 (a metallic ceramic barrier layer) [19] or cobalt [20,21] on SiO_2. Roughness is amplified when the nucleation process is slow or occurs with low areal density: the nuclei which form early in the process grow relatively tall before the surface reaches full coverage (coalescence). Processes that can achieve small roughness are greatly desired to obtain continuous films, especially when films must be very thin for the given application.

Several methods have been shown to improve roughness. (i) A material with a reactive surface (often metallic), such as TiN [22], can be pre-deposited to serve as a ‘nucleation layer’. This presupposes that the chosen material nucleates well on the oxide surface to afford a reasonably smooth thin film. However, this approach has disadvantages in microelectronics fabrication: the nucleation layer consumes part of the width of vias and trenches, which increases

the overall electrical resistance of these interconnects. It must also be possible to grow the layer conformally in deep features, and under conditions (e.g., substrate temperature) that are compatible with subsequent processing steps. Alternatively, the starting surface can be pretreated by (ii) a flux of molecules in vapor [23,24] or liquid [25] or (iii) exposure to energetic particles, such as plasma [26-28] to enhance nucleation and thus reduce roughness.

It is also possible to smoothen thin films by decreasing the film growth rate without substantially altering the nucleation rate on the starting substrate. This is accomplished by adding a flow of molecular inhibitor to the flow of CVD precursor; the inhibitor is selected because it binds weakly to substrate but more strongly to the surface of the deposited film, which affords the desired differential effect. This method has been reported to afford higher nucleation density and smoother films in a few systems: HfB_2 grown from $Hf(BH_4)_4$ using NH_3 as the inhibitor [19], Cu grown from Cu(hfac)(VTMS) using VTMS as the inhibitor [29], Ru grown from $Ru(EtCp)_2$ using CH_3I or C_2H_5I as the inhibitor [30-32] and Ru grown with $Ru_3(CO)_{12}$ using CO as the inhibitor [33].

Kinetically, the development of initial roughness can be described in terms of the area density of possible nucleation sites, the time dependence of film nucleation (rate of nucleation), and the rate of film growth on those nuclei. The smoothest film results when the precursor has a high probability of reaction with the substrate surface, but a low probability of reacting with the surface of the deposited material, i.e., *the ratio of the nucleation rate to the growth rate is large*. Under those conditions, a high areal density of small nuclei form on the substrate, then growth of these nuclei (possibly accompanied by continued nucleation) leads to coalescence and smoothing within the first few nm of deposited thickness. Similar ideas were reported in the literature for electrodeposition [34,35] and casting [36]. In the area of vapor phase deposition, evidence concerning the ratio of rates on the film morphology has been obtained either by increasing the nucleation rate [23-28] or reducing the growth rate [19,29-33]. We are not aware of any work that has explicitly altered both the nucleation rate and the growth rate.

Here I report a CVD method to grow extraordinarily smooth cobalt films on SiO_2 substrates. We show that the sequential use of nucleation enhancement (by pretreatment of tetrakis(dimethylamino)metal (TDMA-M) molecules, M=V, Hf, Ti) and growth inhibition (by ammonia coflow) dramatically reduces the roughness, smaller than is obtained using either

approach alone. Pretreatment of TDMA-M can also enhance nucleation of HfB_2 on SiO_2 from $Hf(BH_4)_4$.

It is also possible to design a CVD precursor such that the probable ligand reactions tend to increase the nucleation rate and reduce growth rate. A new platinum precursor, cis-bis(η1,η2-2,2-dimethylpent-4-en-1-yl)platinum (PtC5), was developed in the group of Professor G. S. Girolami with the intent of growing ultra-smooth films. I have tested this precursor and report its favorable properties in terms of the nucleation and growth rates.

1.1.3 Infrared reflection spectroscopy of adsorbed intermediates during chemical vapor deposition of oxides

Infrared spectroscopy (IR) offers an experimental means to detect the presence and population of adsorbed species, including reaction intermediates, on a film growth surface. Such information can test hypotheses about the microscopic mechanisms, for example, that reductions in film growth rate are due to site blocking by a co-reactant or an inhibitor. IR has been extensively used for ALD. However, it is experimentally more challenging to monitor a CVD process *in-situ* and in real time because the adsorbed quantities are sub-monolayer, there is unwanted IR absorption due to a partial pressure of precursor molecules in the chamber (and thus in the IR beam path) and adsorbed on the IR windows. Besides, film growth is a dynamic process, which means that the optical response of the film-on-substrate combination may change during the IR measurement. For these reasons, the IR system should (i) have a sub-monolayer sensitivity, (ii) be able to distinguish contributions from the gas phase, windows and surface, and (iii) have a nearly constant sensitivity. Real-time IR has been used for CVD, but only for gas phase species [37,38]. We are not aware of any report that has monitored the CVD growth surface by IR in real time. Our group previously used FTIR in real time to analyze reactive sputter deposition of hydrogenated amorphous silicon films [39-42]. In that system, the IR modes of gas phase species do not overlap with those in the film, which eliminates problem (i); and we used a carefully designed multilayer substrate to eliminate problem (ii).

Since the pioneering work of Greenler [43] for infrared reflection absorption spectroscopy (IRRAS), this technique has been widely used to study thin films [44], gas-liquid interfaces [45], Langmuir-Blodgett monolayers [46] or solution-based surface reaction and

adsorption [47] on metallic substrates. It employs polarized light at grazing incidence: s-polarized light gives no surface electric field, thus no surface absorption, while in p-polarization the superposition of incident and reflected beams enhances the surface electric field and thus the surface absorption. Note that absorption from windows and gas phase is not polarization-dependent. Thus, subtraction of s-polarized signal from p-polarized signal gives pure surface absorption. This approach has been used for solution-based surface reactions [47] to remove absorption from the beam path in the solution and for ultra-thin films to remove background instability [44]. For these reasons, I investigate, theoretically and experimentally, the feasibility of applying real-time IRRAS from a planar metallic substrate to detect the identity and concentration of surface adsorbates during CVD of oxide films.

1.1.4 Superconformal deposition

Void-free filling of recessing features, such as trenches and vias, is necessary in microelectronic fabrication, such as interconnects [44] and shallow trench isolation [45] in integrated circuits. The idea of superconformal deposition [46-48] can be utilized so that deposition at the bottom of the structure is faster than that at the top, which creates a V-shaped taper that favors seamless filling in a trench [49].

I demonstrate a superconformal process for CVD of cobalt from a single source precursor, $Co_2(CO)_8$, together with a consumable inhibitor, tetrakis(dimethylamino)vanadium (TDMAV). Growth from $Co_2(CO)_8$ is typically not conformal due to the high reaction probability of the precursor. Using coflow of TDMAV, the growth is superconformal but contaminated by V, and presumably by C and N from ligand decomposition.

To mitigate the contamination issue, I also propose a new method, using two CVD precursors, which should afford superconformal growth of contamination-free films. One precursor adsorbs strongly but reacts relatively slowly; the other precursor adsorbs less strongly but reacts more rapidly. The strongly adsorbing precursor inhibits the overall growth rate near to the opening, but it is progressively consumed in depth by film growth on the trench sidewalls. Consequently, the inhibition effect diminishes and fast growth from the second precursor affords an increase in growth rate towards the bottom. By using two precursors that deposit the same

film, contamination is avoided. Superconformal growth can occur even when each precursor, if used alone, affords sub-conformal coverage.

1.2 Chapter Summaries

CHAPTER 2

We describe the enhancement of area-selective chemical vapor deposition of cobalt films on one oxide surface over another from the precursor $Co_2(CO)_8$ by addition of the nucleation inhibitor ammonia (NH_3). In the absence of an NH_3 co-flow, the $Co_2(CO)_8$ precursor exhibits a weak intrinsic selectivity: at 70 °C, Co nucleates quickly on Al_2O_3 but more slowly on SiO_2. The addition of an NH_3 co-flow, however, greatly amplifies the selectivity between different oxide surfaces. Thus, NH_3 significantly inhibits nucleation on acidic oxides such as SiO_2 and WO_3, but has little effect on more basic oxides such as Al_2O_3, HfO_2, and MgO. Comparison of growth on fully hydroxylated and dehydroxylated SiO_2 suggests that hydroxyl groups are the nucleation sites that are affected by the addition of NH_3. The mechanism of nucleation appears to be disproportionation of $Co_2(CO)_8$ to Co^{2+} (the intermediate that leads to nucleation) and $Co(CO)_4^-$: this disproportionation occurs readily on basic oxides but not on acidic oxides. Addition of NH_3 has little effect on Co nucleation the basic oxides, probably because ammonia binds poorly to such surfaces, but NH_3 greatly retards nucleation on acidic oxides such as SiO_2; we propose that the latter result is either a site blocking effect or the result of conversion of Co^{2+} to inactive $Co(NH_3)_x^{2+}$ species. Nucleation of cobalt is facile on gold (a very unreactive metal) even in the presence of NH_3. We have found, however, that deposition of Co on tungsten can be inhibited by exposing the surface briefly to ozone; no deposition occurs on the resulting thin oxide overlayer from $Co_2(CO)_8$ in the presence of NH_3. In other words, this thin oxide overlayer affords the same selective inhibition behavior as seen on bulk WO_3. In this way, both metal-on-metal and metal-on-oxide selectivity can be achieved. Cobalt films grown in the absence and presence of ammonia have resistivities of 11–20 and 15–25 μΩ·cm, respectively.

- "Area-selective chemical vapor deposition of cobalt from dicobalt octacarbonyl: Enhancement of dielectric-dielectric selectivity by adding a coflow of ammonia", Z. V.

Zhang, S. Liu, G. S. Girolami, J. R. Abelson, Journal of Vacuum Science & Technology A 38, 033401 (2020).

CHAPTER 3

Very smooth thin films of Co are deposited on SiO_2 by CVD from the precursor dicobalt octacarbonyl $Co_2(CO)_8$ by augmenting the process conditions in two ways: (1) pretreating the surface to promote nucleation, and (2) adding a coflow of a growth inhibitor. The surface pretreatment involves exposure of the SiO_2 surface at 70 °C to a tetrakis(dimethylamino)metal complex $M(NMe_2)_4$, where M = V, Ti, or Hf. This pretreatment affords a self-limiting, sub-monolayer coverage of a metal-containing intermediate. When the pretreated surface is then exposed to 0.025 mTorr of the $Co_2(CO)_8$ precursor, nucleation occurs with essentially no delay to afford a high density (1×10^{12} /cm^2) of nanoscale islands; the rms surface roughness for a 1.1~1.3 nm thick Co film is 1.0 nm. Comparisons show that the $M(NMe_2)_4$ pretreatment has three benefits: it accelerates the nucleation process, it increases the nucleation density by about a factor of 3, and it reduces the surface rms roughness of the ~1.1-1.3 nm thick film by about a factor of 2. The rms surface roughness of the ~1.1-1.3 nm thick film can be further reduced to only 0.3 nm by adding up to 4 mTorr of ammonia NH_3 to the feed gas, along with the $Co_2(CO)_8$ precursor. Ammonia serves as a growth inhibitor that reduces the steady-state growth rate of Co by a factor of 4; the slower growth means that more nucleation can occur before coalescence of islands into a continuous film takes place. These process conditions can be adjusted to turn off the deposition of cobalt on SiO_2: if the pretreatment step is omitted and ammonia pressures of 4 mTorr are used, nucleation is delayed for tens of minutes. These conditions could be employed for the area-selective deposition of cobalt on other (non-SiO_2) surfaces.

- "Ultra-smooth cobalt films on SiO_2: CVD using a nucleation promoter and a growth inhibitor", Z. V. Zhang, S. Liu, G. S. Girolami, J. R. Abelson, *in preparation*.

CHAPTER 4

We demonstrate that growth of HfB_2 by CVD from $Hf(BH_4)_4$ is inherently selective on Al_2O_3 against SiO_2: a 10.4-nm film is grown on Al_2O_3 in 16 min while only 0.07 nm of HfB_2 on SiO_2 in 18 min. We discovered that nucleation occurs readily on both SiO_2 and Al_2O_3. However, Al_2O_3 surface has a higher density of nuclei and HfB_2 islands coalesce to form continuous films

quickly, followed by fast static growth on HfB_2 itself. Due to sparse nucleation, it takes longer for islands to grow and coalesce on SiO_2, and thus, growth is slower. Sparse nucleation also leads to rougher films with broader height distribution functions on SiO_2. The rms roughness is 3.8 nm on SiO_2 and 1.3 nm on Al_2O_3 for samples with a bulk equivalent thickness of ~ 0.5 nm. The difference is thought to be the different basicity of hydroxyl groups on oxide surfaces. When growth on SiO_2 surface is desired, a method of pretreatment from self-limiting adsorption of tetrakis(dimethylamino)hafnium can increase nuclei density, and thus, speed up nucleation. Rms roughness is reduced to from 3.8 nm to 1.7 nm. By contrast, pretreatment on Al_2O_3 slightly increases the film roughness.

- "CVD of HfB_2 from $Hf(BH_4)_4$: area selective deposition on Al_2O_3 against SiO_2 and effect of pretreatment by $Hf[(CH_3)_2N]_4$ on nucleation", Z. V. Zhang, S. Liu, G. S. Girolami, J. R. Abelson, *in preparation.*

CHAPTER 5

We investigate the growth of platinum on various substrates from a newly-design precursor, $Pt[CH_2CMe_2CH_2CH=CH_2]_2$. The deposition, requiring no co-reactant, has no nucleation delay and films are smooth. For example, the film grown on an Al_2O_3 substrate at 330 °C has a root-mean-square roughness of 1.7 nm for a 13-nm film (from SEM), although the films are contaminated by 50 at.% of carbon, the resistivity is high at 830 μΩ·cm and the growth rate is slow. These issues can be mitigated by introducing a remote oxygen plasma. However, the films we obtained still have a high resistivity and presumably high carbon contamination, probably due to a limited flux of atomic oxygen in our plasma source. Conformality of the process needs improvement, presumably attributed to the growth inhibition from by-products.

- "Platinum ω-Alkenyl Compounds. Synthesis and Characterization of $Pt[CH_2CMe_2CH_2CH=CH_2]_2$ and Related Compounds and Their Use as Chemical Vapor Deposition Precursors", S. Liu, Z. V. Zhang, D. Gray, L. Zhu, J. R. Abelson, and G. S. Girolami, *in preparation*.

CHAPTER 6

Real-time infrared reflection absorption spectroscopy is used to measure the surface coverage of adsorbed intermediates during chemical vapor deposition of HfO_2 from tetrakis-(dimethylamino)hafnium and water with the addition of magnesium N, N-dimethylaminodiboranate as a molecular growth inhibitor. Theoretical modeling of IR reflection from a planar, metal-coated substrate shows that p-polarized light at high angle of incidence has a much higher sensitivity for adsorbates than s-polarized light. The theoretical peak sensitivity occurs at a glancing angle of ~ 88°, however, it is a strong function of the thickness and refractive index of deposited oxide. We operate at a lower angle of 60° because, despite the lower sensitivity, the data are independent of the surface oxide. The absorption of precursor molecules in the gas phase and adsorbed on windows is cancelled by subtraction of p-s spectra. The addition of the inhibitor during growth causes a drop in the IR absorption from the precursor that correlates with the observed drop in HfO_2 growth rate.

- "Infrared reflection spectroscopy of adsorbed intermediates during chemical vapor deposition of oxides", Z. V. Zhang, G. S. Girolami, J. R. Abelson, *in preparation.*

CHAPTER 7

We demonstrate a superconformal growth of cobalt films from $Co_2(CO)_8$ by using a consumable inhibitor. Growth from $Co_2(CO)_8$ at 70 °C is not conformal in the absence of a growth inhibitor. Tetrakis(dimethylamino)hafnium is then co-flowed as the inhibitor and reduce the growth rate from 2.7 nm/min to 0.25 nm/min. Adsorption of TDMAV is irreversible, meaning TDMAV is consumed on the sidewalls of the trench in cobalt growth. The growth is superconformal and V-shaped coating profile is obtained with the angle of 4°, which is enough even for a conformal process to fill the trench free of defect. The diffusion-reaction model shows that consumable inhibitors with high sticking probability can render the growth superconformal. Also, the sticking coefficient of TDMAV is approximated as 20 %. The films grown in the presence of TDMAV contain 6% of vanadium and the resistivity is high at 125 μΩ·cm. Using diffusion-reaction model, we propose when two precursors that deposit the same film, have very different rates of adsorption and reaction, superconformal growth can be obtained using a coflow of the two precursors. This method would presumably allow growth of contamination-free films.

- "Superconformal deposition by consumable-inhibitor method and two-precursor method: experiment and modeling", Z. V. Zhang, G. S. Girolami, J. R. Abelson, *in preparation.*
- "Seamless trench filling by chemical vapor deposition of a metallic alloy from two precursors", K. Canova, Z. V. Zhang, G. S. Girolami, J. R. Abelson, *in preparation*.

CHAPTER 8

Promising future work, including proof-of-concept work are discussed.

1.3 References

1. A. J. M. Mackus, A. A. Bol, and W. M. M. Kessels, "The use of atomic layer deposition in advanced nanopatterning," *Nanoscale* **6,** 10941-60 (2014).

2. J. F. Zheng, P. Chen, T. H. Baum, R. R. Lieten, W. Hunks, S. Lippy, A. Frye, W. M. Li, J. O'Neill, J. Xu, J. Zhu, J. Bao, V. Machkaoutsan, M. Badaroglu, G. Yeap, G. Murdoch, J. Bommels, Z. Tokei, and Ieee, *Selective co growth on cu for void-free via fill* (2015). [DOI: 10.1109/IITC-MAM.2015.7325663]

3. R. C. Longo, S. McDonnell, D. Dick, R. M. Wallace, Y. J. Chabal, J. H. G. Owen, J. B. Ballard, J. N. Randall, and K. Cho, "Selectivity of metal oxide atomic layer deposition on hydrogen terminated and oxidized si(001)-(2×1) surface," *J Vac Sci Technol B* **32,** 03D112 (2014).

4. M. M. Kerrigan, J. P. Klesko, and C. H. Winter, "Low temperature, selective atomic layer deposition of cobalt metal films using bis(1,4-di-tert-butyl-1,3-diazadienyl)cobalt and alkylamine precursors," *Chemistry of Materials* **29,** 7458-66 (2017).

5. J. A. Singh, N. F. W. Thissen, W.-H. Kim, H. Johnson, W. M. M. Kessels, A. A. Bol, S. F. Bent, and A. J. M. Mackus, "Area-selective atomic layer deposition of metal oxides on noble metals through catalytic oxygen activation," *Chemistry of Materials* **30,** 663-70 (2018).

6. A. J. M. Mackus, M. J. Weber, N. F. W. Thissen, D. Garcia-Alonso, R. H. J. Vervuurt, S. Assali, A. A. Bol, M. A. Verheijen, and W. M. M. Kessels, "Atomic layer deposition of pd and pt nanoparticles for catalysis: On the mechanisms of nanoparticle formation," *Nanotechnology* **27,** 034001 (2015).

7. M. J. Weber, A. J. M. Mackus, M. A. Verheijen, C. van der Marel, and W. M. M. Kessels, "Supported core/shell bimetallic nanoparticles synthesis by atomic layer deposition," *Chemistry of Materials* **24,** 2973-7 (2012).

8. F. S. M. Hashemi and S. F. Bent, "Sequential regeneration of self-assembled monolayers for highly selective atomic layer deposition," *Advanced Materials Interfaces* **3,** 1600464 (2016).

9. F. S. M. Hashemi, C. Prasittichai, and S. F. Bent, "A new resist for area selective atomic and molecular layer deposition on metal–dielectric patterns," *The Journal of Physical Chemistry C* **118,** 10957-62 (2014).

10. R. Chen, H. Kim, P. C. McIntyre, and S. F. Bent, "Self-assembled monolayer resist for atomic layer deposition of hfo2 and zro2 high-κ gate dielectrics," *Applied Physics Letters* **84,** 4017-9 (2004).

11. L. Tzu-Ling and F. B. Stacey, "Area-selective atomic layer deposition of dielectric-on-dielectric for cu/low-k dielectric patterns," 2019, vol. 10960. [DOI: 10.1117/12.2519845]

12. D.-M. Tyler and J. G. Ekerdt, "Selective atomic layer deposition of cobalt for back end of line," *ECS Transactions* **80,** 29-37 (2017).

13. A. Mameli, M. J. M. Merkx, B. Karasulu, F. Roozeboom, W. M. M. Kessels, and A. J. M. Mackus, "Area-selective atomic layer deposition of sio2 using acetylacetone as a chemoselective inhibitor in an abc-type cycle," *Acs Nano* **11,** 9303-11 (2017).

14. X. Jiang and S. F. Bent, "Area-selective ald with soft lithographic methods: Using self-assembled monolayers to direct film deposition," *The Journal of Physical Chemistry C* **113,** 17613-25 (2009).

15. S. K. Song, H. Saare, and G. N. Parsons, "Integrated isothermal atomic layer deposition/atomic layer etching supercycles for area-selective deposition of tio2," *Chemistry of Materials* **31,** 4793-804 (2019).

16. F. S. Minaye Hashemi, C. Prasittichai, and S. F. Bent, "Self-correcting process for high quality patterning by atomic layer deposition," *ACS Nano* **9,** 8710-7 (2015).

17. H.-B.-R. Lee and S. F. Bent, "Microstructure-dependent nucleation in atomic layer deposition of pt on tio2," *Chemistry of Materials* **24,** 279-86 (2012).

18. E. Mohimi, Z. V. Zhang, S. M. Liu, J. L. Mallek, G. S. Girolami, and J. R. Abelson, "Area selective cvd of metallic films from molybdenum, iron, and ruthenium carbonyl precursors: Use of ammonia to inhibit nucleation on oxide surfaces," *Journal of Vacuum Science & Technology A* **36,** 041507 (2018).

19. S. Babar, N. Kumar, P. Zhang, and J. R. Abelson, "Growth inhibitor to homogenize nucleation and obtain smooth hfb_2 thin films by chemical vapor deposition," *Chemistry of Materials* **25,** 662-7 (2013).

20. A. E. Kaloyeros, Y. Pan, J. Goff, and B. Arkles, "Editors' choice—review—cobalt thin films: Trends in processing technologies and emerging applications," *ECS Journal of Solid State Science and Technology* **8,** P119-P52 (2019).

21. Z. V. Zhang, S. Liu, G. S. Girolami, and J. R. Abelson, "Area-selective chemical vapor deposition of cobalt from dicobalt octacarbonyl: Enhancement of dielectric-dielectric selectivity by adding a coflow of nh3," *Journal of Vacuum Science & Technology A* **38,** 033401 (2020).

22. G. Ruhl, B. Froschle, P. Ramm, A. Intemann, and W. Pamler, "Deposition of titanium nitride/tungsten layers for application in vertically integrated-circuits technology," *Applied Surface Science* **91,** 382-7 (1995).

23. Y. Hwang, B. M. Nguyen, and S. A. Dayeh, "Atomic layer deposition of platinum with enhanced nucleation and coalescence by trimethylaluminum pre-pulsing," *Applied Physics Letters* **103,** 263115 (2013).

24. B. N. Zope and A. V. Gelatos, "Surface treatment to improve cctba based cvd co nucleation on dielectric substrate," United States US 9,218,980 B2

25. H. Han, J. J. Kim, and D. Y. Yoon, "Pretreatment technique for surface improvement of ru films in ru-metalorganic chemical vapor deposition," *Journal of Vacuum Science & Technology A: Vacuum, Surfaces, and Films* **22,** 1120-3 (2004).

26. N. Kumar, A. Yanguas-Gil, S. R. Daly, G. S. Girolami, and J. R. Abelson, "Remote plasma treatment of si surfaces: Enhanced nucleation in low-temperature chemical vapor deposition," *Applied Physics Letters* **95,** 144107 (2009).

27. K. S. Choi, J. M. Lim, S. Roy, and C. M. Lee, "Enhancement of ru nucleation in ru-metal organic chemical vapor deposition by electron cyclotron resonance plasma pretreatment," *Jpn J Appl Phys 1* **42,** 5539-42 (2003).

28. J. Lim, H. Park, and C. Lee, "Enhancement of ru nucleation by pretreatments of the underlying tasin film surface in ru mocvd," *Thin Solid Films* **475,** 194-7 (2005).

29. S. Babar, L. M. Davis, P. Y. Zhang, E. Mohimi, G. S. Girolami, and J. R. Abelson, "Chemical vapor deposition of copper: Use of a molecular inhibitor to afford uniform nanoislands or smooth films," *Ecs Journal of Solid State Science and Technology* **3,** Q79-Q83 (2014).

30. J. J. Kim, M. S. Kim, and D. Y. Yoon, "Effects of an added iodine source (c2h5i) on ru metal–organic chemical vapor deposition," *Chemical Vapor Deposition* **9,** 105-9 (2003).

31. J. J. Kim, D. H. Jung, M. S. Kim, S. H. Kim, and D. Y. Yoon, "Surface roughness reducing effect of iodine sources (ch3i, c2h5i) on ru and ruo2 composite films grown by mocvd," *Thin Solid Films* **409,** 28-32 (2002).

32. K. M. Thom and J. G. Ekerdt, "The effect of an iodine source on nucleation and film properties of ru films deposited by chemical vapor deposition," *Thin Solid Films* **518,** 36-42 (2009).

33. W. Liao and J. G. Ekerdt, "Effect of co on ru nucleation and ultra-smooth thin film growth by chemical vapor deposition at low temperature," *Chemistry of Materials* **25,** 1793-9 (2013).

34. S. Hassani, K. Raeissi, and M. A. Golozar, "Effects of saccharin on the electrodeposition of ni–co nanocrystalline coatings," *Journal of Applied Electrochemistry* **38,** 689-94 (2008).

35. M. Bhardwaj, K. Balani, R. Balasubramaniam, S. Pandey, and A. Agarwal, "Effect of current density and grain refining agents on pulsed electrodeposition of nanocrystalline nickel," *Surface Engineering* **27,** 642-8 (2011).

36. F. A. Crossley and L. F. Mondolfo, "Mechanism of grain refinement in aluminum alloys," *Jom* **3,** 1143-8 (2017).

37. S.-W. Kang, Y.-J. Park, Y.-S. Kim, Y.-H. Shin, and J.-Y. Yun, "Real-time evaluation of aluminum borohydride trimethylamine for aluminum chemical vapor deposition," *Journal of The Electrochemical Society* **156,** H333-H9 (2009).

38. V. Hopfe, D. W. Sheel, C. I. M. A. Spee, R. Tell, P. Martin, A. Beil, M. Pemble, R. Weiss, U. Vogt, and W. Graehlert, "In-situ monitoring for cvd processes," *Thin Solid Films* **442,** 60-5 (2003).

39. M. Katiyar and J. R. Abelson, "Methods to enhance absorption signals in infrared reflectance spectroscopy: A comparison using optical simulations," *Journal of Vacuum Science & Technology A* **13,** 2005-12 (1995).

40. N. Maley, I. Szafranek, L. Mandrell, M. Katiyar, J. R. Abelson, and J. A. Thornton, "Infrared relfectance spectroscopy of very thin films of a-sih," *Journal of Non-Crystalline Solids* **114,** 163-5 (1989).

41. M. Katiyar, G. F. Feng, Y. H. Yang, J. R. Abelson, and N. Maley, "Hydrogen incorporation in the early stages of hydrogenated amorphous silicon deposition evaluated by real time infrared reflectance spectroscopy," *Applied Physics Letters* **63,** 461-3 (1993).

42. M. Katiyar, Y. H. Yang, and J. R. Abelson, "Hydrogen-surface reactions during the growth of hydrogenated amorphous silicon by reactive magnetron sputtering: A real time kinetic study by in situ infrared absorption," *Journal of Applied Physics* **77,** 6247-56 (1995).

43. R. G. Greenler, "Infrared study of adsorbed molecules on metal surfaces by reflection techniques," *Journal of Chemical Physics* **44,** 310-& (1966).

44. T. Buffeteau, B. Desbat, and J. Turlet, "Polarization modulation ft-ir spectroscopy of surfaces and ultra-thin films: Experimental procedure and quantitative analysis," *Applied Spectroscopy* **45,** 380-9 (1991).

45. D. Blaudez, T. Buffeteau, J. C. Cornut, B. Desbat, N. Escafre, M. Pezolet, and J. M. Turlet, "Polarization modulation ftir spectroscopy at the air-water interface," *Thin Solid Films* **242,** 146-50 (1994).

46. D. Blaudez, T. Buffeteau, B. Desbat, M. Orrit, and J. M. Turlet, "Characterization of langmuir-blodgett monolayers using polarization modulated ftir spectroscopy," *Thin Solid Films* **210-211,** 648-51 (1992).

47. K. Kunimatsu, H. Seki, W. G. Golden, J. G. Gordon, and M. R. Philpott, "Electrode/electrolyte interphase study using polarization modulated ftir reflection-absorption spectroscopy," *Surf Sci* **158,** 596-608 (1985).

48. M. H. van der Veen, K. Vandersmissen, D. Dictus, S. Demuynck, R. Liu, X. Bin, P. Nalla, A. Lesniewska, L. Hall, K. Croes, L. Zhao, J. Bommels, A. Kolics, Z. Tokei, and Ieee, "Cobalt bottom-up contact and via prefill enabling advanced logic and dram technologies," *2015 IEEE International Interconnect Technology Conference and 2015 IEEE Materials for Advanced Metallization Conference***,** 25-7 (2015).

49. M. Nandakumar, A. Chatterjee, S. Sridhar, K. Joyner, M. Rodder, and I. Chen, "Shallow trench isolation for advanced ulsi cmos technologies," 1998, p. 133-6. [DOI: 10.1109/IEDM.1998.746297]

50. W. B. Wang, N. N. Chang, T. A. Codding, G. S. Girolami, and J. R. Abelson, "Superconformal chemical vapor deposition of thin films in deep features," *Journal of Vacuum Science & Technology A* **32,** 051512 (2014).

51. Y. Au, Y. Lin, and R. G. Gordon, "Filling narrow trenches by iodine-catalyzed cvd of copper and manganese on manganese nitride barrier/adhesion layers," *Journal of The Electrochemical Society* **158,** D248-D53 (2011).

52. T. K. Talukdar, W. B. Wang, G. S. Girolami, and J. R. Abelson, "Superconformal coating and filling of deep trenches by chemical vapor deposition with forward-directed fluxes," *Journal of Vacuum Science & Technology A* **36,** 051513 (2018).

53. W. B. Wang and J. R. Abelson, "Filling high aspect ratio trenches by superconformal chemical vapor deposition: Predictive modeling and experiment," Journal of Applied Physics 116, 194508 (2014).

CHAPTER 2

AREA-SELECTIVE CHEMICAL VAPOR DEPOSITION OF COBALT FROM DICOBALT OCTACARBONYL: ENHANCEMENT OF DIELECTRIC-DIELECTRIC SELECTIVITY BY ADDING A COFLOW OF AMMONIA

2.1 Introduction

Many nanoscale electronic devices are fabricated by a top-down approach involving blanket thin film deposition followed by photolithographic patterning and etching steps. However, as feature sizes shrink towards or below 10 nm, edge placement errors in photolithography make it difficult to avoid unacceptable misalignments between layers. For this reason, bottom-up patterning methods that automatically result in pattern registry are becoming increasingly attractive. One such bottom-up method is area-selective deposition (ASD), in which, for example, growth occurs on metallic surfaces but not on dielectric surfaces [1]. As a result, ASD reduces production costs by obviating the need for additional patterning and etching steps. Another potential application of ASD is in dual damascene metallization, which requires void-free fill of vias with high aspect ratio. ASD can meet this need by bottom-up growth, which occurs when film nucleates on the bottom of the feature but not on the sidewalls [2]. Most area-selective deposition processes developed so far concern selective deposition of metal on metal or oxide on oxide; only a few studies have dealt with selective deposition of other materials combinations[3], such as metal on oxide, or metal on one oxide but not on another.

No deposition process is area-selective indefinitely: even on the most unreceptive surfaces, nucleation and growth will eventually occur. Therefore, given a pair of surfaces, a deposition can be considered as “more selective” if there is a larger difference in the nucleation delay. But if steady state growth after nucleation is slow, then relatively little film can be grown selectively even if the nucleation delay times differ significantly. As a result, a better metric for selectivity for a particular deposition process is not the difference in nucleation delay, but how thick a film can be grown on one surface vs. another.

Accordingly, a useful metric for selectivity is the parameter *S*, defined as [4]:

$$S = \frac{n_{GS} - n_{NG}}{n_{GS} + n_{NG}}$$

where n_{GS} and n_{NG} are the number of atoms deposited per unit area on the growth surface and the non-growth surface, respectively. The *n* values are equivalent to film thickness under the assumption of constant atomic density. If $S = 1$, then the deposition is perfectly selective and there is no deposition on the non-growth substrate; if $S = 0$ then the deposition is non-selective. It is sometimes possible to increase *S* by employing a cyclic deposition process in which a light etching step on each cycle is used to remove stray nuclei or metal atoms from the non-growth surface [5].

There is significant and growing interest in cobalt, especially in the context of applications in interconnects (ICs) at the < 10 nm node. The reason for this interest is that cobalt has a low bulk resistivity (~ 6 μΩ·cm), adheres strongly to Cu [6], and has a low solubility in Cu [7]. A Co capping layer significantly improves the lifetime of the copper lines in modern ICs by reducing Cu electromigration [8-10] without unduly increasing the RC delay [11]. Also, Co requires less or no diffusion barrier when used alone as an interconnect material [12], thus avoiding the increased interconnect resistivity associated with scaling down the sizes of vias in ICs [13].

Area selective deposition of cobalt films has been carried out by electrodeposition [14] and electroless deposition [15] methods, and also by ALD [16] and CVD [17,18]. Most of these studies involve selective Co deposition on metal vs. a neighboring oxide.

In the present work, we investigate the ASD of cobalt on different oxides from dicobalt octacarbonyl, $Co_2(CO)_8$, and investigate the effect of ammonia on the selectivity. The choice of ammonia as a selectivity enhancer was made because we have recently shown that this molecule enhances metal vs. oxide ASD from $Mo(CO)_6$ [19]. As we will show, $Co_2(CO)_8$ behaves quite differently from $Mo(CO)_6$. For example, nucleation from $Co_2(CO)_8$ in the absence of ammonia is somewhat faster on basic oxides such as Al_2O_3 than on acidic oxides such as SiO_2, whereas in the other systems the exact opposite behavior is seen. In addition, for $Co_2(CO)_8$ a coflow of ammonia has negligible effect on the nucleation rate for deposition on Al_2O_3 but it strongly

inhibits nucleation and growth on SiO_2, whereas for the other metal carbonyls ammonia slows growth on all oxide surfaces.

The net result is that ammonia enables highly selective ASD of Co from $Co_2(CO)_8$ on some oxide surfaces over others. In addition, the cobalt deposition process can in some cases be tuned to enable nucleation of Co on metal but not on oxide, or Co on oxide but not on metal, by taking advantage of native oxides or ozone-generated oxide overlayers.

2.2 Experimental

The CVD experiments are performed in a cold wall high vacuum chamber described elsewhere [20,21]. The precursor $Co_2(CO)_8$ is purchased from Sigma Aldrich and used as received. This precursor is supplied by the vendor as a mixture with 1-10 % hexane to improve shelf life; the hexane is removed by evacuation before the first use of the precursor. The precursor is maintained in a glass container immersed in a water bath at 20 °C and delivered to the chamber without a carrier gas through a 0.4 cm i.d. stainless steel tube aimed at the substrate. These conditions supply a precursor partial pressure of 0.018 mTorr as measured in the chamber background, but the local fluxes delivered to the substrate by the effusive flow from the dosing tube are higher than those suggested by the isotropic background pressure. At the higher flow rates, the local fluxes are also affected by gas scattering when the mean free path becomes smaller than the distance from the injection tube to the substrate. To maintain a nearly constant effect of gas scattering on the effusing flux of precursor, Ar is added to maintain a total chamber pressure of 4 mTorr. Research grade ammonia (99.992%) and Ar (99.999%) are delivered into the chamber via separate mass flow controllers and delivery lines. Substrates are radiatively heated to 70 °C, as measured by a K-type thermocouple attached to the sample holder.

All substrates are degreased by washing successively with acetone, IPA, and deionized water, and are then cleaned by UV ozone treatment for 10 min before being loaded into the chamber, unless noted otherwise. In control experiments (*Supplementary materials*), we determined that UV ozone treatment can remove organic contamination due to exposure to atmosphere, which otherwise may increase the nucleation delay. The UV ozone treatment also

restores hydrophilicity (Supplementary Fig. 2.2), which is not the case when using acetone, IPA, and deionized water cleaning alone [22,23].

The following substrates have been studied: (a) 300 nm thermal SiO_2 (microelectronic grade) on Si. (b) 10 nm ALD Al_2O_3 on Si deposited from trimethylaluminum and water; a patterned Al_2O_3 / SiO_2 substrate is also fabricated by ALD of Al_2O_3 on SiO_2 that had been masked using a standard photolithography process, followed by lift-off. (c) 10 nm ALD HfO_2 on Si deposited from tetrakis(dimethylamido)hafnium and water. (d) 300 nm CVD MgO on Si deposited from magnesium *N*,*N*-dimethylaminodiboranate and water [24]. (e) 10 nm ALD TiO_2 on Si deposited from tetrakis(dimethylamido)titanium and water. (f) 50 nm thermal WO_3 on Si fabricated by annealing an e-beam evaporated tungsten film at 400 °C in O_2 for 3h [25]. (g) Dehydroxylated SiO_2, which is obtained by annealing sample (a) at 900 °C for 2 h and cooling to room temperature in dry oxygen; the resulting substrate is immediately loaded into the CVD chamber [26,27], without further cleaning. Unlike some metal oxides, the rehydroxylation process on dehydroxylated SiO_2 is very slow in air at room temperature (typically weeks to months) [27-30], so the SiO_2 surface does not rehydroxylate significantly during the few minutes required to transfer the sample from the annealing furnace to the CVD chamber. For resistivity and growth rate measurements, the SiO_2 substrates are pre-dosed in-situ with tetrakis(dimethylamino)vanadium (TDMAV) (Sigma Aldrich) for 2 min to create a nucleation layer that minimizes the nucleation delay. The self-limiting TDMAV layer is thin (~ 1 monolayer) and the contribution to electric conductivity is negligible.

Real-time spectroscopic ellipsometry (SE) is used during growth to monitor the onset of nucleation. We report change in the ellipsometric angle Ψ at a single energy, 2.65 eV, which provides the greatest sensitivity to the onset of nucleation, as discussed previously [31]. $Co_2(CO)_8$ molecules start to flow at time = 0. The start of the nucleation is defined by the time at which Ψ starts to change. Note that Ψ is the amplitude component of the complex reflectance ratio between the p and s components, which includes all the interference effects between layers. Hence, for different substrates the slope of the curve does not correspond in an intuitive way to the growth rate, i.e., the curve can have a descending or ascending slope, and may change the trend as the deposition proceeds. The area density of metal atoms is measured by XRF (Shimadzu EDX7000); we report an equivalent film thickness under the assumption that the

deposited cobalt has bulk density. Measurement by XRF is quite accurate with 10% random error for a film of 1.5 nm. The average growth rate is determined by dividing film thickness with growth time after subtracting the nucleation delay time indicated by SE. Elemental mapping is carried out by XPS (Kratos AXIS XPS). Depth profiling of composition is also performed by XPS (PHI 5400). Film roughness is measured by AFM (Asylum cypher). Resistivity is measured by the 4-point probe method (thicknesses of films for resistivity are measured by SEM).

2.3 Results and Discussion

The following sections will describe our studies of the area-selective deposition of cobalt from the precursor dicobalt octacarbonyl. As we previously discussed [19], the phenomenon of area-selective deposition is sensitive to the history of the surfaces being studied. The use of UV-ozone cleaning appears to eliminate the effect of contamination due to atmosphere. Other experimental factors, such as the duration of exposure to air during sample transfer, the temperature to which a surface is heated, and how long it is kept at that temperature before deposition, are kept constant. Below, we report that the state of hydroxylation of the oxide surface is an important variable in ASD. The results below pertain to growth of cobalt on surfaces prepared as described in the experiment section; substrates pretreated in other ways may show different behavior.

2.3.1 Area-selective growth of cobalt on oxides in the absence of ammonia

We find that deposition of cobalt from $Co_2(CO)_8$ at 0.018 mTorr and 70 °C on Al_2O_3 exhibits a short (< 1 min) nucleation delay as observed by spectroscopic ellipsometry (SE), followed by an increasing growth rate for 5~9 min, which is attributed to the progressive increase in surface coverage up to coalescence (Fig. 2.1). For longer times, the growth rate is stable at ~ 1.5 nm/min. In these experiments (and those conducted in the presence of ammonia to be described later), we keep the gas scattering rate approximately constant by adding a co-flow of Ar such that the total chamber pressure is always 4 mTorr. In the absence of Ar, the growth rates with 0.018 mTorr of precursor flow alone are a little higher (1.7 ~ 1.8 nm/min), indicating that gas scattering effects have only a slight effect on the growth rate.

By contrast, on SiO_2, no change is observed by SE during the first ~ 4 min, but after this time, deposition commences. Thus, at 70 °C deposition of cobalt from $Co_2(CO)_8$ is inherently selective on SiO_2 vs. Al_2O_3, although the selectivity is lost after only ~ 4 min.

AFM data shows that the film roughness is ~ 0.8 nm on Al_2O_3 and ~ 2.2 nm on SiO_2 for the same film thickness of ~ 1.5 nm (Fig. 2.2). This result is consistent with the nucleation results obtained by SE: the rate of nucleation relative to the rate of steady state growth is higher on Al_2O_3 than on SiO_2, so that, at coalescence, there is a higher density of smaller islands on Al_2O_3 and the resulting coalesced film is less rough [32]. When the precursor pressure is 0.018 mTorr, the steady state growth rate of cobalt is ~ 1.5 nm/min (Fig. 2.3). The electrical resistivity of 11 ~ 20 μΩ·cm for films of 40 nm thick matches the results from other groups [33,34]. XPS depth profiling shows that the carbon and oxygen content of the cobalt films is below the detection limit (Fig. 2.4).

2.3.2 Effect of ammonia on steady state growth of cobalt

We now describe the effect of adding a co-flow of ammonia on the growth of cobalt from $Co_2(CO)_8$ at 0.018 mTorr and 70 °C. Before we consider the effect on nucleation delays, we first describe the effect on the steady-state growth rate and other properties. The steady-state growth rate of 1.5 nm/min seen in the absence of NH_3 slows to 0.8 ~ 1.1 nm/min at a co-flow of 0.1 mTorr of NH_3, and becomes constant at 0.4 ~ 0.5 nm/min for a NH_3 co-flow of ~ 0.5 mTorr and above (Fig. 2.3). Thus, NH_3 acts as a growth inhibitor; in several other CVD systems, we have seen similar behavior in which the growth rate is significantly slowed but not reduced to zero at high inhibitor pressures [35].

Films grown in the presence of ammonia have a resistivity of 15 ~ 25 μΩ·cm that is marginally higher than the 11 ~ 20 μΩ·cm values seen in the absence of ammonia. Films grown at both conditions are XRD amorphous (Fig. 2.4). The films contain no detectable carbon and nitrogen, but there is ~ 5 at. % oxygen (Fig. 2.5), which may account for the slightly higher resistivity seen for samples grown in the presence of NH_3. The oxygen may come from the background of the chamber (10^{-7} Torr) during the longer growth time (slower growth rate) or from post-growth air exposure. The absence of detectable carbon rules out the possibility that the oxygen arises by cracking of CO.

2.3.3 Area-selective growth of cobalt on oxides in the presence of ammonia

When cobalt is deposited from 0.018 mTorr $Co_2(CO)_8$ at 70 °C in the presence of 4 mTorr of NH_3, the nucleation delay on Al_2O_3 is lengthened from < 1 min to ~ 7 min, and the nucleation delay on SiO_2 is lengthened from ~ 4 min to 35 min (Fig. 2.6a). Higher pressure of ammonia (~8 mTorr) does not lengthen the delay further. This inhibition effect greatly expands the process window for selective growth on a patterned Al_2O_3 / SiO_2 substrate. When such a patterned substrate is exposed at 70 °C for 30 min to a $Co_2(CO)_8$ pressure of 0.018 mTorr and an ammonia pressure of 4 mTorr, XPS elemental mapping shows that significant cobalt deposition occurs on the Al_2O_3 surface but essentially none on SiO_2; a clear boundary separates the two regions (Fig. 2.6b). An XPS survey scan on the SiO_2 side reveals that only a trace of cobalt (equivalent to a film 0.05 nm thick, according to a detailed fit [36]) can be detected on the surface (Fig. 2.6c). The Co film deposited on Al_2O_3 has a thickness of ~ 9.5 nm as judged by AFM (Fig.2.7).

The ability of ammonia to enhance the selectivity for nucleation and growth of Co on Al_2O_3 over SiO_2 is also seen for surfaces prepared in alternative ways: in the presence of NH_3, nucleation is strongly inhibited on SiO_2 deposited by magnetron sputtering (SiO_2 target), but nucleation occurs readily on Al_2O_3 formed by thermal oxidation of Al (Fig. 2.8).

To further investigate selective nucleation on Al_2O_3 vs. SiO_2, we deposited cobalt films from 0.018 mTorr of precursor and 4 mTorr of ammonia for periods of 10 to 40 min; the thickness is measured by XRF (Fig. 2.9a). On Al_2O_3, growth has already started after 10 minutes, and the steady state growth rate is ~ 0.5 nm/min; after 40 min, 15 nm of cobalt is deposited. In contrast, on SiO_2, growth begins only after 40 min.

Taken together, these results show that, for 14 nm of Co grown on Al_2O_3 under the conditions above, the selectivity *S* (defined in the introduction) of Al_2O_3 over SiO_2 is 0.97 in the presence of NH_3 but < 0.5 in the absence of NH_3 (Fig. 2.9b), i.e., selectivity is improved significantly by co-flowing with NH_3.

2.3.4 Nucleation delay as a function of the oxide surface

In order to extend the observations above, we investigated the effect of a NH_3 co-flow on deposition of Co films from $Co_2(CO)_8$ on a variety of oxide surfaces (Fig. 2.10). For growth at 70 °C from 0.018 mTorr of $Co_2(CO)_8$ in the presence of 4 mTorr of NH_3, the nucleation delays decrease in the following order (as determined by ellipsometry): WO_3 (>30 min), SiO_2 (>30 min), TiO_2 (15 min), HfO_2 (10 min), Al_2O_3 (10 min), and MgO (10 min). Notably, for these oxide surfaces, there is an excellent correlation between the nucleation delay and the acidity of the surface: as judged by their isoelectric points (IEP values given in parentheses), the oxide surfaces we investigated decrease in acidity in the order: WO_3 (IEP = 1.5~2), SiO_2 (2.2), TiO_2 (4~6), HfO_2 (7.5), Al_2O_3 (8~9), and MgO (12) [37]. XRF studies confirm that no deposition of Co occurs before the times indicated by ellipsometry (FIG. 2.10). For comparison, nucleation occurs with short delays (1~2 min) on WO_3 when deposition is conducted in the absence of NH_3 (Fig. 2.11).

2.3.5 Mechanistic role of hydroxyl groups in the enhancement of cobalt deposition selectivity by ammonia

To explore the role of hydroxyl groups in the nucleation process, SiO_2 surfaces were treated in ways that are known to subtract or add hydroxyl sites. As described above, our reference surface, a 300 nm thermal SiO_2/Si substrate that is pre-washed and cleaned by UV ozone treatment, shows a nucleation delay of ~ 4 min in the absence of ammonia and ~ 35 min in its presence.

First, a fully dehydroxylated SiO_2 surface was prepared by heating a previously prepared SiO_2/Si sample to 900 °C in dry oxygen. On this surface, Co nucleation is rapid [38]: in the absence of NH_3 it occurs after ~ 2 min (and the film is 3.9 nm thick after 5 min); in the presence of NH_3 nucleation is delayed and begins after ~ 10 min (and the film is 6 nm thick after 30 min) (Fig. 2.12). Second, a dehydroxylated surface was rehydroxylated by dipping it in a piranha solution at 80 °C for 10 min. This process is reported to afford a higher density of hydroxyl groups compared to the original SiO_2 surface (before dehydroxylation)[29]. On the rehydroxylated surface, nucleation is suppressed by NH_3 to an even greater degree than on the

original surface, and no cobalt is deposited even after 60 min (Fig. 8). An AFM image (Fig. 8, inset) shows no difference between this exposed surface and a fresh substrate.

These results indicate that (1) the chemically reactive strained siloxane rings, which are present on highly dehydroxylated SiO_2 surfaces [39], are good nucleation sites for $Co_2(CO)_8$; (2) nucleation at such strained siloxane rings is not strongly inhibited by added NH_3; and (3) hydroxyl groups on SiO_2 are the target of the inhibition of cobalt deposition from $Co_2(CO)_8$.

2.3.6 Selectivity between oxides and metals

In the absence of NH_3, the nucleation delay for deposition of Co on gold (Fig. 2.14) and vanadium nitride (deposition by CVD [40]) is negligible, so that there is little intrinsic selectivity between gold and SiO_2 (which also has a short nucleation delay in the absence of NH_3, as shown above). Interestingly, whereas NH_3 can significantly inhibit nucleation on SiO_2, it has a negligible effect on gold and vanadium nitride, and nucleation still takes place readily (Fig. 13a). Therefore, we conclude that area-selective deposition of cobalt on gold or vanadium nitride, and not on SiO_2, should be possible by carrying the deposition in the presence of NH_3.

Selective deposition of Co on oxide but not on metal can also be achieved using NH_3 as an inhibitor when the oxide (intended growth surface) is basic and the metal (intended non-growth surface) can form an acidic oxide overlayer. Nucleation on tungsten with UV/ozone-grown oxide (Fig. 13b) behaves similarly to that on thermal WO_3 and can be significantly retarded by using ammonia. When cobalt is desired on Al_2O_3 but not on tungsten, the whole substrate can be treated with ozone to oxidize W and form a thin WO_3 layer, followed by selective deposition from $Co_2(CO)_8$ in the presence of NH_3 (As noted above, all Al_2O_3 surfaces used in this work are cleaned by UV/ozone, hence, the treatment required to oxidize the W will have no further effect on the Al_2O_3 surface.). After cobalt deposition on the Al_2O_3, the tungsten oxide could then be reduced, for example by a H_2 plasma [41], or etched to restore a metallic surface.

2.3.7 Mechanistic interpretation

We previously demonstrated ASD of metallic films on metal substrates in preference to oxide substrates from the carbonyl precursors $Mo(CO)_6$, and showed that the selectivity was greatly enhanced by adding a co-flow of ammonia during CVD [19]. We now find that there are some interesting differences between the behavior of $Co_2(CO)_8$ and $Mo(CO)_6$:

- For $Mo(CO)_6$ in the absence of ammonia, the nucleation delay is *longer* on the basic oxides Al_2O_3 and MgO, and is *shorter* on the acidic oxides SiO_2, TiO_2, and RuO_2. In contrast, for $Co_2(CO)_8$, in the absence of ammonia, the nucleation delay is *shorter* on basic oxides such as Al_2O_3 and *longer* on acidic oxides such as SiO_2.
- For $Mo(CO)_6$, the addition of ammonia results in long nucleation delays on all oxide surfaces; the net effect is to decrease selectivity for growth on one oxide over another (although the selectivity for growth on metal over oxide is greatly improved). For $Co_2(CO)_8$, a coflow of ammonia has a negligible effect on the nucleation rate on basic oxides such as Al_2O_3 (the nucleation delay remains short), but it greatly lengthens the nucleation delay on acidic oxides such as SiO_2; the net result is that the selectivity for growth on one oxide over another is greatly enhanced.

In our earlier work, we proposed that the effect of ammonia in ASD from $Mo(CO)_6$ can be understood as follows [19]. On basic oxides such as Al_2O_3, the intermediate $Mo(CO)_3$ [42] is stable up to 400 °C [43,44], and as a result the decarbonylation of $Mo(CO)_6$ stops at this stage and the nucleation delay is long. Addition of NH_3 has little effect on this result. On acidic oxides such as SiO_2, however, the intermediate $Mo(CO)_3$ is intrinsically unstable and the nucleation delay is therefore short. Addition of NH_3 lengthens the nucleation delay in one of two ways: it either acts as a site blocker that prevents adsorption of the $Mo(CO)_6$ precursor, or it increases the basicity of the surface, which then stabilizes the $Mo(CO)_3$ subcarbonyl intermediate. In either case, nucleation is delayed.

Here we discuss possible reasons for the different behavior of cobalt, which is grounded in experimental and theoretical studies of the chemistry of $Co_2(CO)_8$ on various oxide surfaces [38,45-54]. Basic oxide surfaces such as Al_2O_3 promote the disproportionation of $Co_2(CO)_8$ to Co^{2+} and $Co(CO)_4^-$, in which the Co^{2+} species are bound to the basic sites [38,53,54]. This surface reaction is analogous to the well-known disproportionation that takes place when Lewis

bases are added to $Co_2(CO)_8$ in solution [55]. We hypothesize that the surface-bound Co^{2+} species serve as nucleation sites for growth of Co; this hypothesis accounts for why the nucleation delay is short on basic oxides. In contrast, on acidic oxide surfaces such as SiO_2, the low basicity of the surface means that the disproportionation of $Co_2(CO)_8$ to Co^{2+} and $Co(CO)_4^-$ is unfavorable, which leads to a long nucleation delay [53].

The above mechanism explains why, in the absence of ammonia, $Co_2(CO)_8$ nucleates with a shorter delay on basic oxides but a longer delay on acidic oxides. We now turn to the question of why ammonia further lengthens the nucleation delay on acidic oxides (but has little effect on basic oxides). The adsorption of NH_3 should make acidic oxides more basic and thus induce the disproportionation of $Co_2(CO)_8$; in the absence of other factors the net result should be to shorten the nucleation delay, instead of the lengthening actually observed.

One possible way to explain the observed behavior is that, on acidic oxides, NH_3 acts as a site blocker, which prevents adsorption of the $Co_2(CO)_8$ precursor. Another possibility is that NH_3 converts the active adsorbed cobalt species ($Co_2(CO)_8$ and Co^{2+}) to an inert form[38] such as $Co(NH_3)_x^{2+}$; the reaction of Co^{2+} with ammonia to form $Co(NH_3)_x^{2+}$ species is known to occur on oxide surfaces at room temperature in the presence of >2 Torr pressures of NH_3 [38,56].

But if NH_3 renders the Co^{2+} species inert on acidic oxides, why is this same effect not seen on basic oxides? It is known that SiO_2 and other acidic oxides have surface sites with a very high binding affinity for ammonia, so that ammonia remains on the surface even at temperatures much higher than 70 °C; in contrast, basic oxides such as Al_2O_3 do not bind ammonia strongly at these temperatures[57]. Therefore, when a Co^{2+} ion is formed on an acidic oxide (which has a high concentration of adsorbed NH_3), it is rapidly trapped and deactivated by reaction with surface-bound NH_3, whereas when a Co^{2+} ion is formed on a basic oxide (which has a low concentration of adsorbed NH_3), it is not rapidly trapped, and instead can serve as a nucleation site for growth of Co.

Thus, the difference in nucleation behavior between $Mo(CO)_6$ and $Co_2(CO)_8$ on acidic vs. basic oxide surfaces (and the effect of added ammonia) is attributed to the different nature of the reaction intermediates that are formed, and their relative kinetic stabilities.

2.4 Conclusion

Area-selective CVD of cobalt from $Co_2(CO)_8$ on one oxide surface but not on another is demonstrated: a co-flow of ammonia can inhibit nucleation on acidic oxides, such as SiO_2 and WO_3, whereas it has negligible effect on more basic oxides, such as Al_2O_3, HfO_2, and MgO. Thus, 15 nm of Co can be grown on Al_2O_3 in 40 min whereas the Co thickness on SiO_2 is less than 0.1 nm. The effect of NH_3 on nucleation delay is seen not only for bulk oxide surfaces, but also for metal surfaces on which a thin oxide has been grown.

Acidic hydroxyl groups on the oxide surface appear to play an important role in inhibition, because ammonia will not inhibit nucleation on dehydroxylated SiO_2. In contrast, on rehydroxylated SiO_2 surfaces, nucleation in the presence of ammonia is completely suppressed in experiments lasting one hour.

The mechanism of nucleation appears to be disproportionation of $Co_2(CO)_8$ to Co^{2+} (which promotes nucleation) and $Co(CO)_4^-$. This disproportionation occurs readily on basic oxides but is unfavorable on acidic oxides such as SiO_2. Addition of NH_3 has little effect on basic oxides (probably because such surfaces do not bind NH_3 well), whereas NH_3 further retards the formation of nucleation centers on SiO_2 (probably because such surfaces bind NH_3, which acts either as a site blocker or converts Co^{2+} to inactive $Co(NH_3)_x^{2+}$ species).

The results of this study open up new possibilities for selective growth on one metal over another, on oxide over metal, and on metal over oxide, in some cases by taking advantage of the different effect of ammonia on the nucleation delay seen for the native metal surface vs. the same metal surface covered with a thin oxide overlayer.

2.5 Figures

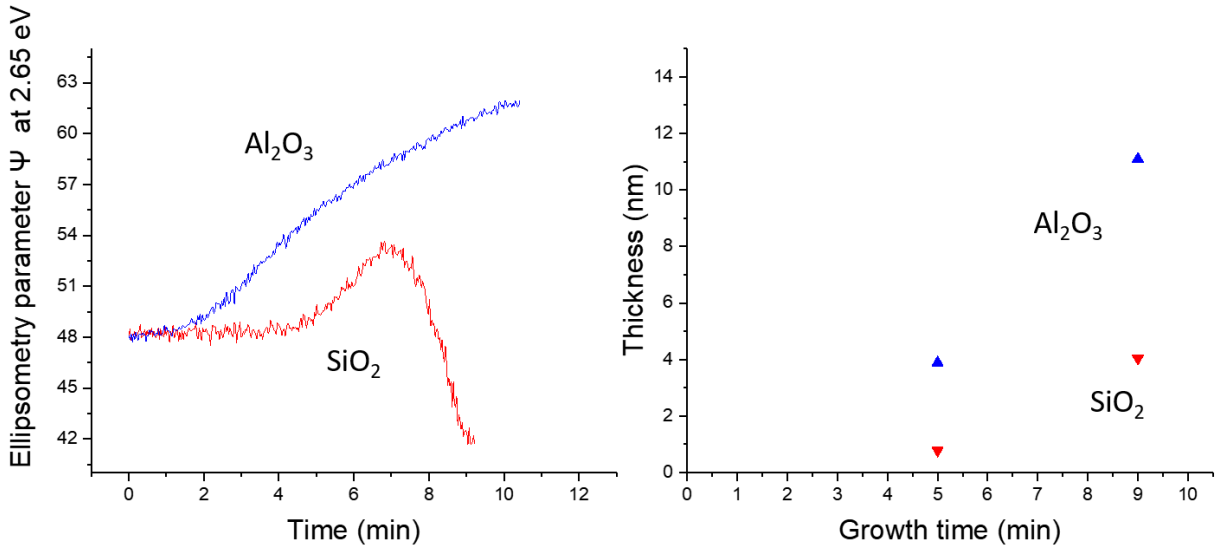

Figure 2.1. a) In situ ellipsometry parameter Ψ, at a photon energy of 2.65 eV, vs. time for Co film growth from $Co_2(CO)_8$ at 70 °C on Al_2O_3 and SiO_2 in the absence of NH_3 (curves are shifted vertically to display in the same range of Ψ). b) Curve of cobalt film thickness vs. growth time (including nucleation delay). Thicknesses are measured by XRF.

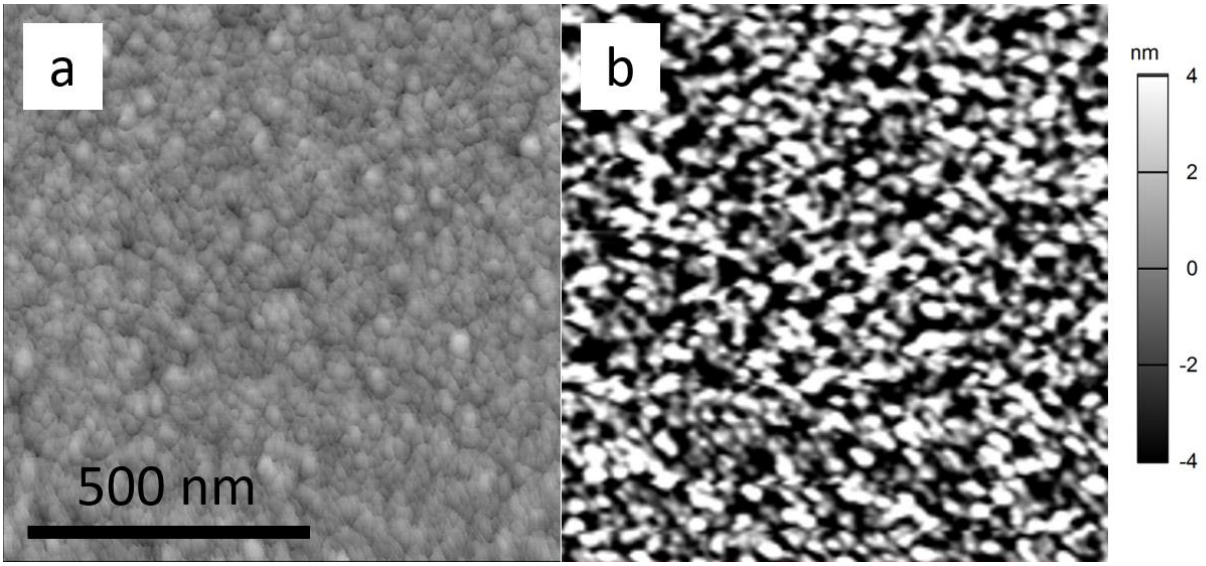

Figure 2.2. AFM scans of 1.5 nm thick cobalt films grown from $Co_2(CO)_8$ at 70 °C on a) Al_2O_3 and b) SiO_2.

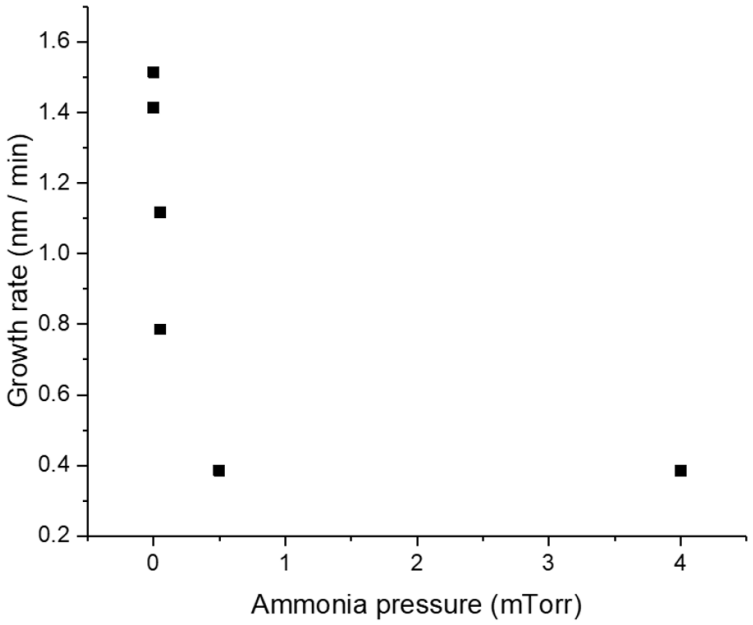

Figure 2.3. Effect of NH_3 pressure on steady-state cobalt growth rate from $Co_2(CO)_8$ at 70 °C. Thicknesses are measured by XRF.

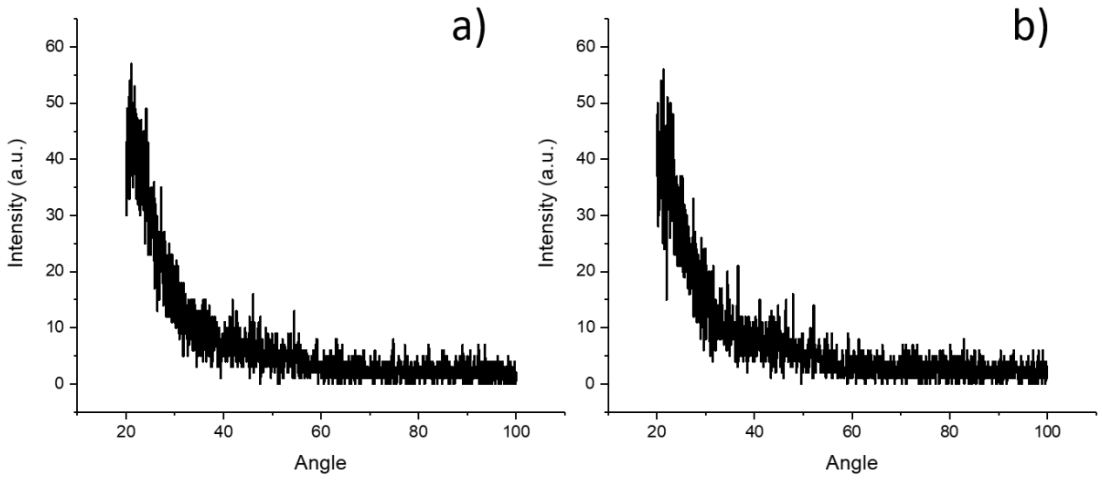

Figure 2.4. XRD patterns of cobalt films grown in the absence (a) and presence (b) of ammonia. The thicknesses are 52 nm and 41 nm, respectively.

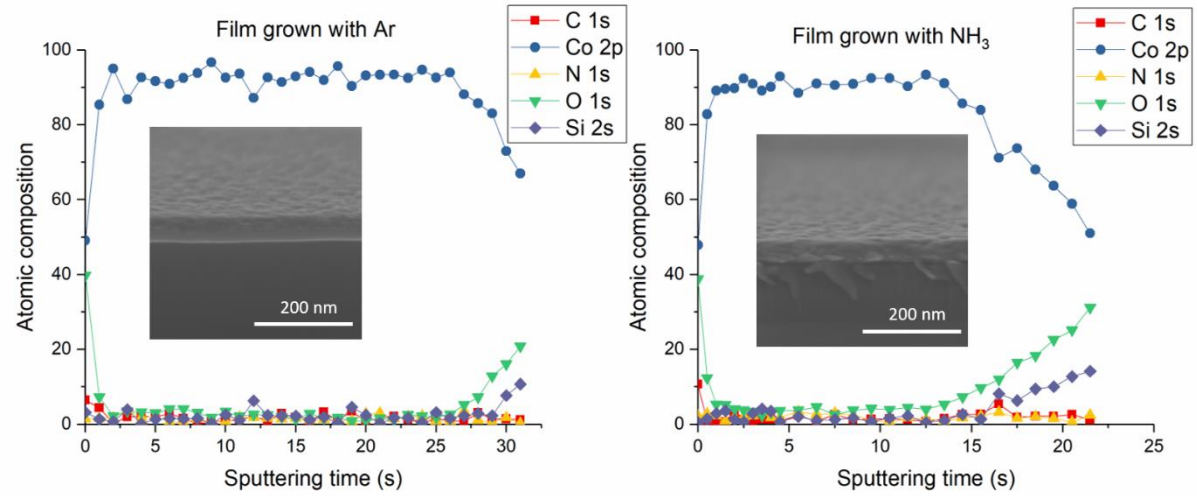

Figure 2.5. XPS sputter depth profiles of cobalt films grown from $Co_2(CO)_8$ at 70 °C with Ar (left) or ammonia (right). Thicknesses are 52 nm and 41 nm, respectively. The difference in sputtering time is due to different ion beam settings. Insets: SEM images of the samples, respectively.

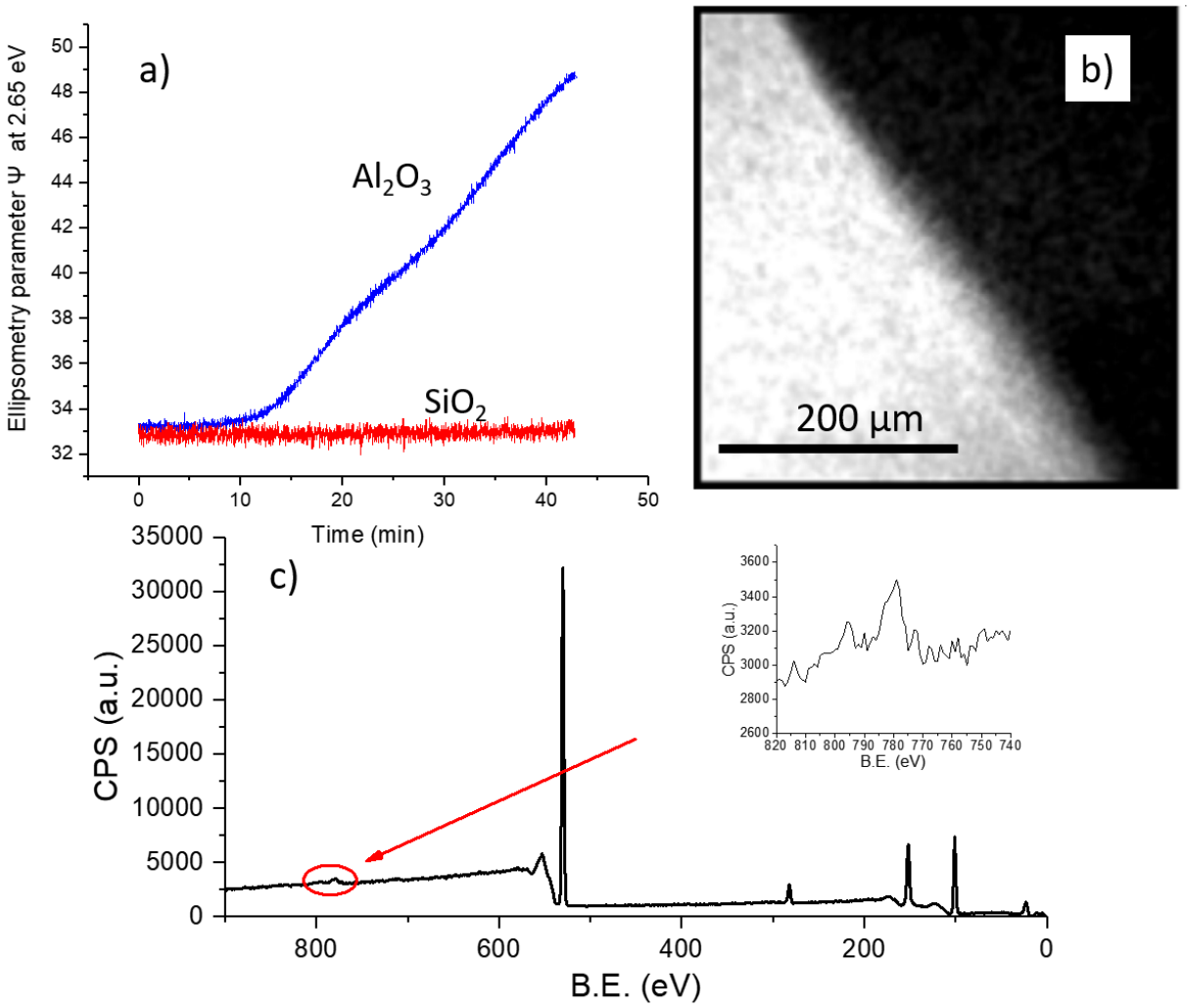

Figure 2.6. a) In situ ellipsometry parameter Ψ at a photon energy of 2.65 eV vs. time for Co film growth from $Co_2(CO)_8$ at 70 °C on SiO_2 and Al_2O_3 in the presence of NH_3 (curves are shifted vertically to facilitate comparison). b) XPS elemental map of cobalt (bright contrast) on a patterned substrate: lower left is Al_2O_3 and upper right is SiO_2. Precursor pressure is 0.018 mTorr, ammonia pressure is 4 mTorr, temperature is 70 °C, and growth time is 30 min. c) XPS survey spectrum of the SiO_2 surface for the same sample as in b).

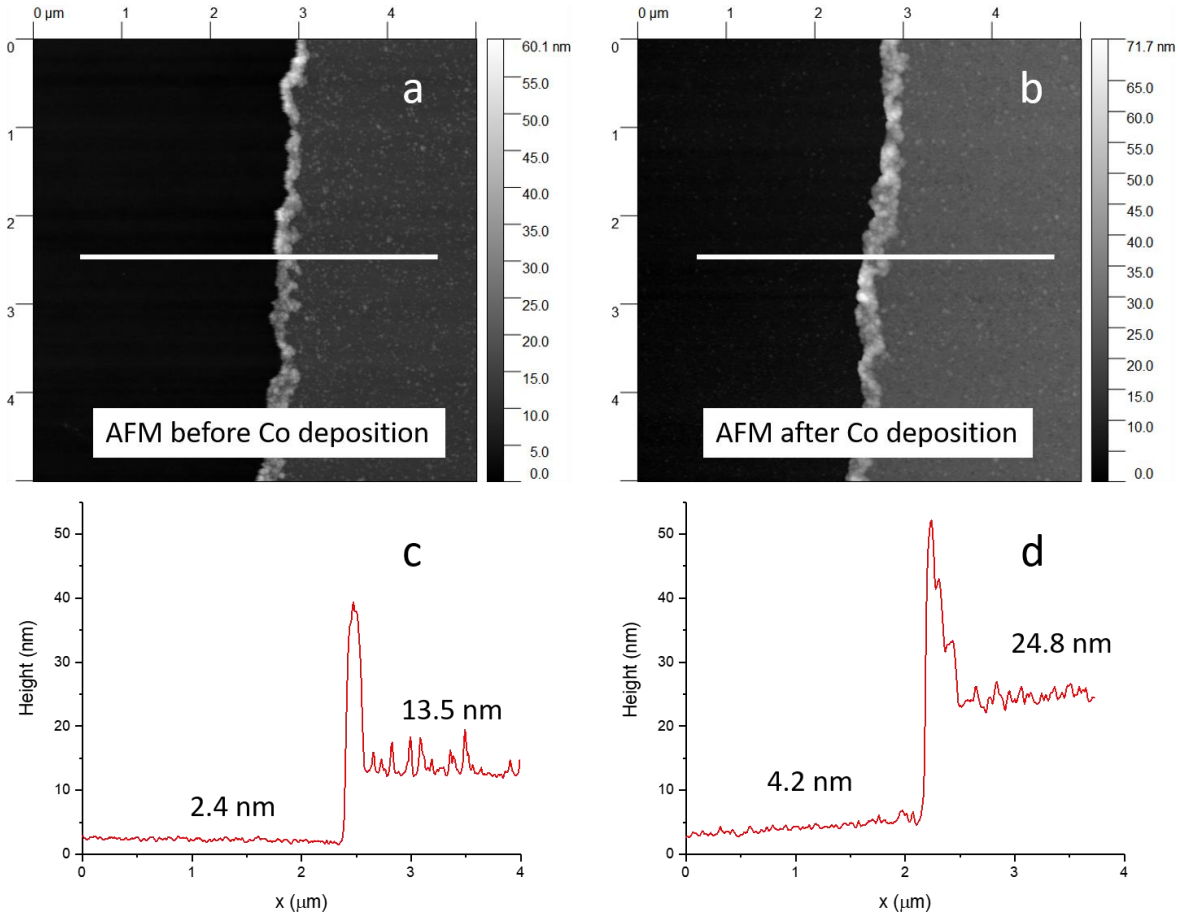

Figure 2.7. AFM images and height profiles of a patterned substrate and before Co deposition (a and c) and after Co deposition (b and d). Within each sample, the left side is SiO_2 and the right side is Al_2O_3. The numbers shown on top of the curves in c and d are average heights (excluding the spike at the interface, which is caused by imperfect lift-off of Al_2O_3 during sample preparation). The thickness of the Al_2O_3 layer is 13.5 – 2.4 = 11.1 nm (c) and the thickness of Al_2O_3 plus Co is 24.8 – 4.2 = 20.6 nm (d). Therefore, the Co film thickness is 20.6 – 11.1 = 9.5 nm.

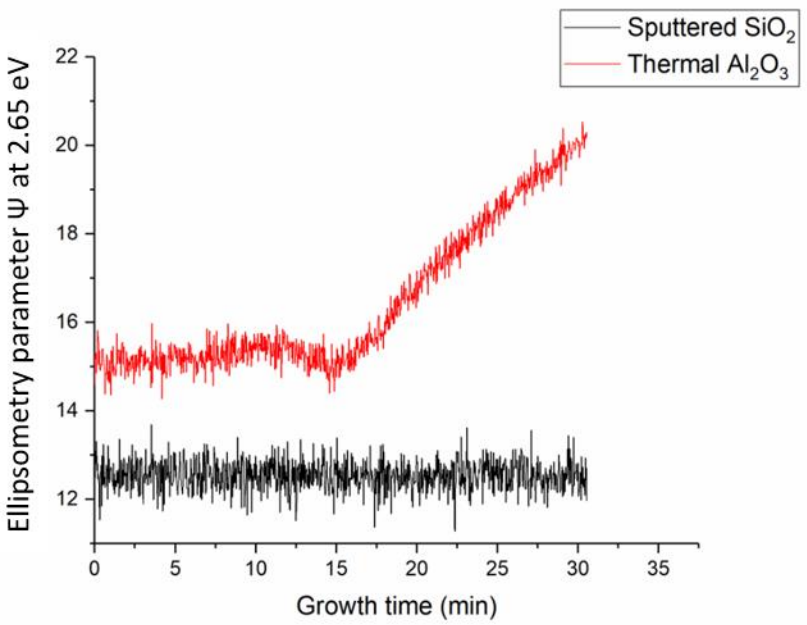

Figure 2.8. Real time ellipsometry study of Co growth from $Co_2(CO)_8$ at 70 °C on sputtered SiO_2 and on thermal Al_2O_3, both in the presence of NH_3. The $Co_2(CO)_8$ pressure is 0.018 mTorr and the NH_3 pressure is 4 mTorr. The SiO_2 substrate is fabricated by sputtering 10 nm SiO_2 onto 300 nm thermal SiO_2 (microelectronic grade) / Si substrate. The Al_2O_3 substrate is fabricated by e-beam evaporating 100 nm of Al on SiO_2 and then annealing in oxygen at 900 °C for 1 h.

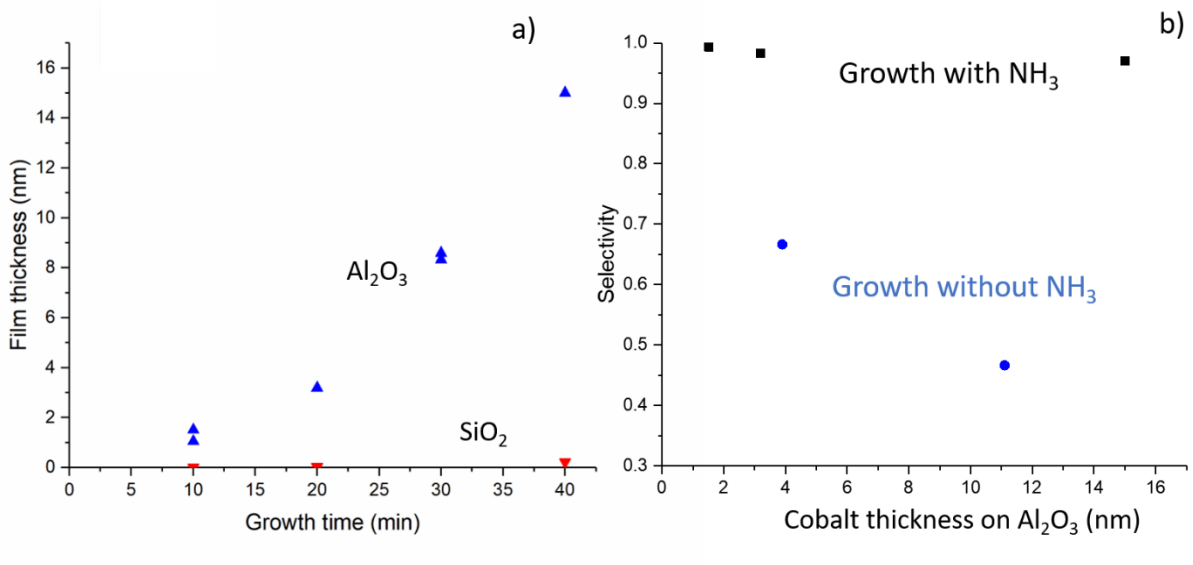

Figure 2.9. a) Film thickness vs. total growth time for deposition of Co from $Co_2(CO)_8$ at 70 °C on Al_2O_3 and SiO_2 substrates in the presence of NH_3. b) Selectivity for preferential growth on Al_2O_3 over SiO_2 substrates vs. Co film thickness on Al_2O_3, both with and without a co-flow of NH_3.

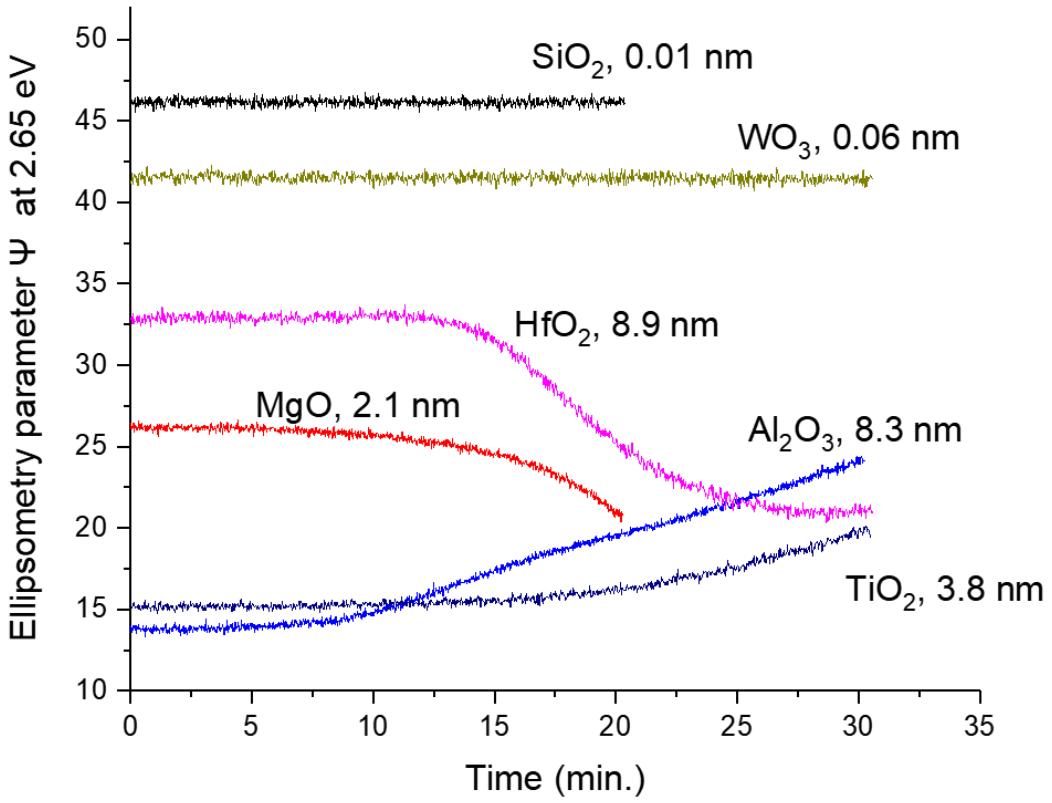

Figure 2.10. In situ ellipsometry parameter Ψ at a photon energy of 2.65 eV vs. time for Co film growth on acidic oxides (WO_3 and SiO_2) and on basic oxides (TiO_2, HfO_2, Al_2O_3, and MgO) in the presence of NH_3. Growth temperature is 70 °C and NH_3 pressure is 4 mTorr. The thicknesses are measured by XRF.

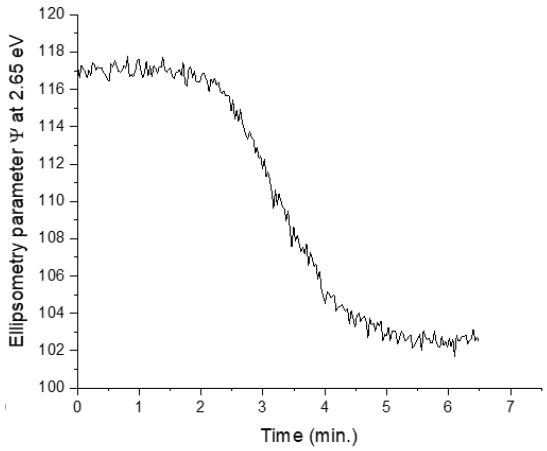

Figure 2.11. Real time ellipsometry study of Co growth from $Co_2(CO)_8$ at 70 °C on WO_3 in the absence of NH_3. The $Co_2(CO)_8$ pressure is 0.018 mTorr. Nucleation on WO_3 after a short nucleation delay, ~ 2 min.

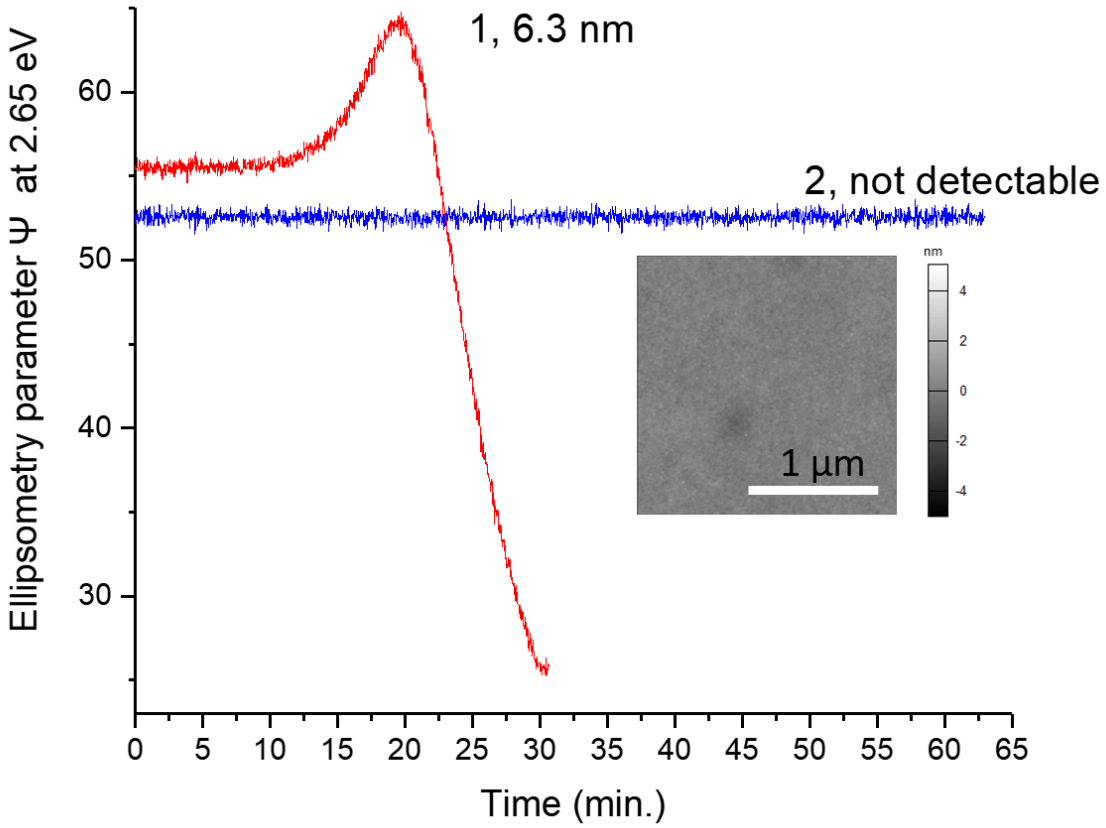

Figure 2.12. In situ ellipsometry parameter Ψ at a photon energy of 2.65 eV vs. time for Co film growth from 0.018 mTorr $Co_2(CO)_8$ and 4 mTorr NH_3 at 70 °C on 1) SiO_2 that has been annealed at 900 °C for 2 h (dehydroxylated SiO_2); 2) SiO_2 annealed at 900 °C for 2 h and afterward immersed in piranha solution for 10 min to afford fully hydroxylated SiO_2. The values shown in the figure are cobalt film thicknesses. Inset: AFM image of the sample described in 2.

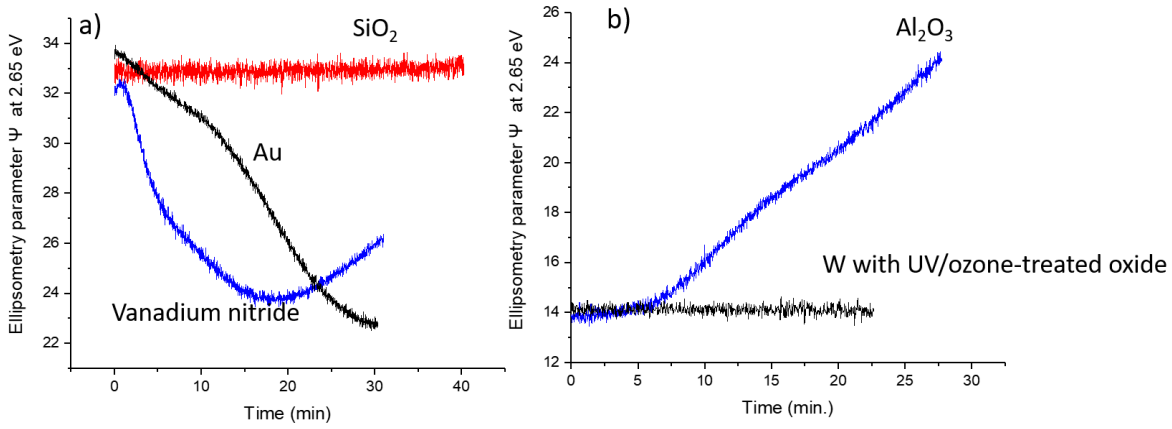

Figure 2.13. In situ ellipsometry parameter Ψ, at a photon energy of 2.65 eV, vs. time for Co film growth from $Co_2(CO)_8$ at 70 °C in the presence of NH_3 on a) SiO_2, Au and VN; b) Al_2O_3 and W with UV/ozone-grown oxide. Curves are shifted vertically to be displayed in the same range.

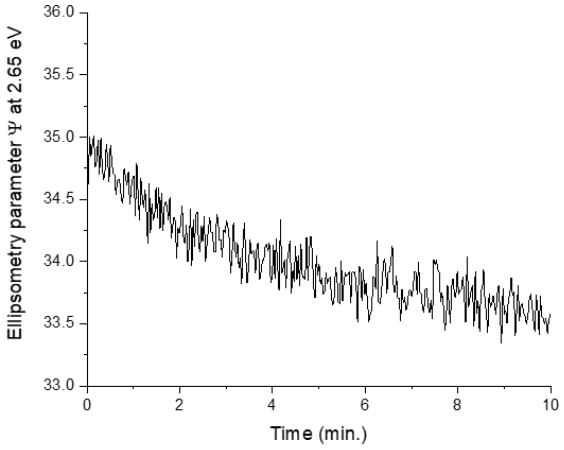

Figure 2.14. Real time ellipsometry study of Co growth from $Co_2(CO)_8$ at 70 °C on Au in the absence of NH_3. The $Co_2(CO)_8$ pressure is 0.015 mTorr. Nucleation on Au occurs immediately.

2.6 References

1. A. J. M. Mackus, A. A. Bol, and W. M. M. Kessels, "The use of atomic layer deposition in advanced nanopatterning," *Nanoscale* **6,** 10941-60 (2014).

2. J. F. Zheng, P. Chen, T. H. Baum, R. R. Lieten, W. Hunks, S. Lippy, A. Frye, W. M. Li, J. O'Neill, J. Xu, J. Zhu, J. Bao, V. Machkaoutsan, M. Badaroglu, G. Yeap, G. Murdoch, J. Bommels, Z. Tokei, and Ieee, *Selective co growth on cu for void-free via fill* (2015). [DOI: 10.1109/IITC-MAM.2015.7325663]

3. A. Mameli, M. J. M. Merkx, B. Karasulu, F. Roozeboom, W. M. M. Kessels, and A. J. M. Mackus, "Area-selective atomic layer deposition of sio2 using acetylacetone as a chemoselective inhibitor in an abc-type cycle," *Acs Nano* **11,** 9303-11 (2017).

4. W. L. Gladfelter, "Selective metallization by chemical-vapor-deposition," *Chemistry of Materials* **5,** 1372-88 (1993).

5. S. K. Song, H. Saare, and G. N. Parsons, "Integrated isothermal atomic layer deposition/atomic layer etching supercycles for area-selective deposition of tio2," *Chemistry of Materials* **31,** 4793-804 (2019).

6. Z. W. Li, R. G. Gordon, D. B. Farmer, Y. B. Lin, and J. Vlassak, "Nucleation and adhesion of ald copper on cobalt adhesion layers and tungsten nitride diffusion barriers," *Electrochem Solid St* **8,** G182-G5 (2005).

7. H. Li and B. P. Tonner, "Structure and growth mode of metastable fcc cobalt ultrathin films on cu(001) as determined by angle-resolved x-ray photoemission scattering," *Surf Sci* **237,** 141-52 (1990).

8. C. C. Yang, F. R. McFeely, P. C. Wang, K. Chanda, and D. C. Edelstein, "Selective chemical vapor deposition-grown ru for cu interconnect capping applications," *Electrochem Solid St* **13,** D33-D5 (2010).

9. M. Tagami, N. Furutake, N. Inoue, E. Nakazawa, K. Arita, Y. Hayashi, and Ieee, "Highly-reliable molecular-pore-stack (mps)-sioch/cu interconnects with cowb metal-cap films," *Proceedings of the 2009 Ieee International Interconnect Technology Conference***,** 11-3 (2009).

10. J. R. Lloyd, M. W. Lane, E. G. Liniger, C. K. Hu, T. M. Shaw, and R. Rosenberg, "Electromigration and adhesion," *Ieee T Device Mat Re* **5,** 113-8 (2005).

11. L. B. Henderson and J. G. Ekerdt, "Effect of phosphorus and carbon incorporation in amorphous cobalt films prepared by chemical vapor deposition," *Journal of the Electrochemical Society* **157,** D29-D34 (2010).

12. M. H. van der Veen, K. Vandersmissen, D. Dictus, S. Demuynck, R. Liu, X. Bin, P. Nalla, A. Lesniewska, L. Hall, K. Croes, L. Zhao, J. Bommels, A. Kolics, Z. Tokei, and Ieee, "Cobalt bottom-up contact and via prefill enabling advanced logic and dram technologies," *2015 IEEE International Interconnect Technology Conference and 2015 IEEE Materials for Advanced Metallization Conference***,** 25-7 (2015).

13. J. Kelly, J. H. C. Chen, H. Huang, C. K. Hu, E. Liniger, R. Patlolla, B. Peethala, P. Adusumilli, H. Shobha, T. Nogami, T. Spooner, E. Huang, D. Edelstein, D. Canaperi, V. Kamineni, F. Mont, S. Siddiqui, and Ieee, *Experimental study of nanoscale co damascene beol interconnect structures* (2016). [DOI: 10.1109/IITC-AMC.2016.7507673]

14. Y. Shacham-Diamand and Y. Sverdlov, "Electrochemically deposited thin film alloys for ulsi and mems applications," *Microelectronic Engineering* **50,** 525-31 (2000).

15. J. Gambino, J. Wynne, J. Gill, S. Mongeon, D. Meatyard, B. Lee, H. Bamnolker, L. Hall, N. Li, M. Hernandez, P. Little, M. Hamed, I. Ivanov, and C. L. Gan, "Self-aligned metal capping layers for copper interconnects using electroless plating," *Microelectronic Engineering* **83,** 2059-67 (2006).

16. M. M. Kerrigan, J. P. Klesko, and C. H. Winter, "Low temperature, selective atomic layer deposition of cobalt metal films using bis(1,4-di-tert-butyl-1,3-diazadienyl)cobalt and alkylamine precursors," *Chemistry of Materials* **29,** 7458-66 (2017).

17. C. C. Yang, P. Flaitz, P. C. Wang, F. Chen, and D. Edelstein, "Characterization of selectively deposited cobalt capping layers: Selectivity and electromigration resistance," *Ieee Electron Device Letters* **31,** 728-30 (2010).

18. S. W. Ryu, S. Kim, J. Yoon, J. T. Tanskanen, H. Kim, and H. B. R. Lee, "Area-selective chemical vapor deposition of co for cu capping layer," *Current Applied Physics* **16,** 88-92 (2016).

19. E. Mohimi, Z. V. Zhang, S. M. Liu, J. L. Mallek, G. S. Girolami, and J. R. Abelson, "Area selective cvd of metallic films from molybdenum, iron, and ruthenium carbonyl precursors: Use of ammonia to inhibit nucleation on oxide surfaces," *Journal of Vacuum Science & Technology A* **36,** 041507 (2018).

20. S. Jayaraman, Y. Yang, D. Y. Kim, G. S. Girolami, and J. R. Abelson, "Hafnium diboride thin films by chemical vapor deposition from a single source precursor," *Journal of Vacuum Science & Technology A* **23,** 1619-25 (2005).

21. S. Jayaraman, E. J. Klein, Y. Yang, D. Y. Kim, G. S. Girolami, and J. R. Abelson, "Chromium diboride thin films by low temperature chemical vapor deposition," *Journal of Vacuum Science & Technology A* **23,** 631-3 (2005).

22. H. Baumgartner, V. Fuenzalida, and I. Eisele, "Ozone cleaning of the si-sio2 system," *Applied Physics a-Materials Science & Processing* **43,** 223-6 (1987).

23. J. R. Vig, "Uv ozone cleaning of surfaces," *Journal of Vacuum Science & Technology a-Vacuum Surfaces and Films* **3,** 1027-34 (1985).

24. T. K. Talukdar, S. Liu, Z. Zhang, F. Harwath, G. S. Girolami, and J. R. Abelson, "Conformal mgo film grown at high rate at low temperature by forward-directed chemical vapor deposition," *Journal of Vacuum Science & Technology A* **36,** 051504 (2018).

25. C. Nilsson and J. Habainy, "Oxidation of pure tungsten in the temperature interval 400° to 900° c," Thesis, Lund University, 2013.

26. E. A. Wovchko, J. C. Camp, J. A. Glass, and J. T. Yates, "Active sites on sio2: Role in ch3oh decomposition," *Langmuir* **11,** 2592-9 (1995).

27. L. T. Zhuravlev, "The surface chemistry of amorphous silica. Zhuravlev model," *Colloids and Surfaces a-Physicochemical and Engineering Aspects* **173,** 1-38 (2000).

28. E. Borello, Dellagat.G, B. Fubini, C. Morterra, and Venturel.G, "Surface rehydration of variously dehydrated eta-alumina," *Journal of Catalysis* **35,** 1-10 (1974).

29. S. Shioji, M. Kawaguchi, Y. Hayashi, K. Tokami, and H. Yamamoto, "Rehydroxylation of dehydrated silica surfaces by water vapor adsorption," *Advanced Powder Technology* **12,** 331-42 (2001).

30. A. Kanta, R. Sedev, and J. Ralston, "Thermally- and photoinduced changes in the water wettability of low-surface-area silica and titania," *Langmuir* **21,** 2400-7 (2005).

31. S. Babar, E. Mohimi, B. Trinh, G. S. Girolami, and J. R. Abelson, "Surface-selective chemical vapor deposition of copper films through the use of a molecular inhibitor," *Ecs Journal of Solid State Science and Technology* **4,** N60-N3 (2015).

32. S. Babar, N. Kumar, P. Zhang, and J. R. Abelson, "Growth inhibitor to homogenize nucleation and obtain smooth hfb_2 thin films by chemical vapor deposition," *Chemistry of Materials* **25,** 662-7 (2013).

33. M. E. Gross, K. S. Kranz, D. Brasen, and H. Luftman, "Organometallic chemical vapor-deposition of cobalt and formation of cobalt disilicide," *J Vac Sci Technol B* **6,** 1548-52 (1988).

34. J. Lee, H. J. Yang, J. H. Lee, J. Y. Kim, W. J. Nam, H. J. Shin, Y. K. Ko, J. G. Lee, E. G. Lee, and C. S. Kim, "Highly conformal deposition of pure co films by mocvd using co-2(co)(8) as a precursor," *Journal of the Electrochemical Society* **153,** G539-G42 (2006).

35. S. Babar, "Role of growth inhibitors in nucleation and growth of thin film deposited by chemical capor deposition in high aspect ratio structures " Thesis, University of Illinois at Urbana-Champaign, 2013.

36. M. Bettge, Y. Li, B. Sankaran, N. D. Rago, T. Spila, R. T. Haasch, I. Petrov, and D. P. Abraham, "Improving high-capacity li1.2ni0.15mn0.55co0.1o2-based lithium-ion cells by modifiying the positive electrode with alumina," *Journal of Power Sources* **233,** 346-57 (2013).

37. M. Kosmulski, "Isoelectric points and points of zero charge of metal (hydr)oxides: 50 years after parks' review," *Advances in Colloid and Interface Science* **238,** 1-61 (2016).

38. K. M. Rao, G. Spoto, E. Guglielminotti, and A. Zecchina, "Spectroscopic investigation of the interaction of co2(co)8 with mgo and sio2," *J Chem Soc Farad T 1* **84,** 2195-207 (1988).

39. A. Comas-Vives, "Amorphous sio2 surface models: Energetics of the dehydroxylation process, strain, ab initio atomistic thermodynamics and ir spectroscopic signatures," *Physical Chemistry Chemical Physics* **18,** 7475-82 (2016).

40. E. Mohimi, Z. V. Zhang, J. L. Mallek, S. Liu, B. B. Trinh, P. P. Shetty, G. S. Girolami, and J. R. Abelson, "Low temperature chemical vapor deposition of superconducting vanadium nitride thin films," *Journal of Vacuum Science & Technology A* **37,** 031509 (2019).

41. A. Vesel, A. Drenik, R. Zaplotnik, M. Mozetic, and M. Balat-Pichelin, "Reduction of thin oxide films on tungsten substrate with highly reactive cold hydrogen plasma," *Surface and Interface Analysis* **42,** 1168-71 (2010).

42. H. G. Ang, G. K. Chuah, S. Jaenicke, and W. L. Loh, "Temperature-programmed decomposition of mo(co)(6) : Indication of surface reactions and cluster formation," *J Chem Soc Dalton***,** 1243-9 (1997).

43. H. G. Ang, K. S. Chan, G. K. Chuah, S. Jaenicke, and S. K. Neo, "Thermal-reactions of mo(co)(6) on metal-oxide surfaces," *J Chem Soc Dalton***,** 3753-8 (1995).

44. A. Brenner, D. A. Hucul, and S. J. Hardwick, "Remarkable decarbonylation of chromium, molybdenum, and tungsten hexacarbonyls supported on silica and the nature of these materials as heterogeneous catalysts," *Inorg Chem* **18,** 1478-84 (1979).

45. J. W. Klaus and S. M. George, "Sio2 chemical vapor deposition at room temperature using sicl4 and h2o with an nh3 catalyst," *Journal of the Electrochemical Society* **147,** 2658-64 (2000).

46. H. H. Lamb, B. C. Gates, and H. Knozinger, "Molecular organometallic chemistry on surfaces - reactivity of metal-carbonyls on metal-oxides," *Angew Chem Int Edit* **27,** 1127-44 (1988).

47. K. M. Rao, G. Spoto, and A. Zecchina, "Ir investigation of co adsorbed on co particles obtained via co2(co)8 adsorbed on mgo and sio2," *Journal of Catalysis* **113,** 466-74 (1988).

48. M. Kurhinen and T. A. Pakkanen, "Diffuse reflectance infrared spectroscopy study of co2(co)8supported on alumina," *Langmuir* **14,** 6907-15 (1998).

49. S. Suvanto, T. A. Pakkanen, and L. Backman, "Controlled deposition of co2(co)8 on silica in a fluidized bed reactor: Ir, chemisorption and decomposition studies," *Applied Catalysis A: General* **177,** 25-36 (1999).

50. S. Suvanto, P. Hirva, and T. A. Pakkanen, "Interaction of co(co)(x) with surface sites of sio2: Theoretical study," *Surf Sci* **465,** 277-85 (2000).

51. K. Muthukumar, H. O. Jeschke, R. Valenti, E. Begun, J. Schwenk, F. Porrati, and M. Huth, "Spontaneous dissociation of co(2)(co)(8) and autocatalytic growth of co on sio(2): A combined experimental and theoretical investigation," *Beilstein J Nanotechnol* **3,** 546-55 (2012).

52. K. Muthukumar, R. Valenti, and H. O. Jeschke, "Dynamics of tungsten hexacarbonyl, dicobalt octacarbonyl, and their fragments adsorbed on silica surfaces," *J Chem Phys* **140,** 184706 (2014).

53. R. L. Schneider, R. F. Howe, and K. L. Watters, "Interactions of cobalt carbonyls with oxide surfaces .2. Dicobalt octacarbonyl and tetracobalt dodecacarbonyl on silicas and aluminas," *Inorg Chem* **23,** 4593-9 (1984).

54. N. Homs, A. Choplin, P. Ramirez de la Piscina, L. Huang, E. Garbowski, R. Sanchez-Delgado, A. Theolier, and J. M. Basset, "Surface organometallic chemistry: Evidence of disproportionation of dicobalt octacarbonyl to cobalt(2+) bis[dicarbonylcobaltate(1-)] at the surface of partially hydroxylated magnesia," *Inorg Chem* **27,** 4030-3 (1988).

55. W. Hieber and J. Sedlmeier, "Über metallcarbonyle, lxii. Mitteil.): Über die reaktion des kobalt-tetracarbonyls mit verschiedenartigen basen ii)," *Chemische Berichte* **87,** 25-34 (1954).

56. A. Zecchina, G. Spoto, E. Garrone, and A. Bossi, "Spectroscopic study of carbon monoxide adsorption on cobalt(ii) oxide-magnesium oxide solid solutions. 3. Carbon monoxide adsorption on aggregated cobalt(2+) ions," *The Journal of Physical Chemistry* **88,** 2587-91 (1984).

57. F. Arena, R. D. Chio, and G. Trunfio, "An experimental assessment of the ammonia temperature programmed desorption method for probing the surface acidic properties of heterogeneous catalysts," *Applied Catalysis A: General* **503,** 227-36 (2015).

2.7 Supplementary Materials

Influence of exposure to atmosphere and UV-ozone cleaning

An important issue is whether the kinetics of nucleation depend on the sample history. To test the role of surface treatments, we first examined the nucleation of MoC_x films from the precursor $Mo(CO)_6$ on thermally grown SiO_2 that had been exposed to laboratory air for several months – which can result in the adsorption of hydrocarbons and other contaminants. As noted in the text of this article, growth from $Mo(CO)_6$ is significantly different from that of $Co_2(CO)_8$; the point here is to test the reactivity of the SiO_2 surface. Under CVD conditions that afford prompt nucleation of MoC_x on clean SiO_2 surfaces, only a small density of nuclei formed on the air-exposed surfaces (Supplementary Figure 2.1a). In a second experiment, the air-exposed surface was cleaned before deposition by rinsing it with acetone, IPA, and DI water. The nucleation density on this surface was the same as on the uncleaned, air-exposed surface, so it is clear that the rinsing does not remove all the surface adsorbates. In a third experiment, an air-exposed surface was cleaned as above, then exposed to UV ozone for 10 min. On this surface, the density of nuclei was improved (Supplementary Figure 2.1), showing that UV ozone can remove surface contaminants.[1,2]

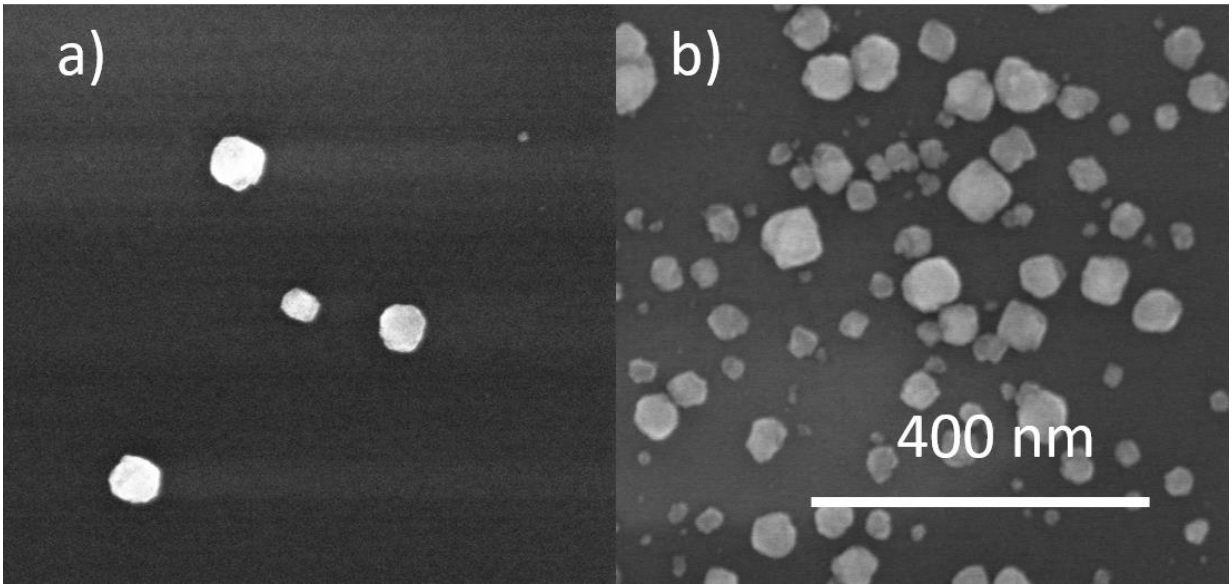

Supplementary Figure 2.1. SEM image of MoC_x nuclei on a) SiO_2 without cleaning (exposed in lab air for several months); b) SiO_2 cleaned by acetone/IPA/deionized water rinse followed by UV ozone treatment. The growth conditions are: temperature 200 °C, $Mo(CO)_6$ pressure 0.025 mTorr, time 3 min.

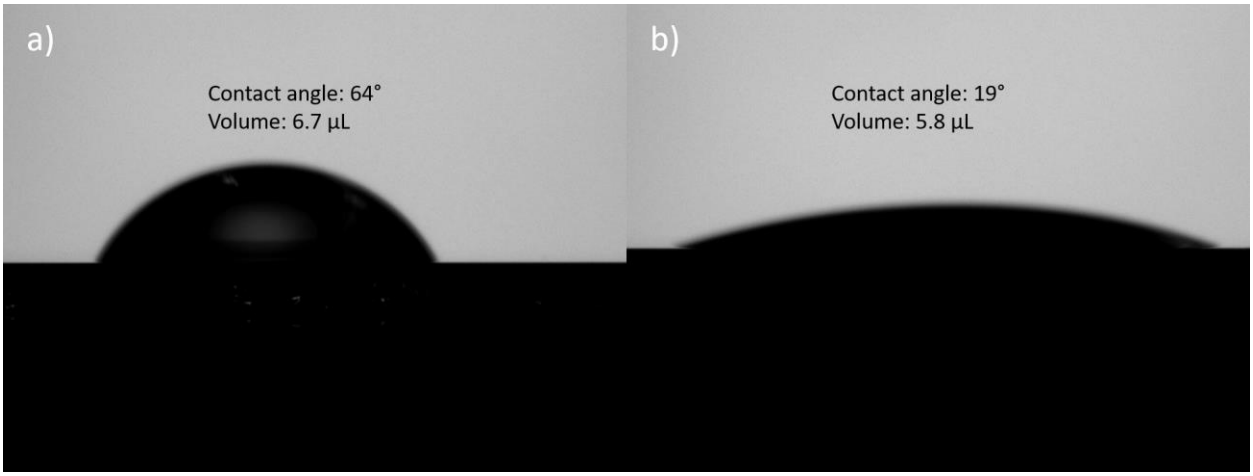

Supplementary Figure 2.2. Contact angle measurement on SiO_2 with (a) and without (b) exposure to UV ozone for 10 min.

1. J. R. Vig, "Uv ozone cleaning of surfaces," Journal of Vacuum Science & Technology a-Vacuum Surfaces and Films 3, 1027-34 (1985).

2. H. Baumgartner, V. Fuenzalida, and I. Eisele, "Ozone cleaning of the si-sio2 system," Applied Physics a-Materials Science & Processing 43, 223-6 (1987).

CHAPTER 3

ULTRA-SMOOTH COBALT FILMS ON SILICON OXIDE: CVD USING A NUCLEATION PROMOTER AND A GROWTH INHIBITOR

3.1 Introduction

Chemical vapor deposition (CVD) can afford thin films that are extremely conformal, e.g., a step coverage of 90-95% in trenches of aspect ratio up to 20:1, when the effective sticking (reaction) coefficient of the precursor with the film growth surface is small. However, the surface roughness can be several nm or larger when the film is deposited on a relatively unreactive substrate; examples include the growth of HfB_2 (a metallic ceramic barrier layer) [1] or cobalt [2,3] on SiO_2. For films only a few nm thick, there may be pinholes or, in extreme cases, a lack of continuity. Roughness is amplified when the nucleation process is slow or occurs with low areal density: the nuclei which form early in the process grow relatively tall before the surface reaches full coverage (coalescence). In addition, roughness that develops during the initial stages of film growth cannot be smoothed out during subsequent film growth, even under highly conformal conditions: we have shown that the long-range (high *k*) component persists, but is not detected by in-situ spectroscopic ellipsometry [4,5].

Kinetically, the development of initial roughness can be described in terms of the area density of possible nucleation sites, the time dependence of film nucleation (rate of nucleation), and the rate of film growth on those nuclei.

As we describe below, the smoothest film results when the precursor has a high probability of reaction with the substrate surface, but a low probability of reacting with the surface of the deposited material, i.e., *the ratio of the nucleation rate to the growth rate is large*. Under those conditions, a high areal density of small nuclei form on the substrate, then growth of these nuclei (possibly accompanied by continued nucleation) leads to coalescence and smoothing within the first few nm of deposited thickness. Similar ideas were reported from literatures of electrodeposition [6,7] and casting [8]. In the area of vapor phase deposition, the argument of the

ratio changing film morphology is demonstrated either by increasing nucleation rate [9-14] or reducing growth rate [1,15-19], however, is not explicitly elaborated and not demonstrated by changing both nucleation rate and growth rate.

Several methods have been shown to increase the nucleation rate. (i) A material with a reactive surface (often metallic), such as TiN [20], can be pre-deposited as a 'nucleation layer'. This presupposes that the chosen material nucleates well on the oxide surface to afford a reasonably smooth thin film. However, this approach has disadvantages in microelectronics fabrication: the nucleation layer consumes part of the width of vias and trenches, which increases the electrical resistance of the interconnect. It must also be possible to grow the layer conformally in deep features, and under conditions (e.g., substrate temperature) which are compatible with subsequent processing steps. Alternatively, the starting surface can be pretreated by (ii) a flux of molecules in vapor [9,10] or liquid [11] or (iii) exposure to energetic particles, such as plasma [12-14] to enhance nucleation.

It is also possible to decrease the film growth rate without substantially altering the nucleation rate on the starting substrate. This is accomplished by adding a flow of molecular inhibitor to the flow of CVD precursor; the inhibitor is selected because it binds weakly to substrate but more strongly to the surface of the deposited film, which affords the desired differential effect. This method has been reported to afford higher nucleation density and smoother films in a few systems: HfB_2 grown from $Hf(BH_4)_4$ using NH_3 as the inhibitor [1], Cu grown from Cu(hfac)(VTMS) using VTMS as the inhibitor [15], Ru grown from $Ru(EtCp)_2$ using CH_3I or C_2H_5I as the inhibitor [16-18] and Ru grown with $Ru_3(CO)_{12}$ using CO as the inhibitor [19].

Here we report a CVD method to grow extraordinarily smooth cobalt films on SiO_2 substrates. Cobalt is of strong interest in microelectronics for back-end metallization and as a transistor contact; compared with copper, cobalt has a greater electromigration resistance and a lower diffusion rate in Si and SiO_2 [21,22]. However, CVD of cobalt on SiO_2 typically forms isolated nuclei (Chapter 2), and full coalescence does not occur until a thickness of several nm; the roughness that results from sparse nucleation limits the application of cobalt in nanoscale device features [3,23]. We show that the sequential use of nucleation enhancement and growth inhibition dramatically reduces the roughness of 1-2-nm thick films. Pre-treatment involves

exposure of the SiO_2 surface to tetrakis(dimethylamino)metal precursors, TDMA-M, where M = Ti, Hf, or V; this affords a self-limiting, sub-monolayer coverage of a M-containing intermediate (~ 4 atoms per nm^2). Such molecules were reported to enhance nucleation for CVD of Al from dimethyl aluminum hydride [24] and Co from Hexacarbonyl(3,3-dimethyl-1-butyne)dicobalt (CCTBA) [10]. Then CVD is carried out using the $Co_2(CO)_8$ precursor with a co-flow of ammonia as a growth inhibitor.

3.2 Experimental

CVD experiments are performed in a cold wall high vacuum chamber of high vacuum construction described elsewhere [25,26]; the base pressure is 1×10^{-7} Torr, most of which is H_2. The pressure in the chamber background is measured by MKS Baratron® capacitance manometer (390HA-00001). Microelectronic grade Si wafers with 300 nm thermal SiO_2 are used and degreased by washing successively with acetone, IPA, and deionized water, and then are cleaned by UV ozone treatment for 10 min before the substrates are loaded into the chamber. We showed in a previous paper [3] that the preparation of a clean substrate surface is critical in order to obtain reliable and consistent data on nucleation; the UV-ozone treatment is particularly helpful in that regard. Substrates are radiatively heated to 70 °C, as measured by a K-type thermocouple attached to the front of the sample holder.

The precursor $Co_2(CO)_8$ (Sigma Aldrich) is sold as a mixture with 1-10 % hexane to improve shelf life; the hexane is removed by evacuation before the first use of the precursor. The hexane-free precursor is placed in a glass container, which is immersed in a water bath and delivered to the chamber without a carrier gas through a 0.4 cm i.d. stainless steel tube aimed at the substrate. Variation of the precursor pressure (0.01 to 0.035 mTorr) affects the growth rate but not morphology (roughness); we chose to do most of our studies at a background $Co_2(CO)_8$ pressure of 0.025 mTorr in the chamber. Forward-directed gas streams, however, produce a higher flux at the substrate surface than indicated by the background chamber pressure.

Tetrakis(dimethylamino)vanadium (TDMAV), tetrakis(dimethylamino)titanium (TDMAT), tetrakis(dimethylamino)hafnium (TDMAH), and tetrakis(dimethylamino)silane (TDMAS) are supplied by Sigma-Aldrich and used as received. They are maintained in separate

metal containers and delivered to the chamber at room temperature without carrier gas. The pressure of these molecules in the chamber is ~ 5×10^{-6} Torr. For the samples with the pre-treatment step, the SiO_2 surface is exposed to TDMA-M, where M = Ti, Hf, or V, at 70 °C. Cobalt deposition is performed 5-10 min after the pre-treatment, to avoid the effect of residual TDMA-M molecules in the chamber.

Research grade ammonia (99.992%) is delivered into the chamber via a mass flow controller (or a needle valve at lower flow rates) through a separate line to establish desired pressures.

Real-time spectroscopic ellipsometry (SE) is used to monitor the adsorption of TDMA-M molecules and onset of cobalt deposition. We do not use SE to estimate surface roughness because SE is not sensitive to roughness on longer lateral length scales [4]. The areal density of metal atoms is measured by ex-situ by X-ray fluorescence (Shimadzu EDX7000); we report an equivalent film thickness calculated from the bulk density of cobalt. Film roughness is measured by atomic force microscope (Asylum cypher) and surface morphology is imaged by scanning electron microscope (Hitachi 4800). Nuclei densities are best estimates (total error not exceeding 20%) based on counting nuclei within a 200 × 200 nm square SEM image; the error arises because nuclei that are close to one another are difficult to count (e.g., Figs. 3.2, 3.5 and 3.6c).

3.3 Results and Discussion

3.3.1 TDMA-M (M=V, Hf, Ti) adsorption on SiO_2

We investigate the adsorption of TDMAV on SiO_2 at 70 °C by turning on the flux and measuring the SE signal at 2.65 eV; it rises quickly but saturates in ~ 10s (Fig. 3.1a), indicating that TDMAV adsorbs to saturation. Four SiO_2 substrates are exposed to TDMAV for different periods of time (10, 30, 60, and 600 s). After 10 s, the areal density of vanadium atoms is 85 % of the saturated value, 4 atoms per nm^2 (FIG. 3.1b). The pressure of TDMAV in the chamber is too low to be measured by the capacitance manometer (< 10^{-6} torr), which implies that the sticking coefficient is high. The average density of OH on the SiO_2 surface is ~ 4.6 atoms per nm^2, indicating that TDMAV covers essentially every site. Other inhibitors, TDMAT and

TDMAH, exhibit similar behavior: the areal densities of titanium and hafnium atoms both saturate at ~ 4.5 /nm^2.

These observations are consistent with literature reports in which TDMA-M (M = V, Hf, Ti) are used as precursors for the ALD of metal nitrides or oxides: they undergo self-limiting adsorption on SiO_2 by losing one or two dimethylamine (DMA) ligands [27-29] when the temperature is below that at which CVD occurs (<175 °C for TDMAV [30], ~ 225 °C for TDMAT [28] and > 250 °C for TDMAH [31]). For all three molecules, we have experimentally confirmed the onset temperatures for CVD.

3.3.2 Effect of adsorbed layer of TDMA-M on nucleation

In order to make comparisons with later results, we first describe the deposition of cobalt from the carbonyl precursor $Co_2(CO)_8$ at 70 °C in the absence of nucleation promoters or growth inhibitors. Under these conditions, Co nucleation on SiO_2 is poor (Fig. 3.2a) [3]: the density of Co nuclei is small (3×10^{11} /cm^2). After deposition for 3 min, the films are 1-9 nm thick and have a root-mean-square (rms) roughness of 2.0 to 2.7 nm, with a broad height distribution (Fig. 3.3). For example, a film with mean thickness 1.3 nm has a maximum height of ~ 15 nm.

A significantly different film morphology is seen when the substrates are pretreated with TDMA-M molecules for 2 min at ~ 5×10^{-6} Torr. The density of nuclei (1×10^{12} /cm^2) is larger by a factor of three, and the roughness of 1.0 nm is decreased by a factor of over two, i.e., TDMA-M molecules serve as a nucleation promotor for cobalt deposition. The Co films grown on these pretreated surfaces have lower rms roughnesses of 0.6 to 1.3 nm, and the height distribution function is much narrower. For a Co film with a thickness of 1.1 nm, the maximum height is reduced to 8 nm. Pretreatments with TDMAV, TDMAT, and TDMAH give similar results.

The resulting surface-bound $M(DMA)_x(O\text{-}Si\equiv)$ intermediate after pretreatment must somehow promote cobalt nucleation, although the mechanism by which this occurs is unknown. These surface species may slow the diffusion of adsorbed cobalt precursor on the SiO_2 surface (thus promoting the formation of a larger density of small nuclei rather than the loss of precursor to larger nuclei); it may reduce the effective sticking coefficient of the cobalt precursor (and

slowing growth of the existing nuclei [32]); For the films on pretreated surface, the nuclei do have smaller diameters and the mean thickness is slightly smaller (1.1 vs. 1.3 nm) for the same growth time, which appears to support the hypothesis.

However, we cannot rule out that slower growth is simply originated from other mechanism. For example, as a possible byproduct, dimethylamine (DMA) may slow down initial Co growth rate. This can only occur in nucleation step. Once the surface is covered by cobalt, there is no source of DMA. To examine this mechanism, we co-flow 1 mTorr of DMA during Co deposition from $Co_2(CO)_8$. The growth rate is significantly reduced, from 1.5 nm/min to 0.1 nm/min.

3.3.3 Effect of growth inhibitors on film roughness

As we already discussed in in a previous paper [1], film roughness can be reduced by co-flowing a growth inhibitor along with a CVD precursor. In this approach, the inhibitor binds strongly to – and reduces the growth rate of – nuclei but binds only weakly to the substrate surface and does not impede the formation of additional nuclei. The surface reaches coalescence with a relatively large areal density of similarly sized small nuclei; in the absence of a distribution of large and small nuclei, the initial roughness is very low.

We have shown in chapter 2 that ammonia can inhibit the growth of Co from $Co_2(CO)_8$ [3]. In that previous study, we found that, at 70 °C and a precursor pressure of 0.018 mTorr, the steady-state growth rate on SiO_2 decreases from 1.5 nm/min in the absence of ammonia to 0.8-1.1 nm/min at an ammonia co-flow of 0.1 mTorr, and becomes constant at 0.4-0.5 nm/min for an ammonia co-flow of ~ 0.5 mTorr and above. We also found that, for a film thickness of ~ 1.5 nm, the film roughness decreased from ~ 2.2 nm in the absence of ammonia to 1.1-1.4 nm in the presence of ~ 0.1 mTorr of ammonia.

We have carried out a more thorough study of the effect of ammonia on the growth of Co onto SiO_2 from $Co_2(CO)_8$ in the absence of any surface pretreatment. At high pressure ammonia significantly inhibits the Co nucleation rate on SiO_2; this effect competes with, and ultimately undermines, the smoothing effect due to the reduction in growth rate. Due to these effects, with

increasing ammonia pressure the roughness of Co films initially decreases then increases again, up to a pressure where nucleation becomes too slow for practical experiments.

The experimental results are as follows. In the absence of ammonia, Co growth is relatively fast: 1.3 nm is deposited on SiO_2 in 3 min. The roughness is 2.0 nm (Figs. 3.4a and 3.5). When ammonia pressure is 0.1 mTorr, growth of a 1.4 nm film takes 9 min (3 times longer)., however, nucleation rate is not much affected (Fig. 3.5). The longer growth time allows for the formation of more nuclei, about 8×10^{11} /cm^2 (Fig. 3.6), which is more than twice than that of a film with similar thickness grown in the absence of ammonia (3×10^{11} /cm^2 in Fig. 1a). The roughness is reduced to 0.9 nm (Fig. 3.4b and FIG. 3.5). When the ammonia pressure is increased to 0.5 mTorr, the growth rate is reduced to 0.4~0.5 nm/min. In 20 min, a film of only 0.5 nm is grown on SiO_2. The film has a roughness of 0.9 nm and the height distribution (Fig. 3.4g) is similar to Fig. 4f, with a broader peak whose center is shifted towards zero. The maximum height is close to Fig. 4f. Slower growth rate is supposed to afford a smoother film, but ammonia inhibits nucleation rate by a factor of 3 at the pressure of 0.5 mTorr (Fig. 3.5) as nuclei density is about 6×10^{11} /cm^2 in a growth time of 20 min. When pressure is increased to 4.0 mTorr, growth rate is not inhibited further but nucleation is practically halted (Fig. 3.5). In 40 min, a film of only 0.3 nm is grown, with sparse nuclei on the surface (Fig. 3.4d). The sample surface is rough (1.5 nm) with a broad height distribution function (Fig. 3.4h). This result is consistent with the earlier study in chapter 2, where ammonia at high pressure can inhibit nucleation strongly on the SiO_2 surface [3,33].

3.3.4 Combination of surface pretreatment and growth inhibitor

We showed in the previous sections that films of Co grown by CVD onto SiO_2 from $Co_2(CO)_8$ can be made less rough can be obtained in two ways: by enhancing nucleation or by inhibiting the growth of nuclei. Here we show that the films are even smoother when both methods are used together.

SiO_2 substrates are pretreated by TDMAV and then exposed to a coflow of $Co_2(CO)_8$ precursor and NH_3 inhibitor. When the ammonia pressure is small (0.1 mTorr), the roughness (Fig. 3.7a, line 2) is improved slightly (roughness is 0.6 nm for a film of 1.5 nm) compared with samples that only received the pretreatment. Many nuclei coalesce with each other (Fig. 3.7c),

making it difficult to count density, but conservatively the density is ~1.1×10^{12} /cm^2. When the ammonia pressure is raised to 4 mTorr, the growth rate and the roughness are significantly reduced. Note that on a bare (untreated) SiO_2 substrate, this pressure of ammonia strongly inhibits nucleation (no growth occurs), whereas nucleation occurs promptly on pretreated SiO_2 (Fig. 3.8). For a 1.6 nm thick film, the roughness is ~ 0.3 nm (Fig. 3.7d) and the height distribution is very narrow (Fig. 3.7a, line 1), better than any other sample. The film is continuous and free of isolated nuclei, within the resolution of the SEM (Fig. 3.7c). Table 3.1 summarizes the conditions under which the films were deposited, and the resulting film morphologies.

In principle, the adsorbed TDMAV layer might be modified upon exposure to NH_3; at temperatures above 150 °C, a co-flow of TDMAV and NH_3 affords VN film growth by CVD [30]. To check for any possible interaction at 70 °C, SiO_2 surfaces are pretreated with TDMAV in the presence of ammonia (4 mTorr) for 2 min, then the ammonia is evacuated for 5-10 min and Co is deposited from the $Co_2(CO)_8$ precursor alone. The resulting roughness, 1 nm for a film of 5.8 nm, is similar to that of samples prepared without the ammonia during pretreatment.

3.3.5 Evolution of surface roughness

The evolution of surface roughness with film thickness depends very strongly on the initial morphology (i.e., after the films coalesces), for two reasons. First, the development of roughness is an instability inherent in the growth process, whose magnitude depends on the precursor sticking probability. If the initial layer at the point of coalescence is very smooth, then the onset of the roughening instability is postponed. Second, roughness on longer in-plane length scales cannot be removed by even the most conformal growth conditions [5,34].

To investigate the dependence of roughness on the nucleation step, we grew thick Co films from the $Co_2(CO)_8$ precursor alone on two SiO_2 substrates, one without and one with TDMA-V pretreatment. For growth on a surface without pretreatment, the nuclei are sparse when the film is thin (similar to Fig. 3.3a). For a film 8.5 nm thick, the surface roughness is 2.7 nm and the height distribution function is broad (Fig. 3.8, red line), similar to that of a thinner film (Fig. 3.2b, red line). For growth with substrate pretreatment, the nuclei are dense (similar to Fig. 3.3b). For a film 8.9 nm thick the roughness is only 1.2 nm (Fig. 3.9, blue line). Thus, a

smooth initial layer with a high density of nuclei leads to a very much smoother film in the later stage of film growth.

A film prepared by the process described in section D has a roughness of only 0.35 nm for a thickness of 3.4 nm (Fig. 3.10, black line). However, if the film is prepared by the process in section D to a thickness of ~1.5 nm, then is grown with precursor only (to speed up the growth rate), the roughness is 0.9 nm for a total thickness of 4.9 nm (Fig. 3.10, red line). It is well established that the growth of roughness is driven by shadowing effects such that peaks receive slightly more flux than valleys, and that the effects of shadowing are reduced by conformal growth conditions: when the effective sticking coefficient is low, precursor re-emission helps to homogenize the flux on all surfaces [35,36]. *Under the present conditions, to obtain a Co film with roughness of ~ 1 nm, it is sufficient simply to use substrate pre-treatment. However, to reduce the roughness to < 0.5 nm, growth must be carried out using an ammonia coflow.*

As noted above, ammonia inhibits nucleation on bare (untreated) SiO_2. This effect produces a surprising result when Co is grown, with ammonia, on top of a sparse nucleation layer, similar to that in Fig. 3a: the use of ammonia does not make the surface smoother, but instead makes it rougher. A sparse initial layer is grown to a thickness of 1.5 nm, then an additional 7.1 nm is deposited with ammonia (slowly, over 44 minutes); the resulting roughness is 4.5 nm (Fig. 3.11). We interpret that this occurs because ammonia prevents the generation of additional nuclei on exposed areas of the SiO_2 surface, thus, growth occurs only be enlarging the initial, widely-spaced nuclei.

3.3.6 Mechanistic framework

Here we provide a mechanistic framework for the growth of a smooth and dense nucleation layer that is consistent with the above results. Generally, in nucleation step of CVD, precursor molecules are impinging on the substrate surface [37], where they are adsorbed or reflected. Adsorbed precursors can desorb from the surface, diffuse to existing nuclei, or decompose to form adatoms. Adatoms can form new nuclei by itself or through combination to reach critical size [38]. In the case of metal deposition on dielectrics, nucleation follows island or Volmer-Weber mode, where growth of nuclei is favored rather than nucleation. In such case, precursor molecules landing on or diffusing to existing nuclei will be more likely to decompose

to film materials rather than that on substrate surface. And thus, to disfavor growth of nuclei, either decomposition rate, or precursor transport can be selectively inhibited on nuclei. Precursor transport inhibition is easier compared with decomposition rate, through site blocking [1,15,19,34] or reduction of surface diffusion [39]. In fact, reducing diffusion can also enhance nucleation by reducing loss of precursor to nuclei, as we discussed in previous section. We cannot tell whether adsorbed TDMA-M layer and ammonia can affect surface diffusion but we can still tell whether they have effect on nucleation rate and growth rate. Except for surface diffusion, bulk diffusion also exists in some systems, leading to island redistribution. However, when the film deposition temperature is low relative to its melting point, bulk diffusion is negligible and will not be considered here. In the case, the initial surface morphology is only governed by the nucleation rate and the film growth rate onto nuclei, as follows. The films are not continuous until a certain thickness has been deposited, which sets a lower limit of thickness for a continuous film (Fig. 3.12 a-b). However, if the formation of nuclei is rapid compared with the growth rate, then then density of nuclei is higher; coalescence occurs at a smaller thickness and with a narrower size distribution of nuclei (Fig. 3.12 c). When the nucleation rate is unchanged but the growth rate is reduced (Fig. 3.12d), the density of nuclei, for the same growth time, is identical to Fig. 3.12a. However, as growth proceeds over a longer time scale, more nuclei form (Fig. 3.12e), leading to a smoother final film (Fig. 3.12f). Note that the results in Figs. 3.11c and 3.12f are identical (although a longer time is required to achieve 3.12f), because what matters is the *ratio* of the nucleation rate to the growth rate.

Preliminary experiments illustrate the strong differences between candidate molecules. In general, to achieve ultra-smooth films, we need to find ways to enhance nucleation and slow down growth rate. The mechanism for nucleation enhancement from TDMA-M molecules is not well established yet, and thus it is not easy to discover a substance that acts like TDMA-M does in the present system and to provide guideline for other systems. We try TDMA-Si as the pretreatment molecules but it seems not to adsorb well at our process temperature. Trimethylaluminum (TMA) is a great ALD precursor and it was discovered to improve nucleation for Pt deposition [9]. TMA molecules adsorb well on the surface at 70 °C, however, there is no evidence that TMA layer can enhance nucleation of cobalt from $Co_2(CO)_8$. Hexacarbonyl(3,3-dimethyl-1-butyne)dicobalt (CCTBA) is an ALD precursor for cobalt, and it adsorbs well on the surface. However, we find no evidence that CCTBA can enhance nucleation.

A working hypothesis is that the molecule must contain an early-transition metal (like Ti, V or Hf) to stimulate precursor dissociation. However, the ligands on the promoter may also play a role in precursor adsorption and reaction. In the future work, molecules like $Ti(Cl)_4$ or titanium butoxide could be trialed as nucleation promoters because they contain the same transition metal but different ligands.

Selection of growth inhibitor should bind strongly to film surface and reduces the growth rate of islands, but binds weakly to the substrate surface and does not impede the formation of additional nuclei. Also, inhibitor molecules should not compromise the performance of nucleation enhancement from pretreatment of adsorbed molecules, i.e., inhibitor should not promote decomposition or desorption of pretreatment molecules. Dimethylamine (DMA) is a stronger growth inhibitor than ammonia and it also works well to smoothen cobalt deposition, along with TDMA-M molecules. However, it is not clear yet whether DMA can introduce contamination into the films because the growth rate is too low to grow a film thick enough for ex-situ atomic profiling.

3.4 Conclusion

We demonstrate a CVD process to deposit ultra-smooth cobalt films on SiO_2: for example, at a thickness of ~ 1.6 nm, the rms surface roughness is ~ 0.3 nm. The process involves first pretreating the substrate to TDMA-M (M = V, Ti, Hf) molecules to improve the nucleation of cobalt; adsorption of these molecules is self-limiting. Next, cobalt is deposited from $Co_2(CO)_8$ with a co-flow of NH_3 as a growth inhibitor. On a SiO_2 surface that has not been pretreated, ammonia can either smoothen or roughen the deposited Co film, depending on the pressure. This behavior occurs because at low pressure ammonia serves primarily as a growth inhibitor, but at high pressure it also acts as a nucleation inhibitor. Dimethylamine (DMA) is a stronger growth inhibitor than ammonia, and it also works well to smoothen cobalt deposition.

For other CVD systems, the challenge is to identify additives that promote nucleation and others that inhibit the film growth rate. The growth inhibitor must satisfy certain criteria, as we discussed in the previous section. Also, the growth inhibitor should not compromise the nucleation enhancement obtained by pretreatment of the surface.

3.5 Table and Figures

Table 3.1. Summary of all process conditions and morphologies of corresponding samples.

Pretreat-ment	Ammonia pressure (mTorr)	Deposition time (min)	Film thickness (nm)	rms roughness (nm)	Nuclei density (10^{11} cm^{-2})	Average nucleation rate (10^{11} $cm^{-2}\cdot min^{-1}$)
No	0	3	1.3	2.0	3	1
Yes	0	3	1.1	1.0	10	3.3
No	0.1	9	1.4	0.9	8	0.9
No	0.5	20	0.5	0.9	6	0.3
No	4	40	0.3	1.5	0.8	0.02
Yes	0.1	5	1.5	0.6	>11	>2.2
Yes	4	10	1.6	0.3	continuous	continuous

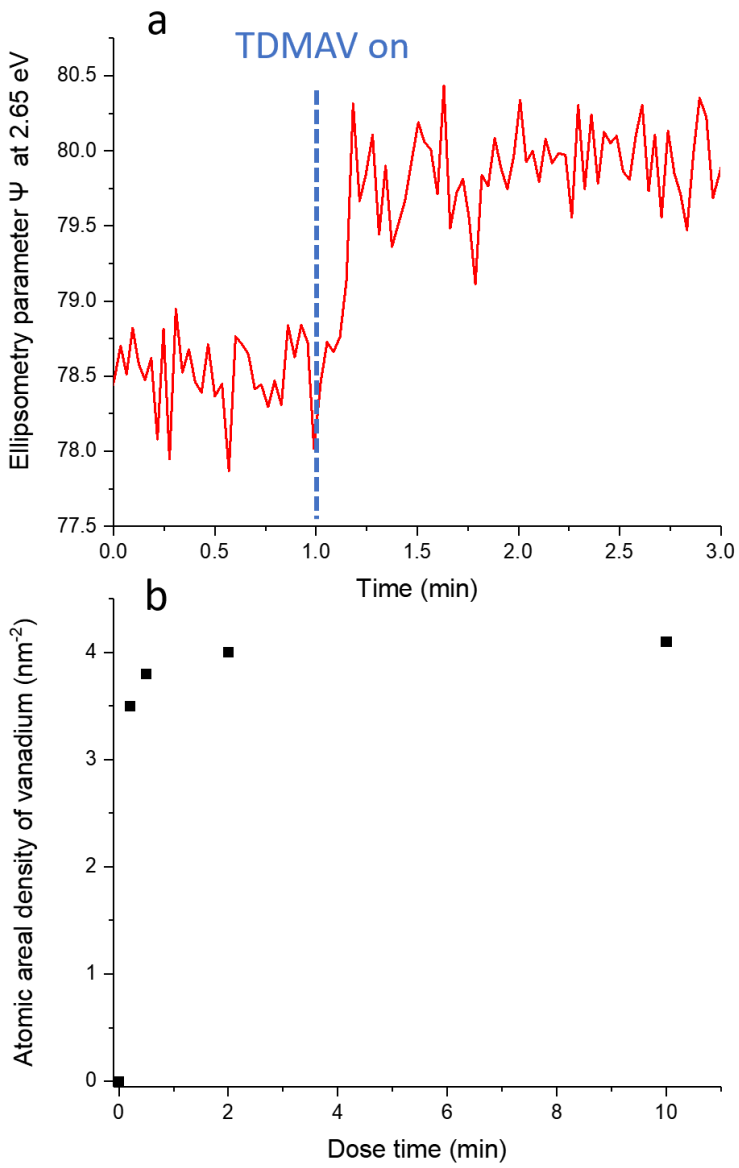

Figure 3.1. a) In situ ellipsometry parameter Ψ, at a photon energy of 2.65 eV, vs. time for adsorption of TDMAV at 70 °C on SiO_2. b) atomic areal density of vanadium on SiO_2 vs. TDMAV dose time. The zero point is obtained by measuring a bare SiO_2 without exposure to TDMAV molecules.

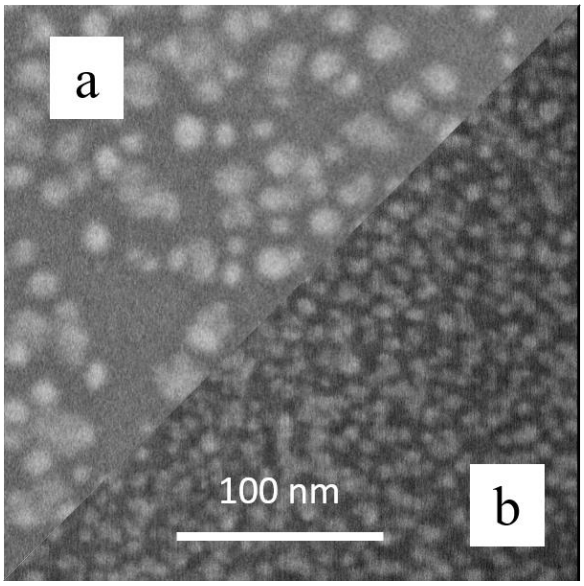

Figure 3.2. SEM images of cobalt nuclei deposited from $Co_2(CO)_8$ at 70 °C and pressure of 0.025 mTorr on SiO_2 a) without pretreatment b) with pretreatment by TDMAV.

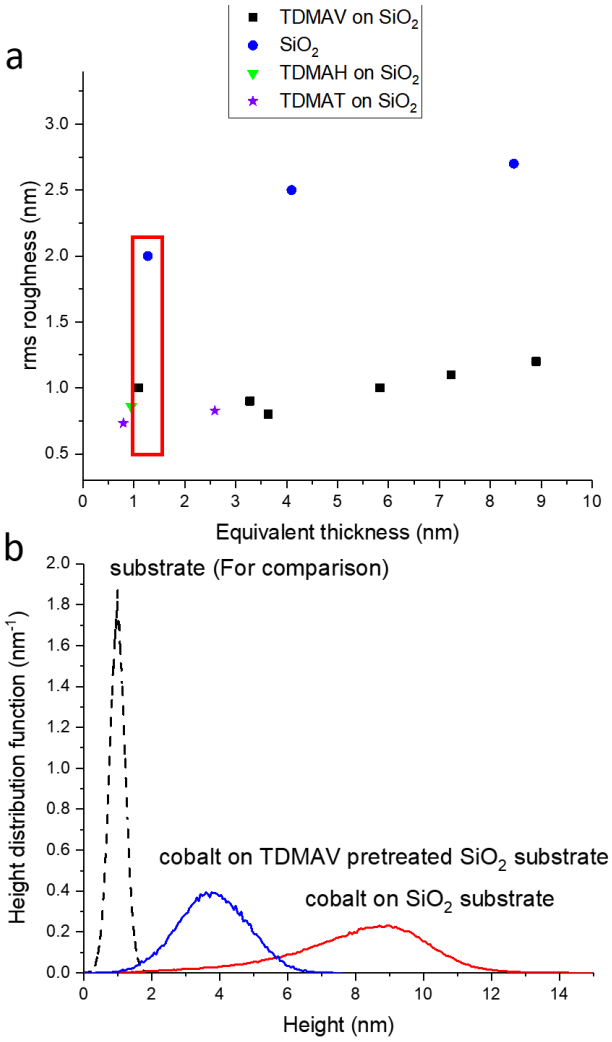

Figure 3.3. a) Surface roughness of cobalt films on SiO_2 with different pretreatment molecules. b) Height distribution functions of two samples with similar thickness (samples in red square in a). The thickness is 1.1 nm and 1.3 nm for blue and red line, respectively. The black dashed line is the height distribution function of bare SiO_2 for comparison.

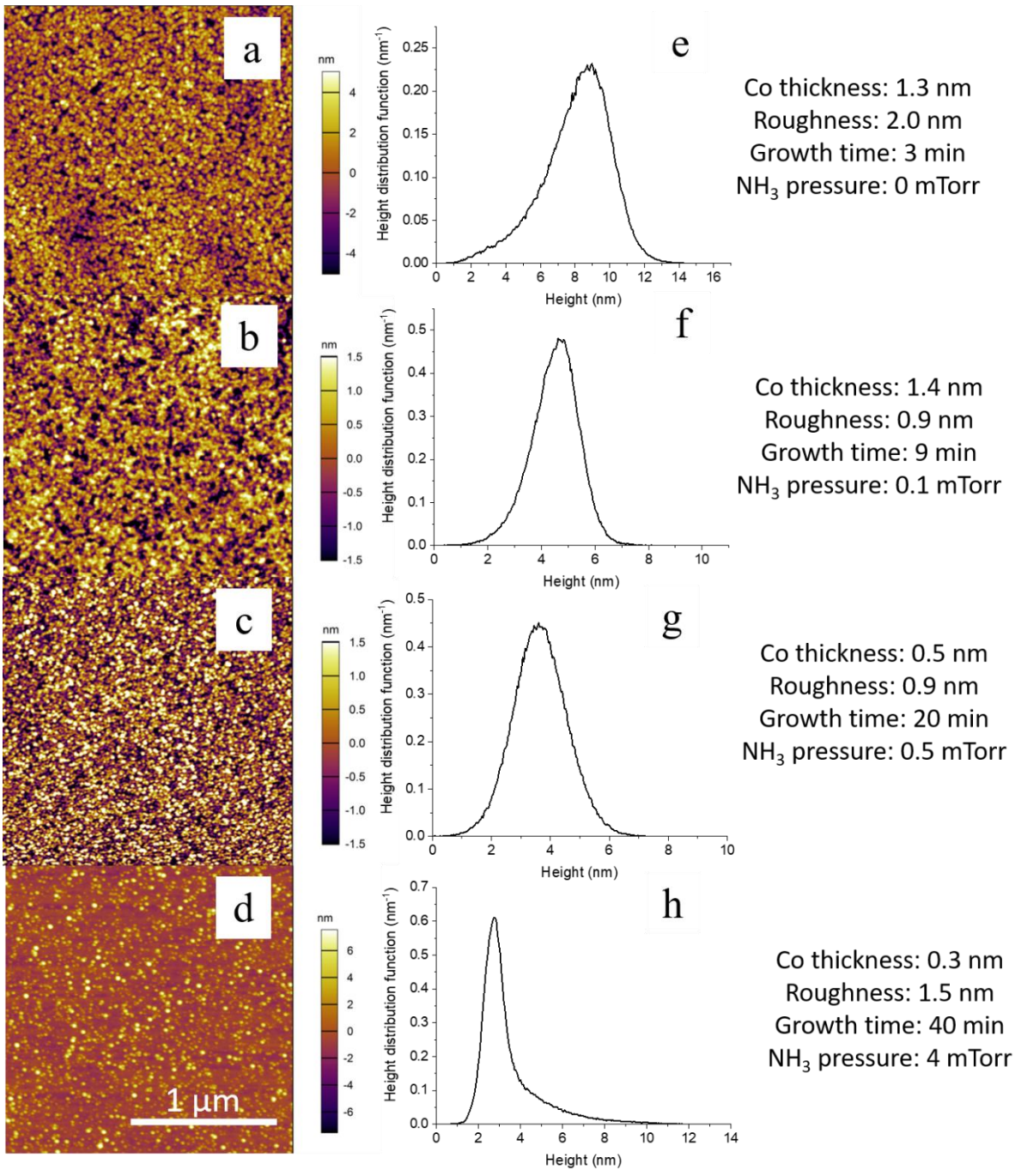

Figure 3.4. AFM images and corresponding height distribution functions for cobalt films on SiO_2 deposited with ammonia of different pressures. The substrate temperature is 70 °C and precursor pressure is 0.025 mTorr.

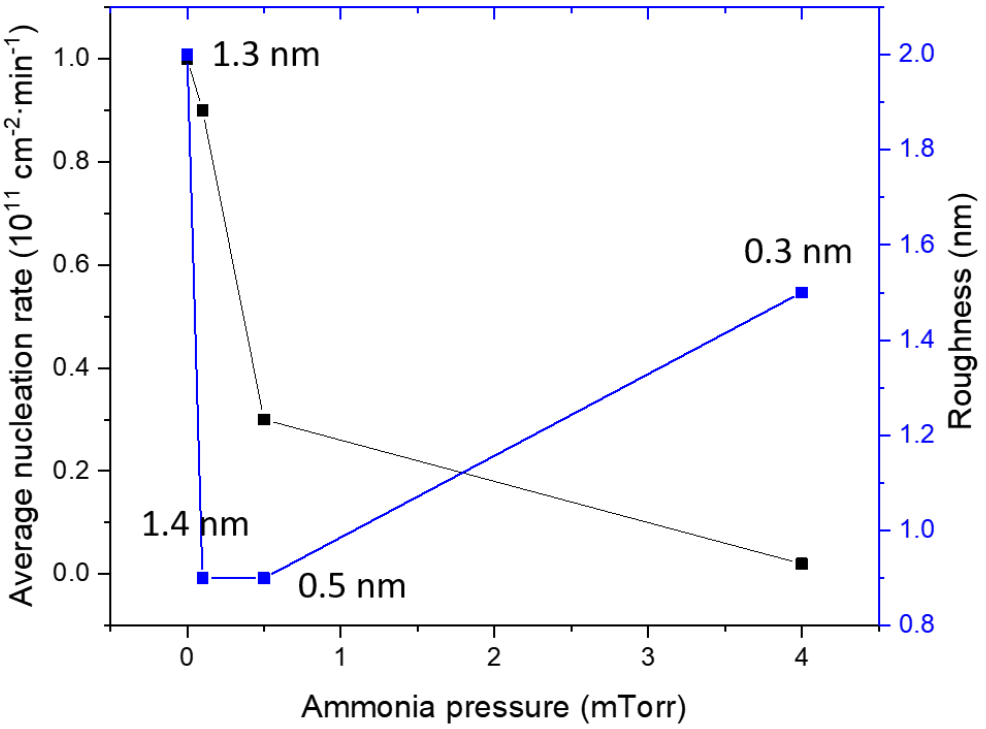

Figure 3.5. Relation of average nucleation rates and film roughnesses to ammonia pressure. Numbers that attached to each point are film thicknesses. Notice films grown with ammonia pressure of 0.5 mTorr and 4 mTorr are thinner. They presumably have a higher roughness if thicknesses are close to comparable to 1.3 or 1.4 nm.

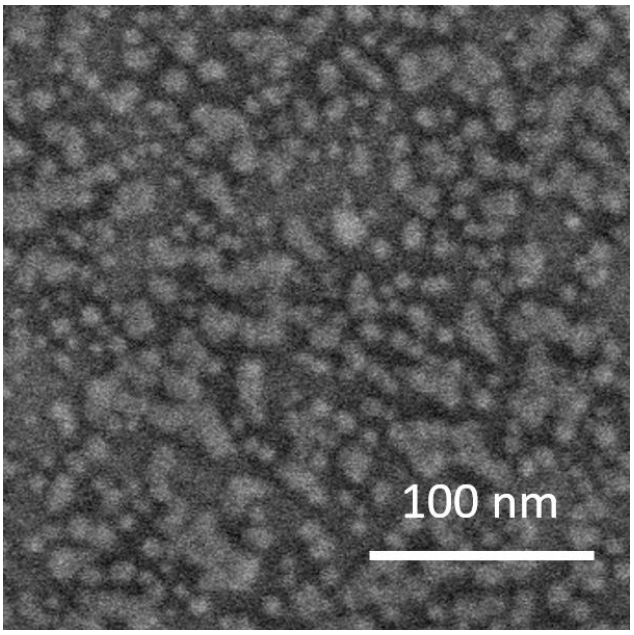

Figure 3.6. a) SEM images of cobalt nuclei deposited from $Co_2(CO)_8$ in the presence of 0.1 mTorr ammonia.

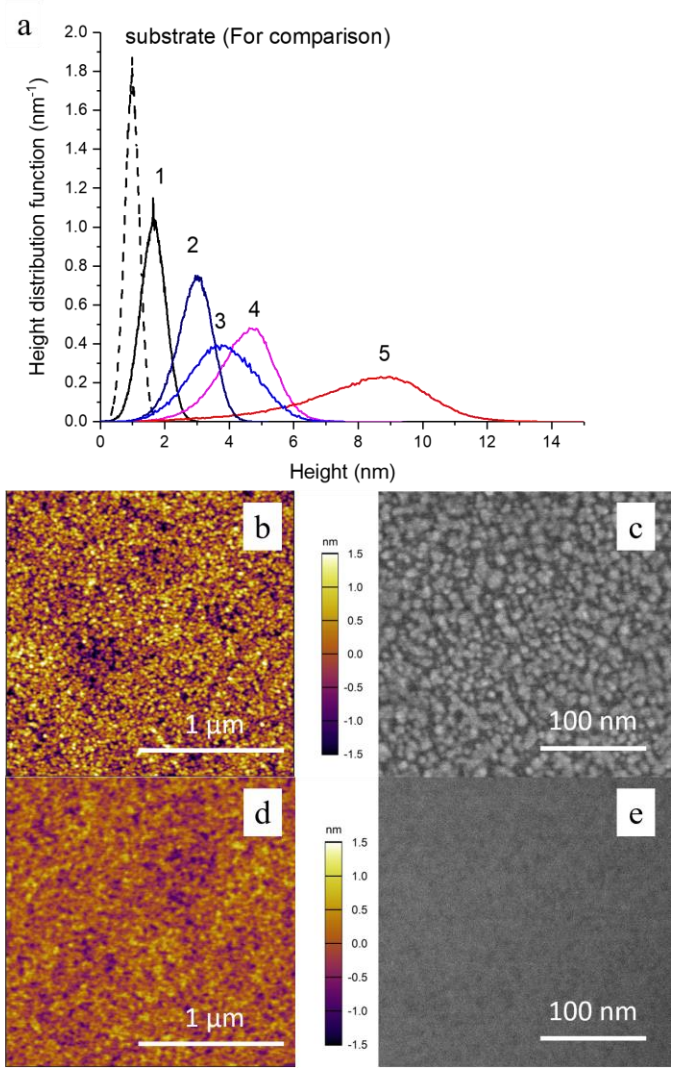

Figure 3.7. a) Height distribution functions of cobalt thin films of similar thicknesses deposited in different process conditions. The sample in black line (1) is deposited by $Co_2(CO)_8$ and 4 mTorr ammonia on TDMAV pretreated SiO_2. The thickness is 1.6 nm and roughness is 0.3 nm. The sample in dark blue line (2) is deposited by $Co_2(CO)_8$ and 0.1 mTorr ammonia on TDMAV pretreated SiO_2. The thickness is 1.5 nm and roughness is 0.6 nm. Samples prepared by processes in previous sections are included for comparison: (3) precursor only on TDMAV pretreated SiO_2 (the thickness is 1.5 nm and roughness is 0.6 nm); (4) precursor and 0.1 mTorr ammonia on bare SiO_2 (the thickness is 1.4 nm and roughness is 0.9 nm); (5) precursor only on bare SiO_2 (the thickness is 1.3 nm and roughness is 2.0 nm). Bare SiO_2 is shown for comparison. b) AFM image of the sample in a2. c) SEM image of the sample in a2. d) AFM image of the sample in a1. e) SEM image of the sample in a1 (The image may appear to be out of focus, but that is only because the sample is smooth and almost featureless).

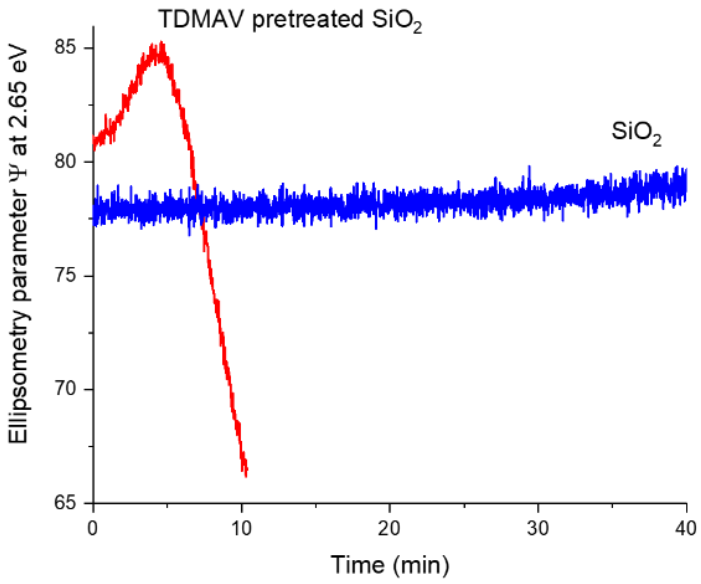

Figure 3.8. In situ ellipsometry parameter Ψ, at a photon energy of 2.65 eV, vs. time for cobalt film deposition from 0.018 mTorr $Co_2(CO)_8$ and 4 mTorr ammonia at 70 °C on bare SiO_2 and TDMAV pretreated SiO_2.

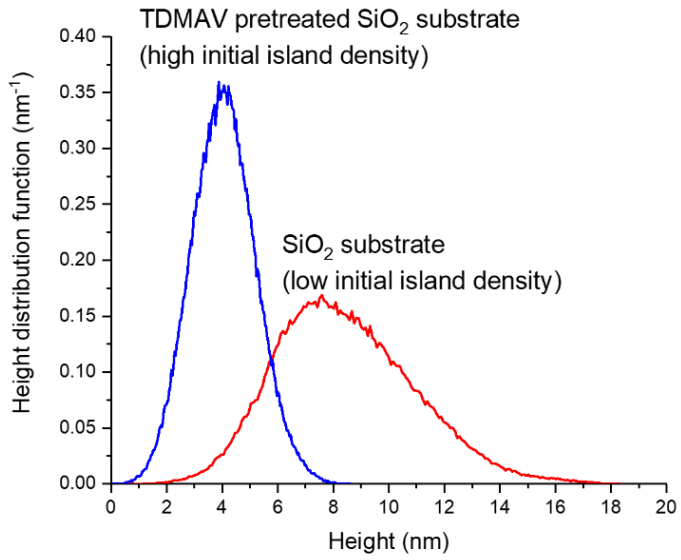

Figure 3.9. Diffusion-reaction calculation of the TDMA-Hf precursor pressure as a function of depth in a rectangular trench (θ = 0°) and a V-shaped trench with θ = 2° (nominal aspect ratio = 14). A substrate temperature of 200 °C is considered in the calculation.

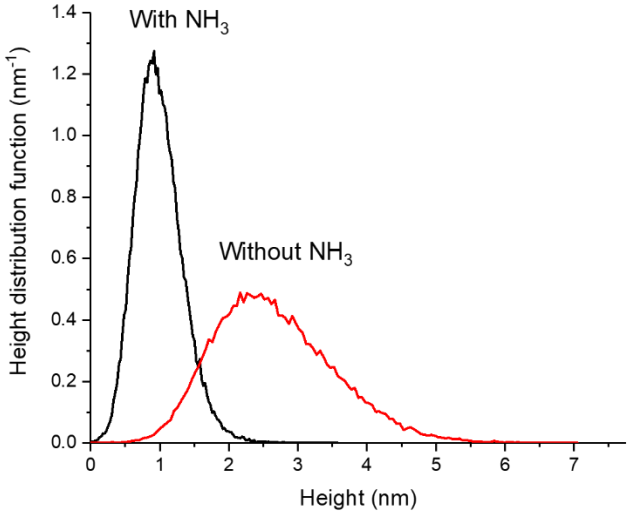

Figure 3.10. Height distribution functions of cobalt films deposited on a dense nucleation layer with and without ammonia co-flow. The dense nucleation layer, ~ 1.5 nm thick, is prepared by deposition from $Co_2(CO)_8$ in the presence of ammonia on TDMAV pretreated SiO_2. The total film thickness is 3.4 and 4.9 nm, respectively.

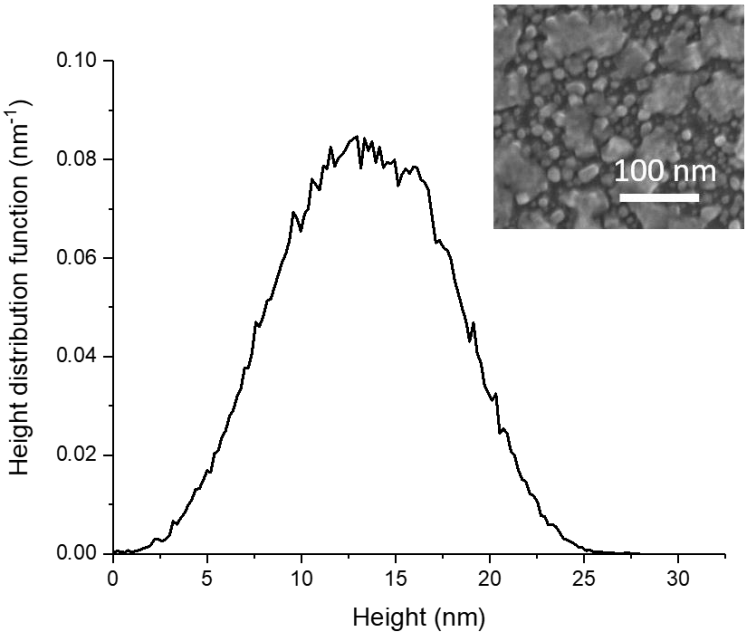

Figure 3.11. Height distribution of a cobalt film deposited on sparse nucleation layer, with 4 mTorr ammonia. The sparse nucleation layer is prepared by deposition from $Co_2(CO)_8$ only on SiO_2 to a thickness of ~ 1.5 nm. The total thickness is 8.6 nm.

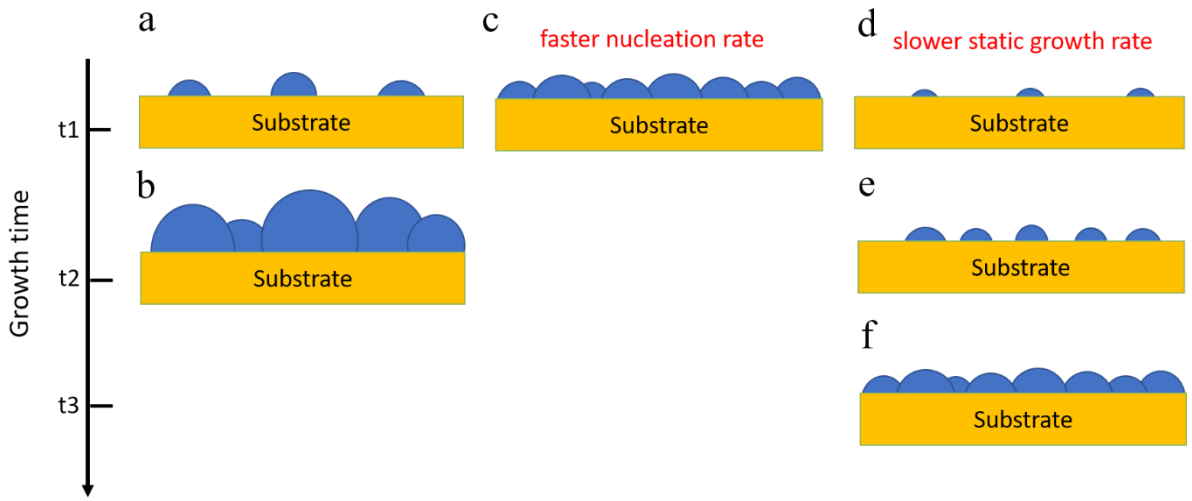

Figure 3.12. Schematic of nuclei formation, growth and coalescence on substrate. See text for details (a-f).

3.6 References

1. S. Babar, N. Kumar, P. Zhang, and J. R. Abelson, "Growth inhibitor to homogenize nucleation and obtain smooth hfb_2 thin films by chemical vapor deposition," *Chemistry of Materials* **25,** 662-7 (2013).

2. A. E. Kaloyeros, Y. Pan, J. Goff, and B. Arkles, "Editors' choice—review—cobalt thin films: Trends in processing technologies and emerging applications," *ECS Journal of Solid State Science and Technology* **8,** P119-P52 (2019).

3. Z. V. Zhang, S. Liu, G. S. Girolami, and J. R. Abelson, "Area-selective chemical vapor deposition of cobalt from dicobalt octacarbonyl: Enhancement of dielectric-dielectric selectivity by adding a coflow of nh3," *Journal of Vacuum Science & Technology A* **38,** 033401 (2020).

4. A. Yanguas-Gil, B. A. Sperling, and J. R. Abelson, "Theory of light scattering from self-affine surfaces: Relationship between surface morphology and effective medium roughness," *Physical Review B* **84,** 085402 (2011).

5. B. A. Sperling and J. R. Abelson, "Simultaneous short-range smoothening and global roughening during growth of hydrogenated amorphous silicon films," *Applied Physics Letters* **85,** 3456-8 (2004).

6. S. Hassani, K. Raeissi, and M. A. Golozar, "Effects of saccharin on the electrodeposition of ni–co nanocrystalline coatings," *Journal of Applied Electrochemistry* **38,** 689-94 (2008).

7. M. Bhardwaj, K. Balani, R. Balasubramaniam, S. Pandey, and A. Agarwal, "Effect of current density and grain refining agents on pulsed electrodeposition of nanocrystalline nickel," *Surface Engineering* **27,** 642-8 (2011).

8. F. A. Crossley and L. F. Mondolfo, "Mechanism of grain refinement in aluminum alloys," *Jom* **3,** 1143-8 (2017).

9. Y. Hwang, B. M. Nguyen, and S. A. Dayeh, "Atomic layer deposition of platinum with enhanced nucleation and coalescence by trimethylaluminum pre-pulsing," *Applied Physics Letters* **103,** 263115 (2013).

10. B. N. Zope and A. V. Gelatos, "Surface treatment to improve cctba based cvd co nucleation on dielectric substrate," United States US 9,218,980 B2

11. H. Han, J. J. Kim, and D. Y. Yoon, "Pretreatment technique for surface improvement of ru films in ru-metalorganic chemical vapor deposition," *Journal of Vacuum Science & Technology A: Vacuum, Surfaces, and Films* **22,** 1120-3 (2004).

12. N. Kumar, A. Yanguas-Gil, S. R. Daly, G. S. Girolami, and J. R. Abelson, "Remote plasma treatment of si surfaces: Enhanced nucleation in low-temperature chemical vapor deposition," *Applied Physics Letters* **95,** 144107 (2009).

13. J. Lim, H. Park, and C. Lee, "Enhancement of ru nucleation by pretreatments of the underlying tasin film surface in ru mocvd," *Thin Solid Films* **475,** 194-7 (2005).

14. K. S. Choi, J. M. Lim, S. Roy, and C. M. Lee, "Enhancement of ru nucleation in ru-metal organic chemical vapor deposition by electron cyclotron resonance plasma pretreatment," *Jpn J Appl Phys 1* **42,** 5539-42 (2003).

15. S. Babar, L. M. Davis, P. Y. Zhang, E. Mohimi, G. S. Girolami, and J. R. Abelson, "Chemical vapor deposition of copper: Use of a molecular inhibitor to afford uniform nanoislands or smooth films," *Ecs Journal of Solid State Science and Technology* **3,** Q79-Q83 (2014).

16. J. J. Kim, M. S. Kim, and D. Y. Yoon, "Effects of an added iodine source (c2h5i) on ru metal–organic chemical vapor deposition," *Chemical Vapor Deposition* **9,** 105-9 (2003).

17. J. J. Kim, D. H. Jung, M. S. Kim, S. H. Kim, and D. Y. Yoon, "Surface roughness reducing effect of iodine sources (ch3i, c2h5i) on ru and ruo2 composite films grown by mocvd," *Thin Solid Films* **409,** 28-32 (2002).

18. K. M. Thom and J. G. Ekerdt, "The effect of an iodine source on nucleation and film properties of ru films deposited by chemical vapor deposition," *Thin Solid Films* **518,** 36-42 (2009).

19. W. Liao and J. G. Ekerdt, "Effect of co on ru nucleation and ultra-smooth thin film growth by chemical vapor deposition at low temperature," *Chemistry of Materials* **25,** 1793-9 (2013).

20. G. Ruhl, B. Froschle, P. Ramm, A. Intemann, and W. Pamler, "Deposition of titanium nitride/tungsten layers for application in vertically integrated-circuits technology," *Applied Surface Science* **91,** 382-7 (1995).

21. M. H. van der Veen, K. Vandersmissen, D. Dictus, S. Demuynck, R. Liu, X. Bin, P. Nalla, A. Lesniewska, L. Hall, K. Croes, L. Zhao, J. Bommels, A. Kolics, Z. Tokei, and Ieee, "Cobalt bottom-up contact and via prefill enabling advanced logic and dram technologies," *2015 IEEE International Interconnect Technology Conference and 2015 IEEE Materials for Advanced Metallization Conference***,** 25-7 (2015).

22. S.-Q. Wang, "Barriers against copper diffusion into silicon and drift through silicon dioxide," *MRS Bulletin* **19,** 30-40 (2013).

23. N. Samal, K. B. Chetry, K. Rook, A. Hayes, and A. Devasahayam, "Low-temperature (≤150 °c) chemical vapor deposition of pure cobalt thin films," *Journal of Vacuum Science & Technology B, Nanotechnology and Microelectronics: Materials, Processing, Measurement, and Phenomena* **32,** 011206 (2014).

24. T. Shinzawa, K. Sugai, Y. Hayashi, T. Nakajima, S. Kishida, H. Okabayashi, K. Tsunenari, Y. Murao, A. Kobayashi, and T. Yako, "Barrier layerless submicron aluminum-damascene interconnection using aluminum chemical vapor deposition with a

new nucleation method," *Electronics and Communications in Japan (Part II: Electronics)* **79,** 88-96 (1996).

25. S. Jayaraman, Y. Yang, D. Y. Kim, G. S. Girolami, and J. R. Abelson, "Hafnium diboride thin films by chemical vapor deposition from a single source precursor," *Journal of Vacuum Science & Technology A* **23,** 1619-25 (2005).

26. S. Jayaraman, E. J. Klein, Y. Yang, D. Y. Kim, G. S. Girolami, and J. R. Abelson, "Chromium diboride thin films by low temperature chemical vapor deposition," *Journal of Vacuum Science & Technology A* **23,** 631-3 (2005).

27. X. Wang, Z. Guo, Y. Gao, and J. Wang, "Atomic layer deposition of vanadium oxide thin films from tetrakis(dimethylamino)vanadium precursor," *Journal of Materials Research* **32,** 37-44 (2016).

28. Q. Xie, Y.-L. Jiang, C. Detavernier, D. Deduytsche, R. L. Van Meirhaeghe, G.-P. Ru, B.-Z. Li, and X.-P. Qu, "Atomic layer deposition of tio2 from tetrakis-dimethyl-amido titanium or ti isopropoxide precursors and h2o," *Journal of Applied Physics* **102,** 083521 (2007).

29. J. W. Elam, D. A. Baker, A. J. Hryn, A. B. F. Martinson, M. J. Pellin, and J. T. Hupp, "Atomic layer deposition of tin oxide films using tetrakis(dimethylamino) tin," *Journal of Vacuum Science & Technology A* **26,** 244-52 (2008).

30. E. Mohimi, Z. V. Zhang, J. L. Mallek, S. Liu, B. B. Trinh, P. P. Shetty, G. S. Girolami, and J. R. Abelson, "Low temperature chemical vapor deposition of superconducting vanadium nitride thin films," *Journal of Vacuum Science & Technology A* **37,** 031509 (2019).

31. X. Liu, S. Ramanathan, and T. E. Seidel, "Atomic layer deposition of hafnium oxide thin films from tetrakis(dimethylamino)hafnium (tdmah) and ozone," *MRS Proceedings* **765,** D3.8 (2011).

32. A. Yanguas-Gil, "Reactivity of heterogeneous surfaces: Modeling precursor–surface interaction using absorbing markov chains," *Journal of Vacuum Science & Technology A* **36,** 051510 (2018).

33. E. Mohimi, Z. V. Zhang, S. M. Liu, J. L. Mallek, G. S. Girolami, and J. R. Abelson, "Area selective cvd of metallic films from molybdenum, iron, and ruthenium carbonyl precursors: Use of ammonia to inhibit nucleation on oxide surfaces," *Journal of Vacuum Science & Technology A* **36,** 041507 (2018).

34. S. Babar, T. T. Li, and J. R. Abelson, "Role of nucleation layer morphology in determining the statistical roughness of cvd-grown thin films," *Journal of Vacuum Science & Technology A* **32,** 060601 (2014).

35. T. Karabacak, "Thin-film growth dynamics with shadowing and re-emission effects," *Journal of Nanophotonics* **5,** 052501 (2011).

36. G. S. Bales and A. Zangwill, "Macroscopic model for columnar growth of amorphous films by sputter deposition," *Journal of Vacuum Science & Technology A* **9,** 145-9 (1991).

37. J. A. Venables and G. D. T. Spiller, "Nucleation and growth of thin films," in *Surface mobilities on solid materials: Fundamental concepts and applications*, edited by V. T. Binh (Springer US, Boston, MA, 1983), p. 341-404. [DOI: 10.1007/978-1-4684-4343-1_16]

38. J. Soethoudt, F. Grillo, E. A. Marques, J. R. van Ommen, Y. Tomczak, L. Nyns, S. Van Elshocht, and A. Delabie, "Diffusion-mediated growth and size-dependent nanoparticle reactivity during ruthenium atomic layer deposition on dielectric substrates," *Advanced Materials Interfaces* **5,** 1800870 (2018).

39. P. Zhang, X. Zheng, S. Wu, and D. He, "A computer simulation of nucleation and growth of thin films," *Computational Materials Science* **30,** 331-6 (2004).

CHAPTER 4

CVD OF HAFNIUM DIBORIDE FROM HAFNIUM BOROHYDRIDE: AREA SELECTIVE DEPOSITION OF ALUMINUM OXIDE AGAINST SILICON OXIDE AND EFFECT OF PRETREATMENT BY $Hf[(CH_3)_2N]_4$ ON NUCLEATION

4.1 Introduction

Chemical vapor deposition (CVD) and atomic vapor deposition (ALD) are powerful techniques on depositing metallic films, such as metals [1-3] and borides [4]. However, they sometimes suffer nucleation issues, especially metal deposition on oxide.

We can take the advantage of such substrate-dependent issues to achieve area selective deposition (ASD). ASD builds upon the previously established pattern on the substrate and obviates the need for additional patterning and etching steps, gaining great interests in semiconductor industry [5]. Previously, we studies the nucleation of MoC_x and Co from $Mo(CO)_6$ [2] and $Co_2(CO)_8$ [3], respectively, on various substrates. We discovered that nucleation is substrate dependent, where it is selective on metallic substrates against dielectrics. Meanwhile, nucleation also varies on different dielectrics. For example, cobalt preferentially grow on Al_2O_3 rather than SiO_2 from $Co_2(CO)_8$ [3], and thus, area selective deposition of cobalt on Al_2O_3 against SiO_2 is obtained. We attribute such differential to the different acidity or basicity of oxides. In ASD processes, selectivity is not perfect as nucleation also commences on the intended nongrowth surface, usually as islands at a lower density. Initial nucleation and growth cannot be detected by spectroscopic ellipsometry (SE), until enough film atoms are on the surface. The time that SE does not respond to growth is usually termed as nucleation delay or incubation time.

If film growth on nongrowth surface is required (such as Co on SiO_2), however, sparse nucleation occurs. Eventually the islands coalesce after long growth time, meaning that it is difficult to make continuous films that are also very thin; instead, at the point of full coalescence

the films are typically thick and rough. Kinetically, we discussed in chapter 3 that the development of initial roughness can be described in terms of the area density of possible nucleation sites, the time dependence of film nucleation (nucleation probability on each site), and the rate of film growth on those nuclei. The first two terms determine the nucleation rate. And smooth films result when the precursor has a high probability of reaction with the substrate surface, or a relatively low probability of reacting with the surface of the deposited material. And thus, Nucleation issue on undesired surface could be mitigated by surface pretreatment [6-11], nucleation layer to increase the rate of nucleation [12,13] or coflow of a growth inhibitor [11,14-19]to reduce rate of growth. Among these methods, the method of surface pretreatment does not consume part of the width of vias and trenches, which increases the electrical resistance of the interconnect, compared with nucleation layer, and does not introduce contaminations into the films, compared with growth inhibitors. In some cases, when the pretreatment is self-limiting, it would work well for recessed structures due to good conformality. TDMAM (M=Ti, V, Hf) molecules have been reported [7] and in chapter 3 as potential candidates for this purpose.

This work is divided into two parts. First, we demonstrate an inherent ASD of HfB_2 from $Hf(BH_4)_4$ on Al_2O_3 against SiO_2, similar to chapter 2. We report film thickness to growth time on Al_2O_3 and SiO_2. We study nucleation by AFM from on SiO_2 to show the selectivity is not perfect and nucleation occurs readily on SiO_2, at a much lower density. Comparison of AFM and ellipsometry data indicates ellipsometry is not as sensitive to monitor the onset of nucleation. Unfortunately, coflow of ammonia does not work here to improve selectivity and will halt the growth completed at very low pressure [14]. Second, we apply surface pretreatment from self-limiting tetrakis(dimethylamino)hafnium (TDMAH) to increase nuclei density of HfB_2 and reduce roughness on SiO_2. Interestingly, surface pretreatment increases film roughness slightly on Al_2O_3.

4.2 Experimental

CVD experiments are performed in a cold wall high vacuum chamber of high vacuum construction described elsewhere; the base pressure is $1x10^{-7}$ Torr, most of which is H_2 [20,21]. The precursor $Hf(BH_4)_4$ is synthesized in the lab. The precursor is maintained in a glass container immersed in a water bath and delivered to the chamber without a carrier gas through a

0.4 cm i.d. stainless steel tube aimed at the substrate to sustain a chamber pressure of 0.05 mTorr. The forward-directed gas stream produces a higher flux at the substrate surface than indicated by the background chamber pressure. The pressure in the chamber background is measured by MKS Baratron® capacitance manometer (390HA-00001). TDMAH are supplied by Sigma-Aldrich and used as received. They are maintained in separate metal containers and supplied at room temperature without carrier gas. The pressure of such molecules in the chamber is below 10^{-6} Torr. Substrates are radiatively heated to 220 °C, as measured by a K-type thermocouple attached to the front of the sample holder. Temperature-dependent selectivity and nucleation is not the subject of the work. However, at high temperate (such as 250 °C), deposition is too fast so the window to differentiate the growth on SiO_2 and Al_2O_3 is small. At low temperature (such as 200 °C), deposition is very slow so the total growth time is long and lots of $Hf(BH_4)_4$ molecules are wasted due to low reactivity. For the samples with the pre-treatment step, the SiO_2 surface is exposed to TDMAH for 2 min, at a temperature of 220 °C. HfB_2 deposition is performed 8 min after the pre-treatment, to avoid the effect of residual TDMAH molecules that desorb from the room temperature chamber walls.

Microelectronic grade Si wafers with 300 nm thermal SiO_2 or 10 nm Al_2O_3 (by atomic layer deposition from trimethylaluminum and water at 80 °C) are used and degreased by washing successively with acetone, IPA, and deionized water, and then are cleaned by UV ozone treatment for 10 min before the substrates are loaded into the chamber.

Real-time spectroscopic ellipsometry (SE) is used to monitor HfB_2 deposition. Data fitting is proceeded with Lorentz oscillator model [4] for thickness using CompleteEASE® software. The areal density of metal atoms is measured ex-situ by Rutherford backscattering spectroscopy; we report an equivalent film thickness by fitting areal atomic density of Hf atoms and converting it to film thickness using the bulk density of HfB_2 and assuming stoichiometry. For samples with pretreatment, TDMAH layer contains ~4.6×10^{14} /cm^2 (chapter 3) Hf atoms and need to be subtracted from total atomic density. Unless stated otherwise, all thicknesses are equivalent film thicknesses. Meanwhile, we will report thickness from SE for comparison. Film roughness is measured by atomic force microscope (Asylum cypher). Nuclei densities are obtained by counting islands manually from AFM images in a square of 500 nm × 500 nm for SiO_2 substrates and 250 nm × 250 nm for Al_2O_3 substrates. 4 counts have been done for each

sample to calculate the standard deviation. Note that tip convolution effects set a limit on the ability to resolve islands as separate when they are very close to each other.

4.3 Results and Discussion

4.3.1 ASD of HfB_2 on SiO_2 and Al_2O_3

SiO_2 and Al_2O_3 substrates are exposed to $Hf(BH_4)_4$ for various periods of time at 220 °C. The film thickness is monitored by in-situ SE and RBS (Fig. 4.1). Thickness measured by SE, however, equivalent thickness by RBS is 30%~40% less, indicating the films are less dense than bulk HfB_2 [22] or the film is boron rich. On Al_2O_3, HfB_2 deposition occurs in < 2 min from SE, which we term a short nucleation delay. The deposition rate increases as nucleation proceeds and then stabilizes at ~1.5 nm/min (from SE) or ~1 nm/min (from RBS) in approximately 5 min. A 10.4-nm film (from RBS) is grown on Al_2O_3 in 16 min. On SiO_2, nucleation delay is more than 15 min from SE and only 0.07 nm of HfB_2 is grown in 18 min. Thus, deposition of HfB_2 is inherently selective on Al_2O_3 against SiO_2.

Though SE curve is flat for the first 15 min, nucleation occurs already on SiO_2, i.e., selective deposition is not perfect. To demonstrate this, the sample with deposition time of 10 min are analyzed by AFM (Fig. 4.2) and RBS (Table 4.1). RBS reports a non-zero thickness of 0.015 nm, and from AFM image, there are quite a few nuclei ($110 \pm 35\ \mu m^{-2}$) on the surface with a maximum height of ~8 nm. These results indicate that SE is not as sensitive as RBS or AFM to monitor the nucleation process.

The nucleation on SiO_2 takes place in a dynamic way, not at the growth-onset only, because nuclei densities increase linearly to the deposition time (Fig. 4.3 and Table 4.1). Note that the nuclei density-deposition time curve crosses x-axis at ~6 min, however, it does not mean nuclei density is zero before 6 min of exposure to $Hf(BH_4)_4$. When islands are counted from AFM images, small islands with the height less than ~2 nm may be neglected because they are submerged in the fluctuation of initial substrate and cannot be detected. If these small islands could be counted, then the whole curve would shift upwards and may cross the x axis close to zero. In fact, nucleation seems to occur immediately, as we will cover in the next paragraph.

Dynamic nucleation is also supported by island height distribution (Fig. 4.4, a and b). Island height distributions are descending curves in this work, which is the sign of dynamic nucleation [23]. Otherwise, there will be a peak shifting to higher value as deposition proceeds.

Nucleation occurs readily when SiO_2 is exposed to $Hf(BH_4)_4$, evidenced by the linear relation between maximum height on the surface and growth time (Fig. 4.5). When island redistribution is not considered, which is the case for this work due to low deposition temperature (200 °C) compared with HfB_2 melting point (3250 °C), the maximum height on the surface is normally on the nucleus [24] that exists the longest (the very first nuclei on the surface). Note that there is a linear correlation between radius (as determined from projected area) and island height (Fig. 4.4, a and b), consistent with a conservation of the island shape with the size (the highest island is the largest island). Thus, it contains the information when nucleation occurs. The precaution is AFM can only tell the relative difference in height, and therefore, maximum height in AFM image equals to maximum height of islands only before coalescence to a continuous film. In this work, the maximum height of HfB_2 islands on SiO_2 increases linearly with deposition time and the intercept is close to 0 (Fig. 4.5), *indicating nuclei form immediately when SiO_2 is exposed to $Hf(BH_4)_4$*. On Al_2O_3 substrate, nucleation is fast, with ~4300 nuclei per μm^{-2} in 3.5 min (Table 4.1), and thus, nucleation occurs readily on both substrates. Note it is more difficult to study the evolution of maximum height the same way as that on SiO_2 because the surface reaches coalescence fast and then maximum height is relatively stable (Fig. 4.6). Growth occurs more quickly on metallic HfB_2 islands than oxide substrates, and thus, initial growth on Al_2O_3 is faster than SiO_2 due to higher nuclei density (selective deposition).

However, it appears the growth rate of islands on SiO_2 are slower, for an unknown reason, than that on Al_2O_3, because the highest islands on SiO_2 after 10 min deposition is ~8 nm (Fig. 4.5) while on Al_2O_3 the highest islands are ~8 nm (Fig.4.6) in 3.5 min. This result appears to allow a possible etching step to fix stray nucleation on SiO_2 to enhance selectivity [25-27], though process of atomic layer etching or gas phase etching has not been developed for HfB_2, as far as we know.

4.3.2 Film roughness on Al_2O_3 and SiO_2

Al_2O_3 is a more reactive surface for CVD of HfB_2, and it is also reflected in film roughness and nuclei density (or rate). For films of similar thicknesses, not only it requires much longer time (24.5 min on SiO_2 for a 0.39 nm film vs. 3.5 min on Al_2O_3 for a 0.59 nm film), the roughness on SiO_2 is higher at 3.8 nm while on Al_2O_3 it is only 1.30 nm (Table 4.1). Due to longer growth time and dynamic nucleation, islands on SiO_2 have a wider height distribution (Fig. 4.7). Some islands are exceeding 20nm. On Al_2O_3, the highest island is 8 nm.

In power spectral density (PSD) analysis, the amplitude at high spatial frequencies corresponds to short-range roughness on the surface, and the amplitude at low frequencies corresponds to long-range roughness. In Fig. 4.8, the PSD at high k is similar on Al_2O_3 and SiO_2, but the plateau at lower k on Al_2O_3 is an order of magnitude smaller than that on SiO_2. This is reasonable because local roughness is determined by local smoothening through diffusion of adatoms and precursors on nuclei and will not be affected by substrates.

As we explained in the introduction, initial roughness can be reduced with a higher nucleation rate and/or a lower rate of film growth on those nuclei. There is no evidence film growth on nuclei for Al_2O_3 surface is slower than SiO_2 (conversely, it seems to be faster as we described above). Nucleation rate is determined by area density of possible nucleation sites and nucleation probability on each site. Surface OH group is presumably the nucleation sites. On fully-hydroxylated SiO_2, the density of OH is ~4.6 nm^{-2} [28] and on Al_2O_3, the value is higher [29] at 9.3~14.5 nm^{-2}. However, the nuclei densities for samples described above are 4300±362 μm^{-2} on Al_2O_3 and 730±65 μm^{-2} on SiO_2. Taking growth time into consideration, the average nucleation rate on Al_2O_3 is 40 times higher (Table 4.1). The difference on the density of OH alone cannot explain the factor of 40. The major reason for a higher nucleation rate on Al_2O_3 is attributed to a higher nucleation probability.

Though the exact nature of higher nucleation probability on Al_2O_3 is not clear, it is likely related to the basicity of oxide surface and influenced by the rate of $Hf(BH_4)_4$ losing volatility on surface and the rate of chemically adsorbed $Hf(BH_4)_x$ species converting to nuclei. First, base is known to induce the decomposition of hafnium borohydride complexes to generate hafnium hydrides and borane-base adducts [30,31]. Because Al_2O_3 is more basic than SiO_2, similar

decomposition reactions would be easier to occur on alumina than silica and cause $Hf(BH_4)_4$ precursor to lose volatility. A monolayer of $Hf(BH_4)_4$ has ~10^{15} /cm^2 Hf atoms. However, for a SiO_2 surface that has been exposed to $Hf(BH_4)_4$ for 10 min, there are only 5×10^{13} /cm^2 atoms. Second, when $M(BH_4)_4$ (M=Zr and Hf) molecules are adsorbed on alumina and silica, the further decomposition of surface-bonded $M(BH_4)_x$ occurs at lower temperature on Al_2O_3 than on SiO_2. [32] The authors suggest that surface-bonded $M(BH_4)_x$ decomposes on Al_2O_3 by deprotonation of surface hydroxyl groups. [32] This cannot be a result of simple deprotonation reaction because SiO_2 is more acidic than Al_2O_3 [33]. It is likely that deprotonation of surface hydroxyl groups on Al_2O_3 is promoted by the local environment. Alternatively, the further decomposition of $M(BH_4)_x$ may also occur in a base promoted fashion as described above: [30,31] the basic sites on alumina promote the decomposition of borohydride to generate hafnium hydrides and borane-base adducts. The generated hafnium hydrides (which are likely more basic than borohydride because M–H bond is likely more ionic than B–H bond) then react with surface O–H groups. Notably, addition of base to hafnium borohydride complexes can also promote the formation of hafnium borohydride/hydride complexes with nuclearity, which is presumably an intermediate towards formation of nuclei.

4.3.3 Effect of TDMAH on HfB_2 nucleation

When HfB_2 growth on SiO_2 is needed, sparse nucleation and long growth time before coalescence makes it difficult to grow a continuous thin film and the surface is rough. Here, we introduce a surface pretreatment of TDMAH on SiO_2 to mitigate the problem. As an ALD precursor, adsorption of TDMAH is a self-limiting process (Fig. 9), resulting surface-bound $M(DMA)_x(O\text{-}Si\equiv)$ intermediate. HfB_2 growth on top of the intermediate is faster: a film of similar thickness (0.42 nm) is deposited in only 16.5 min. This is 8 min shorter than the sample grown on a non-treated SiO_2 surface in otherwise identical conditions. The sample has a higher nuclei density (Fig. 4.10 and Table 4.1) at ~2580 ± 82 μm^{-2}, compared with 733 ± 65 μm^{-2}, leading a much smaller roughness of 1.7 nm (3.8 nm without pretreatment). In PSD, only long-range roughness is reduced while short-range roughness remains unchanged (Fig. 4.8). Thus, pretreatment by TDMAH enhances nucleation and reduces roughness for CVD of HfB_2 from $Hf(BH_4)_4$ on SiO_2. However, growth on such surface is still not as good as Al_2O_3 surface.

Surprisingly, pretreatment on Al_2O_3 makes the nucleation slightly worse. It takes slightly longer (8.3 min vs. 7.3 min) to grow a film of similar thickness (1.9 nm) and the film is rougher (1.7 vs. 1.4 nm) (Table 4.1 and Fig. 4.11). *SiO_2 and Al_2O_3 after TDMAH pretreatment are more similar than before, though nucleation is still worse on SiO_2, indicating the effect of substrates still exists.*

4.4 Conclusion

We investigate nucleation of HfB_2 on SiO_2, Al_2O_3, TDMAH pretreated SiO_2 and Al_2O_3 from $Hf(BH_4)_4$ at 220 °C. Area selective deposition of HfB_2 on Al_2O_3 against SiO_2 is demonstrated. Interestingly, nucleation occurs readily on both SiO_2 and Al_2O_3 but nuclei density on Al_2O_3 is much higher. Islands on Al_2O_3 appear to grow faster: the highest island on Al_2O_3 is ~8 nm in 3.5 min while on SiO_2 it takes 10 min to reach a similar value. Higher nuclei density also leads to a smoother film on Al_2O_3: at a thickness of ~0.5 nm, the rms roughness on Al_2O_3 is about 1.3 nm while on SiO_2 it is 3.8 nm. The different nucleation rates on SiO_2 and Al_2O_3 may relate to the different basicity of hydroxyl groups on different oxide surfaces.

Pretreatment by TDMAH on SiO_2 can enhance nucleation. It increases nuclei density by 5 times and reduces film roughness (rms roughness is 1.7 nm for a film of ~0.4 nm). However, such pretreatment slightly increases film roughness and growth time on Al_2O_3.

4.5 Table and Figures

Table 4.1. HfB_2 deposition on SiO_2, Al_2O_3, SiO_2 with TDMAH pretreatment and Al_2O_3 with TDMAH pretreatment. Note that rms roughness is very low for SiO_2 substrate with 10-min growth time (second sample in the table) and it is simply because most of the surface is still not covered by nuclei and thus substrate roughness is dominant.

Substrate	Deposition time (min)	Equivalent Thickness (nm)	Rms roughness (nm)	Nuclei density (μm^{-2})	Average nucleation rate ($\mu m^{-2} \cdot min^{-1}$)
Al_2O_3	3.5	0.59	1.3	4304±362	1230
SiO_2	10	0.015	0.3	112±35	11
SiO_2	18	0.07	1.7	524±35	29
SiO_2	24.5	0.39	3.8	733±65	30
SiO_2	34	5.8	4.6	1020±57	30
SiO_2 with TDMAH pretreatment	16.5	0.42	1.7	2578 ± 82	156
Al_2O_3	7.3	1.9	1.4	Continuous films	
Al_2O_3	16	10.4	1.1		
Al_2O_3 with TDMAH pretreatment	8.3	1.9	1.7		

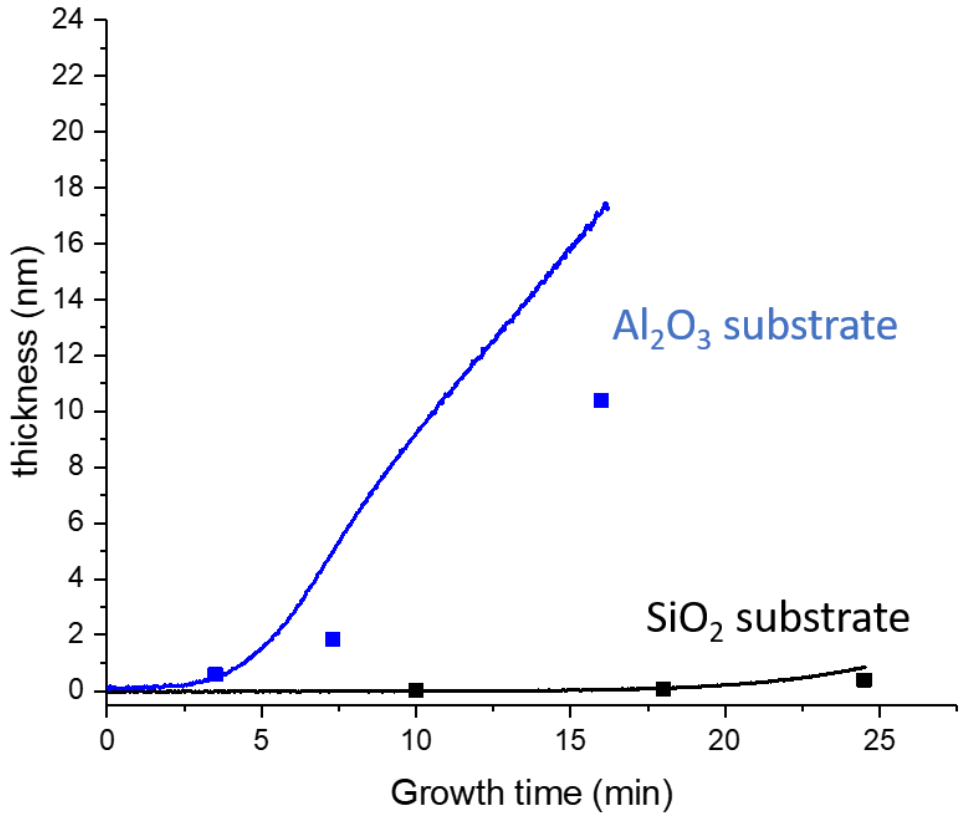

Figure 4.1. Curves of HfB_2 film thickness vs. deposition time. Film thickness is measured by three different techniques: RBS (dots) and SE (lines).

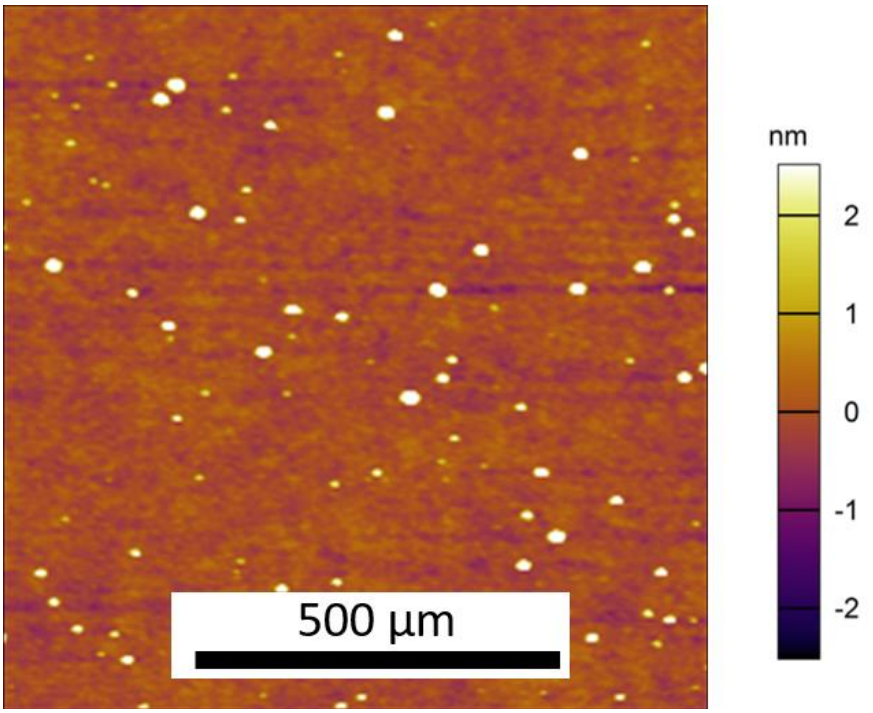

Figure 4.2. AFM images of HfB_2 films on SiO_2 after 10 min.

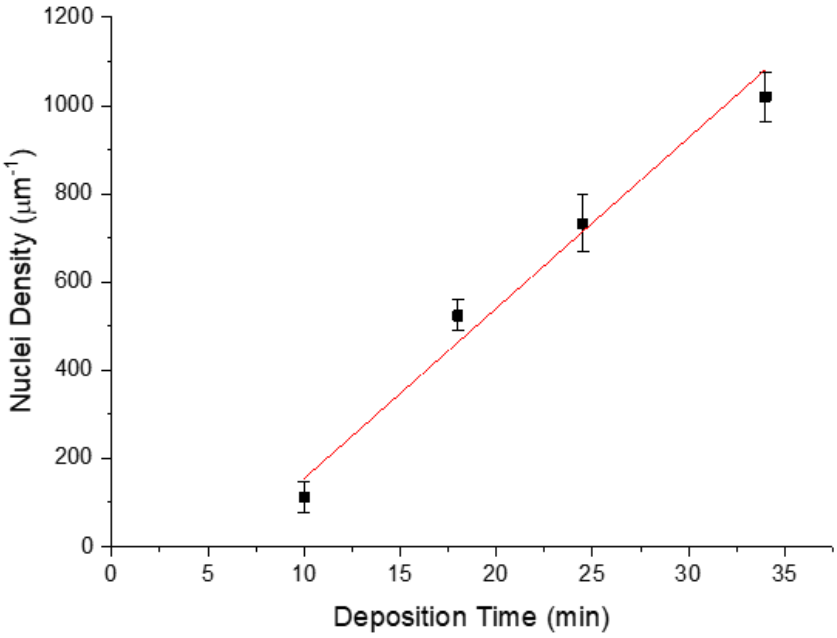

Figure 4.3. Nucleation density vs. deposition time. The red line is linear fit, with a slope of 38.(6) and intercept of -232.

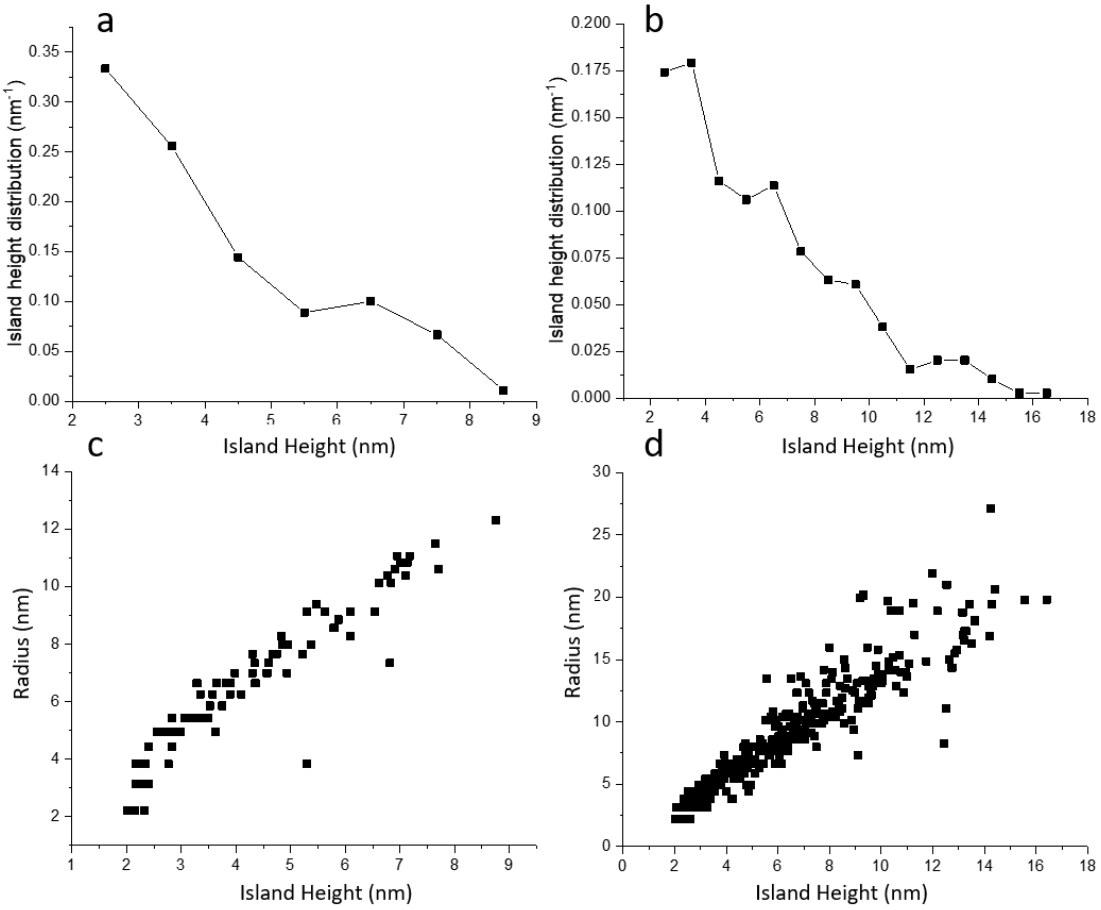

Figure 4.4. Island height distribution and nuclei radius - height correlation for HfB_2 deposited on SiO_2 for 10 min (a and c) and 18 min (b and d). The radius is calculated from $r = \sqrt{S/\pi}$, where S is projected area and the islands are assumed to be circular. Nuclei with the height less than 2 nm are not recognized.

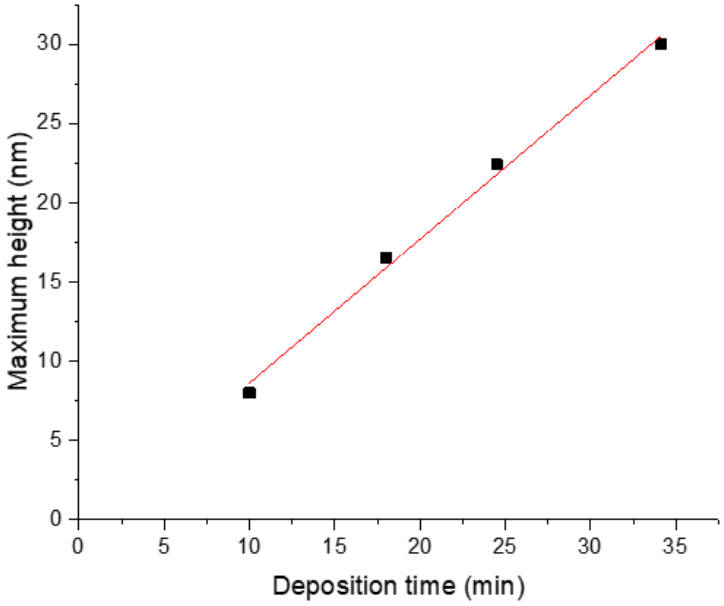

Figure 4.5. Maximum height of HfB_2 islands on SiO_2 with various deposition times. The red solid line is the linear fitting result. The intercept is -0.43 and the slope 0.91.

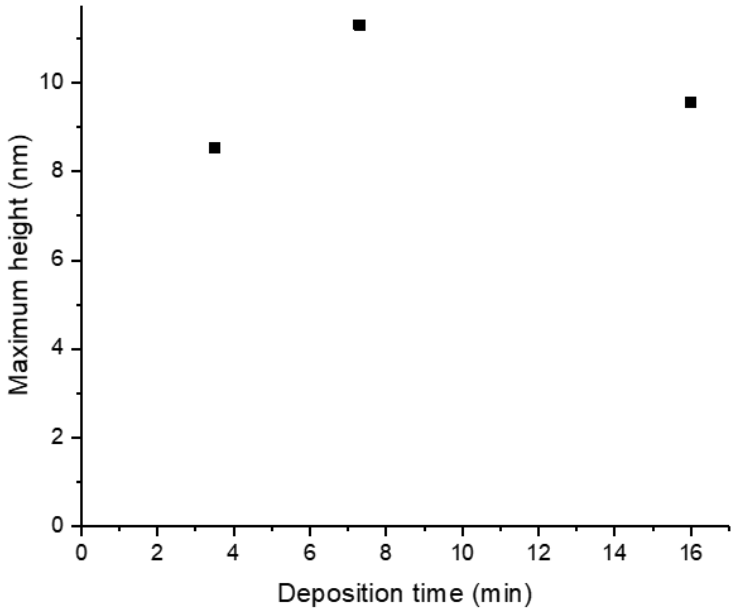

Figure 4.6. Maximum height of HfB_2 islands on Al_2O_3 with various deposition times.

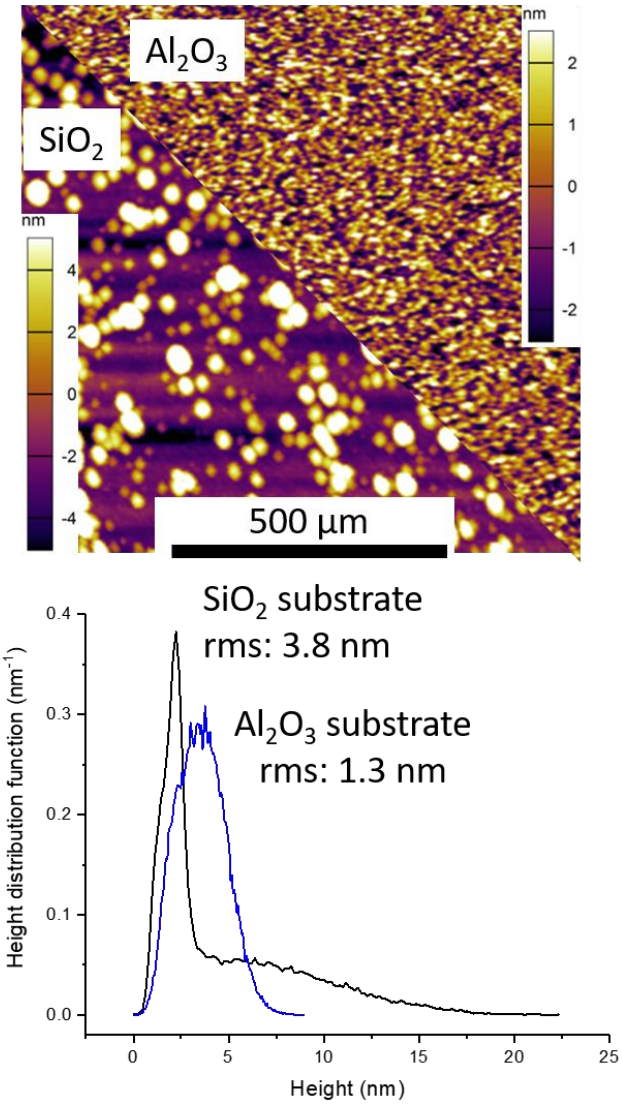

Figure 4.7. AFM images and height distribution functions for HfB_2 films of similar mean thicknesses (0.39 nm vs. 0.59 nm) for deposition times of 24.5 and 3.5 min on SiO_2 and Al_2O_3, respectively. On SiO_2, the sharp peak is mainly from the substrate surface and the broad shoulder is from HfB_2 islands. On Al_2O_3, there is no substrate contribution to the data.

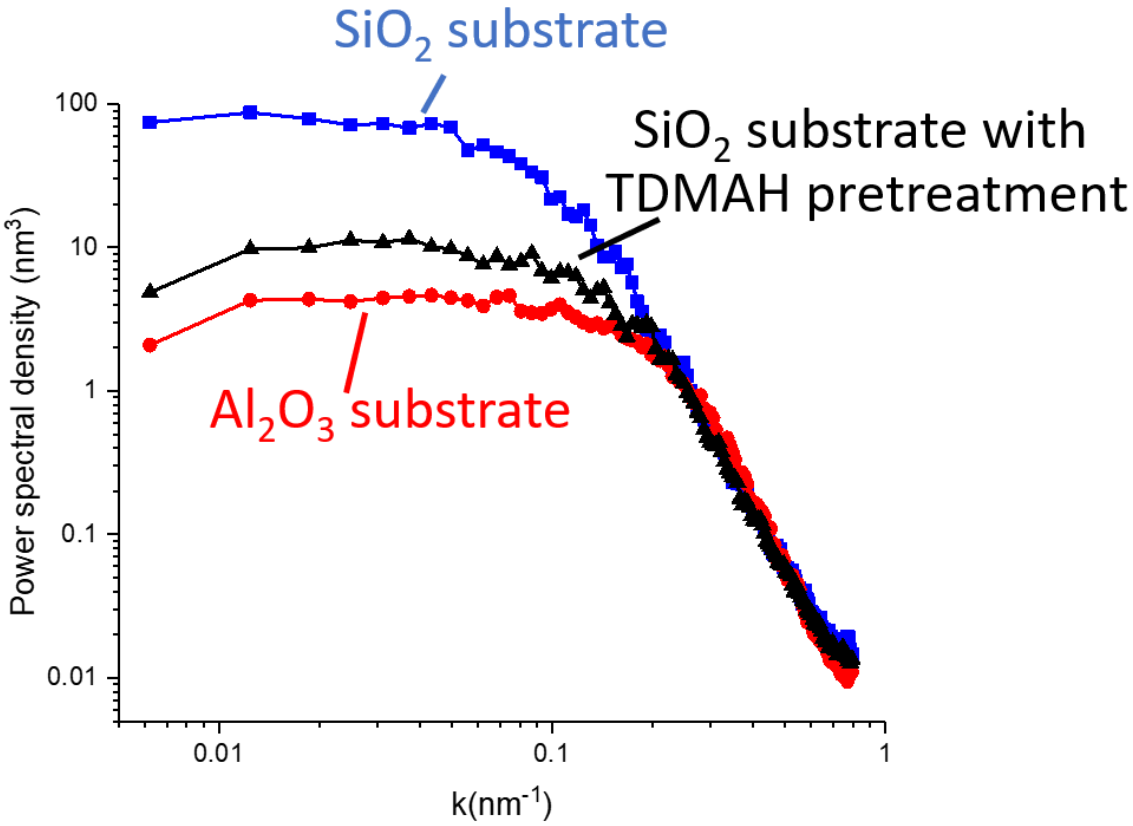

Figure 4.8. Power spectral density of surface roughness from AFM data for samples in Fig. 4.4 and the sample on SiO_2 substrate with TDMAH pretreatment. All samples have similar thickness (from top to bottom: 0.39 nm, 0.42 nm, 0. 59 nm). Deposition time is 24.5 min, 16.5 min and 3.5 min.

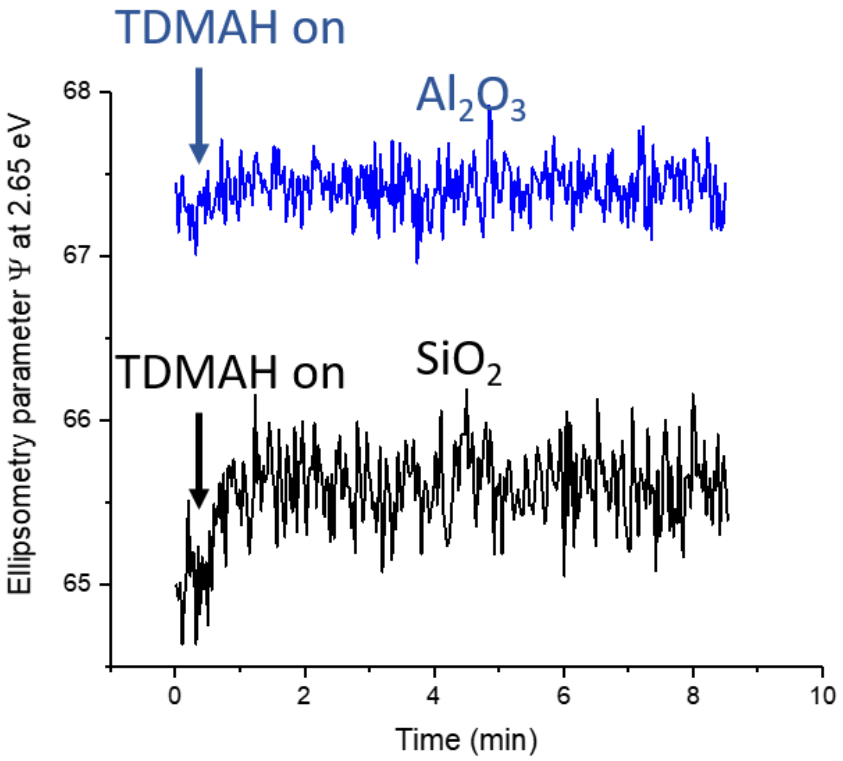

Figure 4.9. In situ ellipsometry parameter Ψ, at a photon energy of 2.65 eV, vs time for TDMAH dosing on SiO_2 and Al_2O_3 at 220 °C. Curves are shifted vertically to be displayed in the same range. Ellipsometry curve shows no change for TDMAH dosing on Al_2O_3, however, TDMAH does adsorb on Al_2O_3, evidenced by RBS. Continuous deposition does not occur as evidenced by the flat ellipsometry curve.

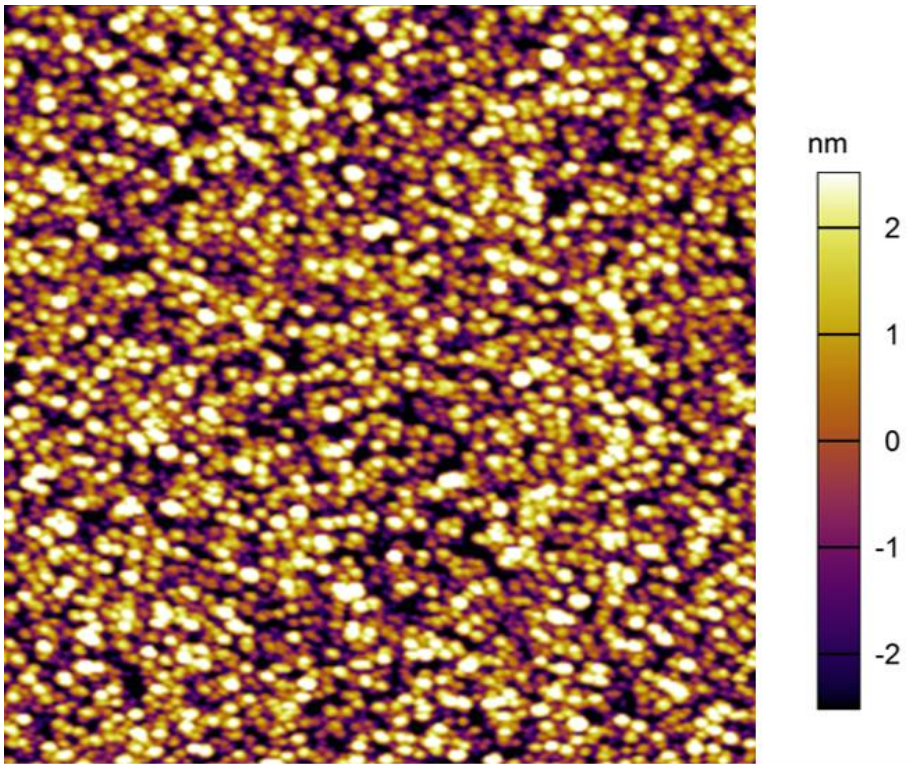

Figure 4.10. AFM image for HfB_2 on SiO_2 with TDMAH pretreatment. Deposition time is 16.5 min.

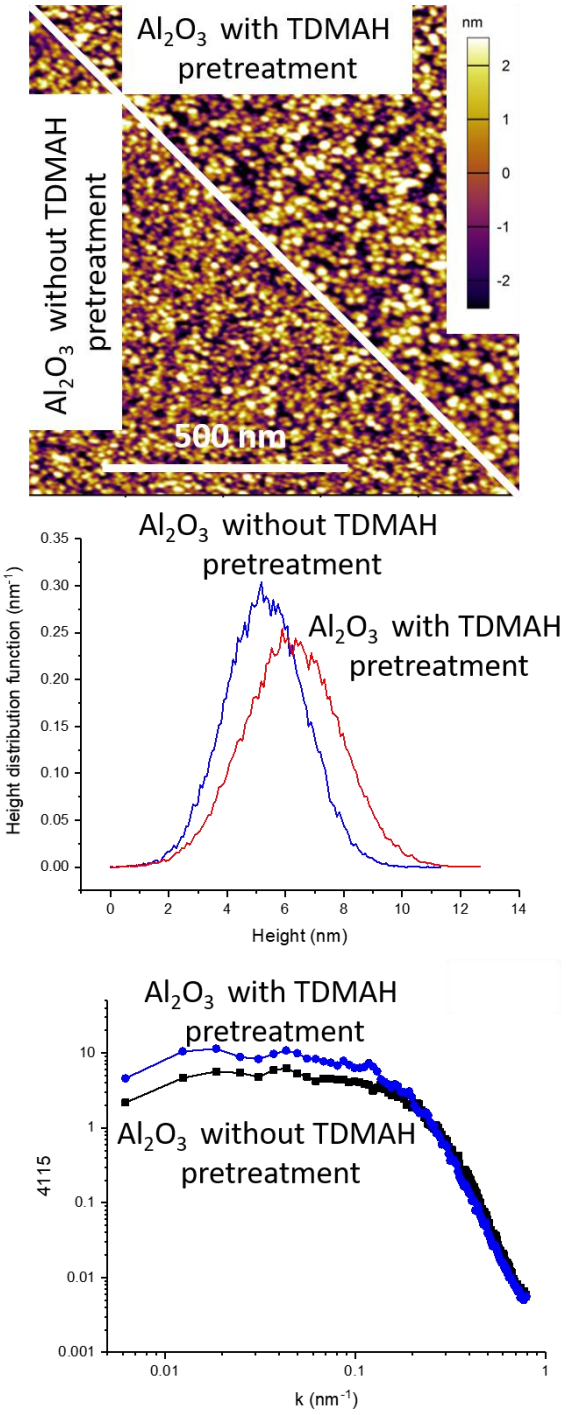

Figure 4.11. AFM images, height distribution functions and PSD for HfB_2 films of similar average thickness (1.86 nm vs. 1.94 nm) for deposition times of 7.3 min and 8.3 min on Al_2O_3, respectively. Both AFM images have the same scale bar and false color scale.

4.6 References

1. A. E. Kaloyeros, Y. Pan, J. Goff, and B. Arkles, "Editors' choice—review—cobalt thin films: Trends in processing technologies and emerging applications," *ECS Journal of Solid State Science and Technology* **8,** P119-P52 (2019).

2. E. Mohimi, Z. V. Zhang, S. M. Liu, J. L. Mallek, G. S. Girolami, and J. R. Abelson, "Area selective cvd of metallic films from molybdenum, iron, and ruthenium carbonyl precursors: Use of ammonia to inhibit nucleation on oxide surfaces," *Journal of Vacuum Science & Technology A* **36,** 041507 (2018).

3. Z. V. Zhang, S. Liu, G. S. Girolami, and J. R. Abelson, "Area-selective chemical vapor deposition of cobalt from dicobalt octacarbonyl: Enhancement of dielectric-dielectric selectivity by adding a coflow of nh3," *Journal of Vacuum Science & Technology A* **38,** 033401 (2020).

4. Y. Yang, S. Jayaraman, B. Sperling, D. Y. Kim, G. S. Girolami, and J. R. Abelson, "In situ spectroscopic ellipsometry analyses of hafnium diboride thin films deposited by single-source chemical vapor deposition," *Journal of Vacuum Science & Technology A* **25,** 200-6 (2007).

5. A. J. M. Mackus, M. J. M. Merkx, and W. M. M. Kessels, "From the bottom-up: Toward area-selective atomic layer deposition with high selectivity," *Chemistry of Materials* **31,** 2-12 (2019).

6. Y. Hwang, B. M. Nguyen, and S. A. Dayeh, "Atomic layer deposition of platinum with enhanced nucleation and coalescence by trimethylaluminum pre-pulsing," *Applied Physics Letters* **103,** 263115 (2013).

7. B. N. Zope and A. V. Gelatos, "Surface treatment to improve cctba based cvd co nucleation on dielectric substrate," United States US 9,218,980 B2

8. H. Han, J. J. Kim, and D. Y. Yoon, "Pretreatment technique for surface improvement of ru films in ru-metalorganic chemical vapor deposition," *Journal of Vacuum Science & Technology A: Vacuum, Surfaces, and Films* **22,** 1120-3 (2004).

9. N. Kumar, A. Yanguas-Gil, S. R. Daly, G. S. Girolami, and J. R. Abelson, "Remote plasma treatment of si surfaces: Enhanced nucleation in low-temperature chemical vapor deposition," *Applied Physics Letters* **95,** 144107 (2009).

10. K. S. Choi, J. M. Lim, S. Roy, and C. M. Lee, "Enhancement of ru nucleation in ru-metal organic chemical vapor deposition by electron cyclotron resonance plasma pretreatment," *Jpn J Appl Phys 1* **42,** 5539-42 (2003).

11. S. L. Zhejun Zhang, Gregory S. Girolami, John R. Abelson, "Ultra-smooth cobalt films on sio2: Cvd using a nucleation promoter and a growth inhibitor," *In preparation*.

12. G. Ruhl, B. Froschle, P. Ramm, A. Intemann, and W. Pamler, "Deposition of titanium nitride/tungsten layers for application in vertically integrated-circuits technology," *Applied Surface Science* **91,** 382-7 (1995).

13. V. Kamineni, M. Raymond, S. Siddiqui, F. Mont, S. Tsai, C. Niu, A. Labonte, C. Labelle, S. Fan, B. Peethala, P. Adusumilli, R. Patlolla, D. Priyadarshini, Y. Mignot, A. Carr, S. Pancharatnam, J. Shearer, C. Surisetty, J. Arnold, D. Canaperi, B. Haran, H. Jagannathan, F. Chafik, and B. L. Herron, "Tungsten and cobalt metallization: A material study for mol local interconnects," 2016, p. 105-7. [DOI: 10.1109/IITC-AMC.2016.7507698]

14. S. Babar, N. Kumar, P. Zhang, and J. R. Abelson, "Growth inhibitor to homogenize nucleation and obtain smooth hfb_2 thin films by chemical vapor deposition," *Chemistry of Materials* **25,** 662-7 (2013).

15. S. Babar, L. M. Davis, P. Y. Zhang, E. Mohimi, G. S. Girolami, and J. R. Abelson, "Chemical vapor deposition of copper: Use of a molecular inhibitor to afford uniform nanoislands or smooth films," *Ecs Journal of Solid State Science and Technology* **3,** Q79-Q83 (2014).

16. J. J. Kim, M. S. Kim, and D. Y. Yoon, "Effects of an added iodine source (c2h5i) on ru metal–organic chemical vapor deposition," *Chemical Vapor Deposition* **9,** 105-9 (2003).

17. J. J. Kim, D. H. Jung, M. S. Kim, S. H. Kim, and D. Y. Yoon, "Surface roughness reducing effect of iodine sources (ch3i, c2h5i) on ru and ruo2 composite films grown by mocvd," *Thin Solid Films* **409,** 28-32 (2002).

18. K. M. Thom and J. G. Ekerdt, "The effect of an iodine source on nucleation and film properties of ru films deposited by chemical vapor deposition," *Thin Solid Films* **518,** 36-42 (2009).

19. W. Liao and J. G. Ekerdt, "Effect of co on ru nucleation and ultra-smooth thin film growth by chemical vapor deposition at low temperature," *Chemistry of Materials* **25,** 1793-9 (2013).

20. S. Jayaraman, Y. Yang, D. Y. Kim, G. S. Girolami, and J. R. Abelson, "Hafnium diboride thin films by chemical vapor deposition from a single source precursor," *Journal of Vacuum Science & Technology A* **23,** 1619-25 (2005).

21. S. Jayaraman, E. J. Klein, Y. Yang, D. Y. Kim, G. S. Girolami, and J. R. Abelson, "Chromium diboride thin films by low temperature chemical vapor deposition," *Journal of Vacuum Science & Technology A* **23,** 631-3 (2005).

22. Y. Yang, S. Jayaraman, D. Y. Kim, G. S. Girolami, and J. R. Abelson, "Cvd growth kinetics of hfb2 thin films from the single-source precursor hf(bh4)(4)," *Chemistry of Materials* **18,** 5088-96 (2006).

23. P. A. Mulheran and D. A. Robbie, "Theory of the island and capture zone size distributions in thin film growth," *Europhys Lett* **49,** 617-23 (2000).

24. J. Soethoudt, F. Grillo, E. A. Marques, J. R. van Ommen, Y. Tomczak, L. Nyns, S. Van Elshocht, and A. Delabie, "Diffusion-mediated growth and size-dependent nanoparticle reactivity during ruthenium atomic layer deposition on dielectric substrates," *Advanced Materials Interfaces* **5,** 1800870 (2018).

25. M. F. J. Vos, S. N. Chopra, M. A. Verheijen, J. G. Ekerdt, S. Agarwal, W. M. M. Kessels, and A. J. M. Mackus, "Area-selective deposition of ruthenium by combining atomic layer deposition and selective etching," *Chemistry of Materials* **31,** 3878-82 (2019).

26. S. K. Song, H. Saare, and G. N. Parsons, "Integrated isothermal atomic layer deposition/atomic layer etching supercycles for area-selective deposition of tio2," *Chemistry of Materials* **31,** 4793-804 (2019).

27. W. Xie and G. N. Parsons, "Thermal atomic layer etching of metallic tungsten via oxidation and etch reaction mechanism using o2 or o3 for oxidation and wcl6 as the chlorinating etchant," *Journal of Vacuum Science & Technology A* **38,** 022605 (2020).

28. L. T. Zhuravlev, "The surface chemistry of amorphous silica. Zhuravlev model," *Colloids and Surfaces a-Physicochemical and Engineering Aspects* **173,** 1-38 (2000).

29. H. Knözinger and P. Ratnasamy, "Catalytic aluminas: Surface models and characterization of surface sites," *Catalysis Reviews* **17,** 31-70 (1978).

30. J. E. Gozum and G. S. Girolami, "Zirconium and hafnium polyhydrides - preparation and characterization of m2h3(bh4)5(pme3)2, mh(bh4)3(dmpe), and mh2(bh4)2(dmpe)2," *Journal of the American Chemical Society* **113,** 3829-37 (1991).

31. M. D. Fryzuk, S. J. Rettig, A. Westerhaus, and H. D. Williams, "Synthesis, stability, and fluxional behavior of binuclear mixed-hydride tetrahydroborate complexes of hafnium(iv) - x-ray crystal-structure of [[(me2pch2sime2)2n]hf(bh4)2](mu-h)3[hf(bh4)[n(sime2ch2pme2)2]]," *Inorg Chem* **24,** 4316-25 (1985).

32. G. A. Nesterov, V. A. Zakharov, V. V. Volkov, and K. G. Myakishev, "Catalysts prepared by the interaction of transition-metal tetrahydroborates with oxide supports - synthesis of surface ti, zr, hf hydrides and their catalytic properties in ethylene polymerization," *Journal of Molecular Catalysis* **36,** 253-69 (1986).

33. M. Kosmulski, "Isoelectric points and points of zero charge of metal (hydr)oxides: 50 years after parks' review," *Advances in Colloid and Interface Science* **238,** 1-61 (2016).

CHAPTER 5

CHEMICAL VAPOR DEPOSITION OF PLATINUM FROM $Pt[CH_2CMe_2CH_2CH=CH_2]_2$

5.1 Introduction

Platinum, as a noble metal, has a low electrical resistivity (10.8 μΩ·cm at 300 K), high catalytic activity and is resistant to oxidation even at elevated temperature [1-3]. These properties make platinum films a potential candidate for applications in microelectronics [4,5] and catalysts [6-8]. Many techniques have been developed to deposit platinum films, including sputtering [9,10], evaporation [11], electrodeposition [12], CVD (or PECVD) [6-8,13] and ALD [3,14,15]. Among them, CVD and ALD are gaining interests due to better control on thickness, morphology and conformality [16-21].

Many precursors have been proposed [22] for platinum deposition, such as β-diketonate [23]family complexes, trimethyl-cyclopentadienyl platinum variants [24], olefin and allyl containing precursors [25-27]. Pure platinum films can be grown in the presence of a reactive gas such as hydrogen, oxygen, ozone, or an oxygen plasma. Among all these precursors, trimethyl(methylcyclopentadienyl)platinum $(C_5H_4Me)PtMe_3$ has become the mostly widely employed [3,14,15,28-31] due to its high vapor pressure (53 mTorr at 23°C[32]) and stability at room temperature. One major drawback of the precursor is that it suffers from long nucleation delay [4,33-35]. Long delay normally indicates a bad nucleation, leading to rough films [3,22,31]. Also, precious precursors are wasted during the time of delay.

In this work, we will report CVD of platinum from a newly designed precursor, *cis*-bis(η1,η2-2,2-dimethylpent-4-en-1-yl)platinum ($Pt[CH_2CMe_2CH_2CH=CH_2]_2$). The molecule is stable towards air and moisture at room temperature. CVD of platinum from the precursor exhibits no nucleation delay on several substrates (Si (with native oxide), Al_2O_3, and vanadium nitride) and the films are smooth. At 330 °C in the absence of a reactive gas, the precursor deposits platinum containing 50% carbon; the growth rate of 1.0 Å/min is reaction-limited and

increases exponentially with increasing temperature. The resistivity is high at 860 μΩ·cm for a 12-nm film). When growth is carried out in the presence of a remote oxygen plasma, the amount of carbon is greatly reduced to below the detection limit of RBS (<30 At%) and the growth rate increases to ~2.2 Å/min without affecting the film smoothness. The film is still under-dense (57% bulk density) and the resistivity is high (450 μΩ·cm for a 12-nm film), indicating carbon contamination is still significant. Smooth films are obtained from quick adsorption of precursor and suppression of self-catalytic reaction on Pt islands. Conformality of the process needs improvement, which we presumably attribute to the inhibited growth from by-products.

5.2 Experimental

CVD experiments are performed in a cold wall high vacuum chamber described elsewhere; the base pressure is $1x10^{-7}$ Torr, most of which is H_2 [16,36]. The precursor is loaded in a glass container, which is maintained at 75 °C in a water bath during experiments. A flow rate of 20 or 30 sccm argon (99.999%) is used as a carrier; the precursor is delivered into the chamber through a 0.4 cm i.d. stainless steel tube pointing toward the substrate to sustain a total chamber pressure of 2 mTorr or 3 mTorr, respectively. The pressure in the chamber background is measured by MKS Baratron® capacitance manometer (390HA-00001). A remote microwave plasma source consisting of a 9.5mm i.d. Pyrex tube with a 2.45GHz Evenson cavity located outside of the chamber was used to generate atomic oxygen from research grade dioxygen gas (99.999%). For these experiments, the flow of O_2 is regulated with a mass flow controller to establish a partial pressure in the chamber of 1.5 mTorr (a total chamber pressure of 3.5 mTorr or 4.5 mTorr). The net plasma power (forward minus reflected) is 70 W.

Several different substrates are tested. 10 nm films of Al_2O_3 are grown on Si (100) by ALD from trimethylaluminum and water at 80 °C. Vanadium nitride (VN) is grown by CVD from tetrakis(dimethylamido)vanadium and ammonia at 330 °C on Si (100). VN films are deposited before platinum growth in the same chamber, without exposure to the air. Silicon (Si (100) with native oxide) and Al_2O_3 substrates are cleaned by UV/ozone to remove ambient contaminations for 10 min before loading into the chamber. Test of conformality is on lithographically defined microtrenches with SiN_x walls as received without further cleaning. The temperatures are measured with a K-type thermocouple attached to the sample holder.

Real-time spectroscopic ellipsometry (SE) is used during growth to monitor the onset of nucleation. We report change in the ellipsometric angle Ψ at a single energy, 2.65 eV, which provides the greatest sensitivity to the onset of nucleation, as discussed previously [37]. Film thickness is measured by scanning electron microscopy (Hitachi 4800) and Rutherford backscattering spectroscopy (3SDH Pelletron). RBS measures areal atomic density and we report an equivalent film thickness calculated from the bulk density of Platinum. This value considers only platinum atoms, not contamination atoms like carbon. Growth rate is calculated from the division of equivalent film thickness and total growth time. For SEM images, each pixel accounts for 0.5 nm in distance, therefore, for a film of sub-20 nm, the error of the thickness measured by SEM is relatively large. In this work, values of thickness and growth rate are from RBS, unless stated otherwise. Film densities are calculated by comparing the thickness as measured by these two techniques. Carbon content in the films was measured by Rutherford backscattering spectroscopy. Surface roughness was measured by atomic force microscopy (Asylum Research Cypher) using a silicon nitride cantilever in contact mode. Film resistivities are measured using the 4-point-probe method for films on Al_2O_3 substrates.

5.3 Results and Discussion

5.3.1 Thermal CVD

At substrate temperatures between 275 and 330 °C, smooth and reflective films are deposited on various substrates (Si, Al_2O_3 and VN) without any co-reactant, such as O_2 or H_2. While maintaining the same substrate reservoir temperature and carrier gas flow rate (20 sccm), the growth rate (Å/min), though very small, increases exponentially with increasing temperature between 275 and 330 °C (Fig. 5.1). This result shows that growth under these conditions is in the reaction limited regime. The deduced activation energy of 18 kcal/mol (0.78 eV) is considerably smaller than the >1.5 eV activation energy seen for growth from $(C_5H_4Me)PtMe_3$ [4]. In addition, the onset temperature is ~ 25 °C lower than that of ~ 300 °C for $(C_5H_4Me)PtMe_3$ [24]. Both observations are consistent with the conclusion that $Pt[CH_2CMe_2CH_2CH{=}CH_2]_2$ is a more reactive molecule under CVD conditions than the cyclopentadienyl compound, as expected owing to the presence of the labile ω-alkenyl groups.

Interestingly, unlike growth from $(C_5H_4Me)PtMe_3$, which shows significant nucleation delays [4,33-35], growth from $Pt[CH_2CMe_2CH_2CH=CH_2]_2$ occurs without delay on all substrates tested (Fig. 5.2), indicating good nucleation (low activation energy) on all substrate surfaces. The films are also very smooth. For example, the film grown on an Al_2O_3 substrate at 330 °C has a rms roughness of 1.7 nm for a 13-nm film (from SEM) (Fig. 5.3).

As is typically seen for organoplatinum CVD precursors, the films in the absence of oxidative or reductive co-reactants contain both platinum and carbon. RBS analysis shows that the films grown at 330 °C consist of ~50 at. % platinum with the balance being carbon (Fig. 5.4). The film is so under-dense as RBS equivalent thickness is only 4.0 nm (17 nm in SEM), corresponding to only 24 % of the bulk density and the film is amorphous (Fig. 5.5a). Because of the presence of the latter [38-41], a 12 nm film deposited at 330 °C on Al_2O_3 has a relatively high resistivity of 830 μΩ·cm, vs. the 10.8 μΩ-cm value seen for bulk platinum.

5.3.2 Remote oxygen plasma assisted CVD

The quality of films grown by CVD from organoplatinum precursors is usually improved, and the growth rate is often increased, by addition of oxidants such as O_2 to the gas stream, which react with excess carbon to remove it as CO or CO_2 [4,24,42]. We find, however, that addition of reactant gases such as O_2 or H_2 [32] has no effect on the growth rate in this work (Fig. 5.6). This finding suggests that the Pt surface is poisoned in such a way that it is unable to activate these molecules such as O_2 or H_2. We therefore investigated lowering the carbon content of the films by employing a reactant that does not rely on the catalytic ability of platinum surface: atomic O generated by a low-power remote oxygen plasma [43]. Growth at 330 °C in the presence of a remote oxygen plasma also occurs with no nucleation delay, and the growth rate is increased to ~ 220 % of its value in the absence of the plasma (Fig. 5.1).

The density, purity, and crystallinity of the film grown in the presence of the oxygen plasma also shows significant improvement (Fig. 5.4): the oxygen and carbon contents are below the RBS detection limit (< ~30%) vs. the ~ 50% carbon content seen for films grown in the absence of a plasma. For a 12 nm thick film (as measured by SEM), the Pt content (as measured by RBS) is equivalent to a pure platinum film with thickness of 6.8 nm, which corresponds to 57% of bulk density, although this value has a large error owing to the thinness of

the films. Glancing angle XRD analysis shows that the film contains nanocrystalline platinum, with crystalline domains of ~7 nm in size (Fig. 5.5b). Films grown in the presence of the remote oxygen plasma are quite smooth: the rms roughness of 2.2 nm is comparable with the 1.7 nm value seen in the absence of the plasma (Fig. 5.3). Rougher surface may be attributed to better crystallinity, or existence of remote plasma enhancing diffusion of adatoms [44]. When substrate temperature is increased to 350 °C, carbon level seems to be increased to ~45 at. %, slightly over RBS detection limit. For an 18 nm thick film (as measured by SEM), the Pt content (as measured by RBS) is equivalent to a pure platinum film with thickness of 9.1 nm, which corresponds to 50 % of bulk density.

The use of the oxygen plasma also lowers the resistivity to 450 μΩ·cm for a 12 nm film deposited on Al_2O_3; this value, is about half that of films grown under otherwise identical conditions but without the oxygen plasma. The value is still too high compared with bulk value. The carbon level could be still high in this film as RBS is not sensitive to carbon.

5.3.3 Conformality in trench structures

As we described previously, the growth of platinum films in our conditions are reaction limited, and low reaction probabilities usually lead to a good conformality [45,46]. Conformality is tested by depositing platinum on a substrate with microtrenches (aspect ratio is 3) at 330 °C in the absence of oxygen plasma. Interestingly, the coating profile is not conformal (Fig. 5.7). On top of the trench, the thickness of platinum is ~14 nm (from SEM) for a total growth time of 40 min. However, in the bottom, the film can hardly be seen from SEM. Growth in the presence of oxygen plasma shares a similar result (Fig. 5.8). A possible reason is the byproducts that build up in the trench during growth, can inhibit platinum growth. There are quite a few byproducts in the reaction. We pick a major byproduct, 4,4-Dimethyl-1-pentene to demonstrate whether it has inhibition effect on platinum growth and only 8 nm (from SEM) film is deposited in 40 min in the presence of a 4,4-Dimethyl-1-pentene coflow (0.07 mTorr).

5.3.4 Discussion

As we discussed in chapter 2, 3 and 4, deposition of nucleation layers, or surface pretreatment can enhance nucleation and reduce nucleation delay. Here, another method is through molecular engineering so a precursor intrinsically with no nucleation is designed for deposition. Precursor design is beyond the scope of the dissertation. In short, the labile ω-alkenyl groups in $Pt[CH_2CMe_2CH_2CH=CH_2]_2$ allows quick adsorption of the precursor on most substrates (nucleation is enhanced).

Another problem in platinum deposition is self-catalytic growth. Decomposition typically occurs more quickly on platinum surfaces than underlying substrate (such as oxide), owing to the highly catalytic nature of platinum [4]. Thus, islands on the surface initiate and then followed by a rapid growth, leading to sparse nucleation and rough films. The fact that H_2 and O_2 cannot affect growth rate indicates all sites with catalytic activities are poisoned, i.e., self-catalytic growth is suppressed (growth of islands is inhibited). This is due to the formation of carbon-containing species that passivate the Pt surface.

As discussed in chapter 3 and 4, ultra-smooth films can be possibly obtained by combining nucleation enhancement and growth inhibition of islands. And thus, this precursor is capable to deposit smooth platinum films.

Currently, this precursor still suffers from high carbon contamination and slow growth rate, which prevent further applications. The flux of atomic oxygen in our remote plasma source is limited[47], and thus, it may prove possible to obtain films with even faster growth rates, lower carbon contents, and lower resistivities by employing a stronger plasma source or a more kinetic accessible oxidant such as ozone, which can directly react with organic species without surface mediated processes. Cyclic cleaning by plasma can also be considered to reduce carbon contamination. Another possible application is to form a nucleation layer, where slow growth rate is not a concern, for CVD/ALD of platinum from other precursors, such as $(C_5H_4Me)PtMe_3$. These experiments and analysis will be a subject of future work.

5.4 Conclusion

We investigate the growth of platinum on various substrates from a newly-design precursor, $Pt[CH_2CMe_2CH_2CH{=}CH_2]_2$. The deposition, requiring no co-reactant, has no nucleation delay and films are smooth. For example, the film grown on an Al_2O_3 substrate at 330 °C has a rms roughness of 1.7 nm for a 13-nm film (from SEM), although the films are contaminated by 50 at.% of carbon, the resistivity is high at 830 μΩ·cm and the growth rate is slow. These issues can be mitigated by introducing a remote oxygen plasma. However, the films we obtained still have a high resistivity and presumably high carbon contamination, probably due to a limited flux of atomic oxygen in our plasma source. Conformality of the process needs improvement, which we attribute to the inhibited growth from by-products.

5.5 Figures

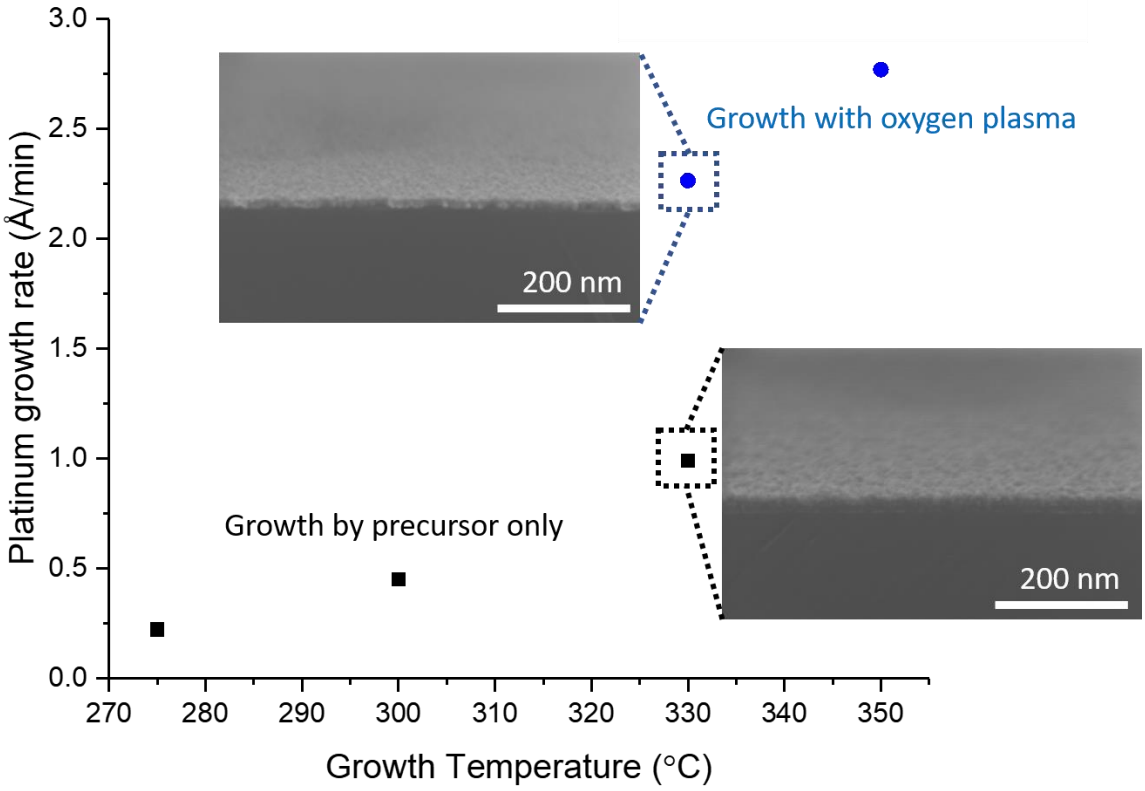

Figure 5.1. Influence of growth temperature and oxygen plasma on platinum growth rate. The growth rate was calculated from the ratio of film thickness (measured by RBS) and growth time. The inserts show two cross-sectional SEM images for the samples grown at 330 °C, with and without plasma, respectively.

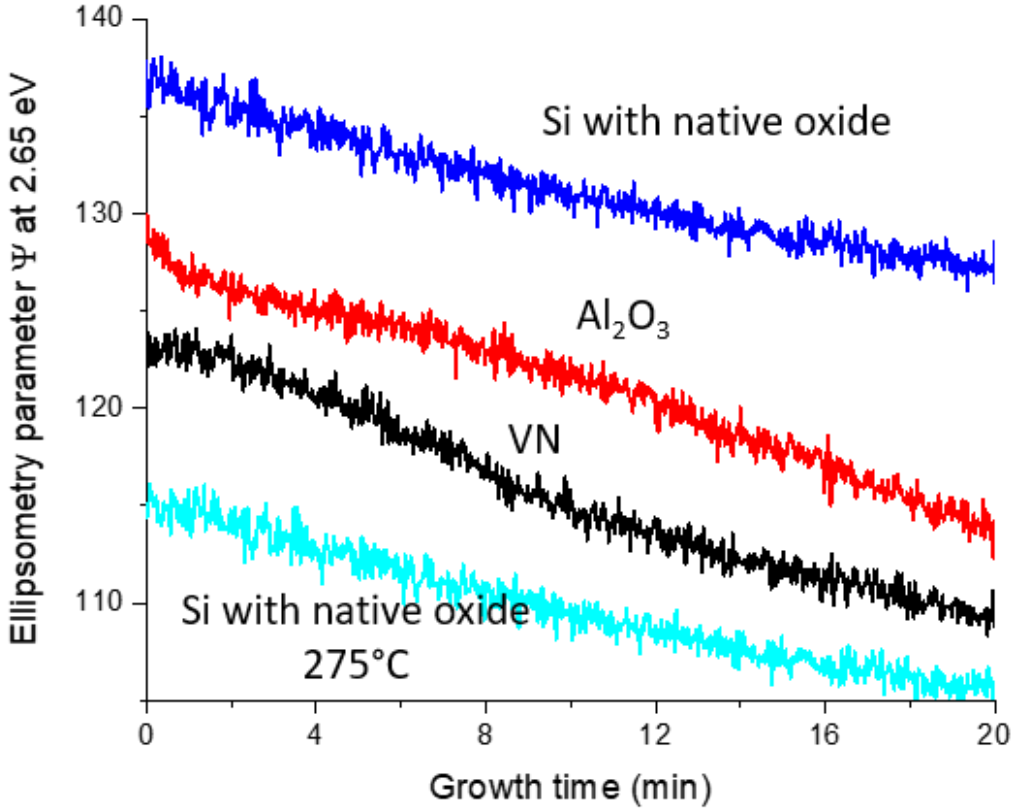

Figure 5.2. Real time ellipsometry curve (at 2.65 eV) of Pt growth on SiO_2, VN and Al_2O_3 without co-reactant. The bottom curve is for the growth at 275 °C and the rest are at 330 °C. The platinum precursor is introduced at the time of 0. Curves are shifted vertically to be displayed in the same range.

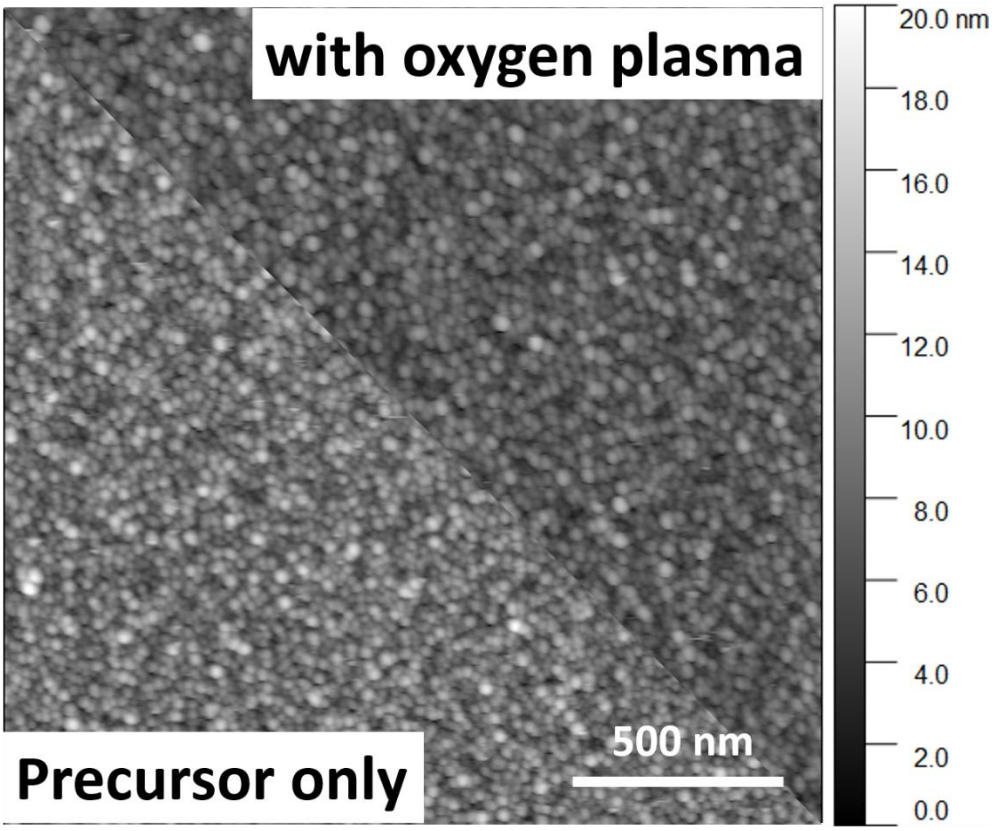

Figure 5.3. AFM image of Pt film grown by precursor only and with oxygen plasma at 330 °C on Al_2O_3 substrates.

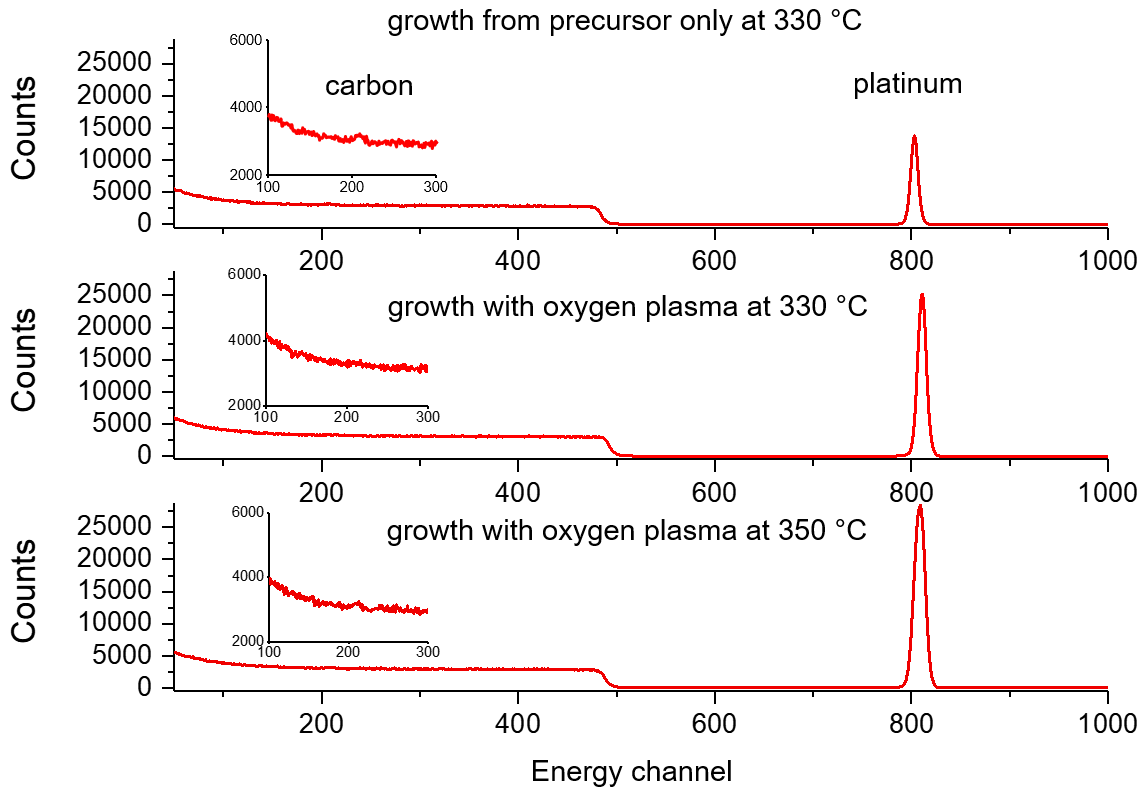

Figure 5.4. RBS spectra of Pt films grown without and with oxygen plasma.

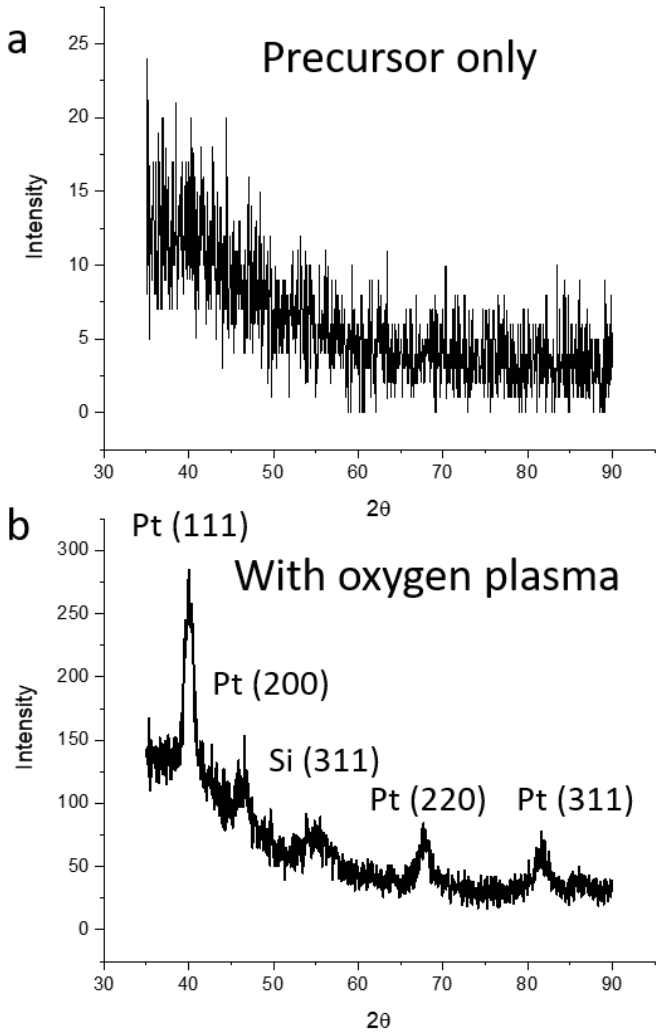

2θ	d(Å)	FWHM	XS(Å)
39.930 (0.063)	2.2560 (0.0068)	1.222 (0.080)	71 (6)
46.621 (0.194)	1.9466 (0.0153)	1.318 (0.273)	67 (15)
67.704 (0.128)	1.3828 (0.0046)	1.502 (0.216)	65 (10)
81.570 (0.164)	1.1792 (0.0039)	1.755 (0.257)	61 (10)

Figure 5.5. Glancing angle (1°) XRD spectrum of the Pt films grown 330 °C from precursor only (a) and in presence of an oxygen plasma (b). The film in (a) does not show observable XRD peaks (17 nm in thickness from SEM). The film in (b) contains nanocrystalline platinum, with crystalline domains of ~7 nm in size (12 nm in thickness from SEM).

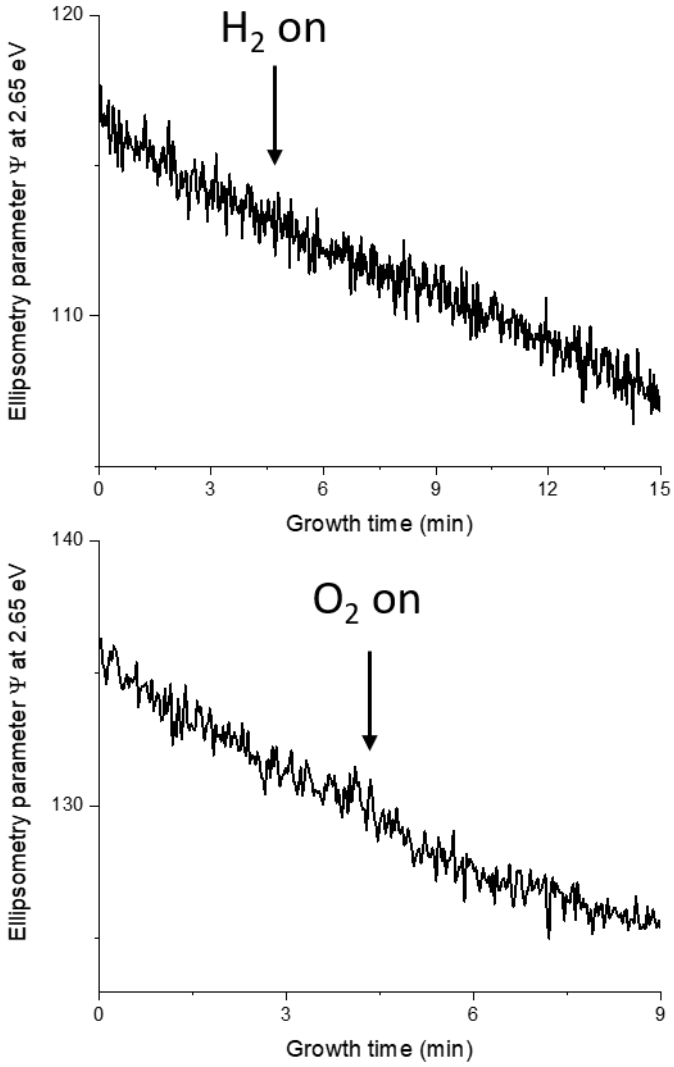

Figure 5.6. Real time ellipsometry curve (at 2.65 eV) of Pt growth at 330 °C. Precursor molecules are flowing the whole time. Introduction of H_2 or O_2 does not change the slope of ellipsometry curves, indicating the growth rate is not changed.

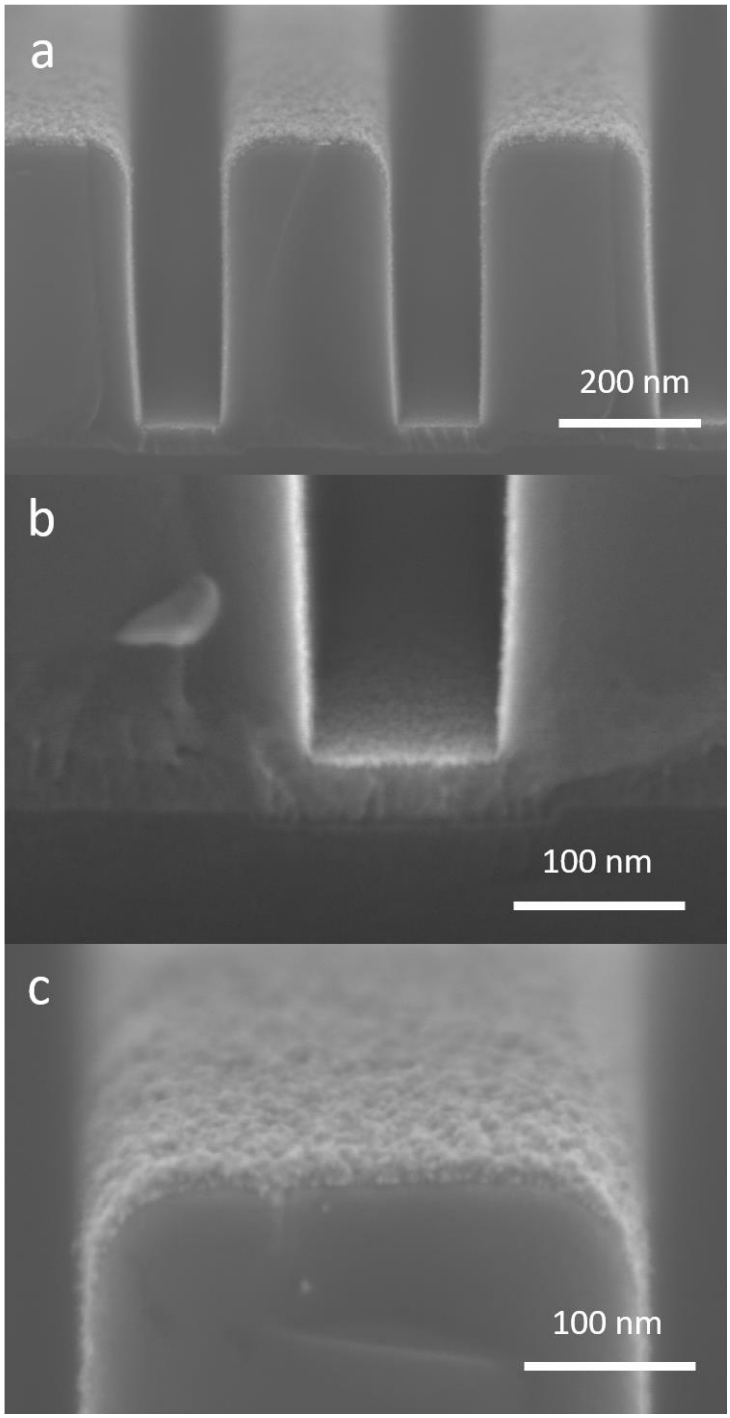

Figure 5.7. Cross-sectional SEM images of Pt in trenches. The growth proceeds in the absence of an oxygen plasma. The aspect ratio of the trenches is 3. (b) and (c) are enlarged areas for the bottom and top of the trench, respectively, in (a). The total growth time is 40 min.

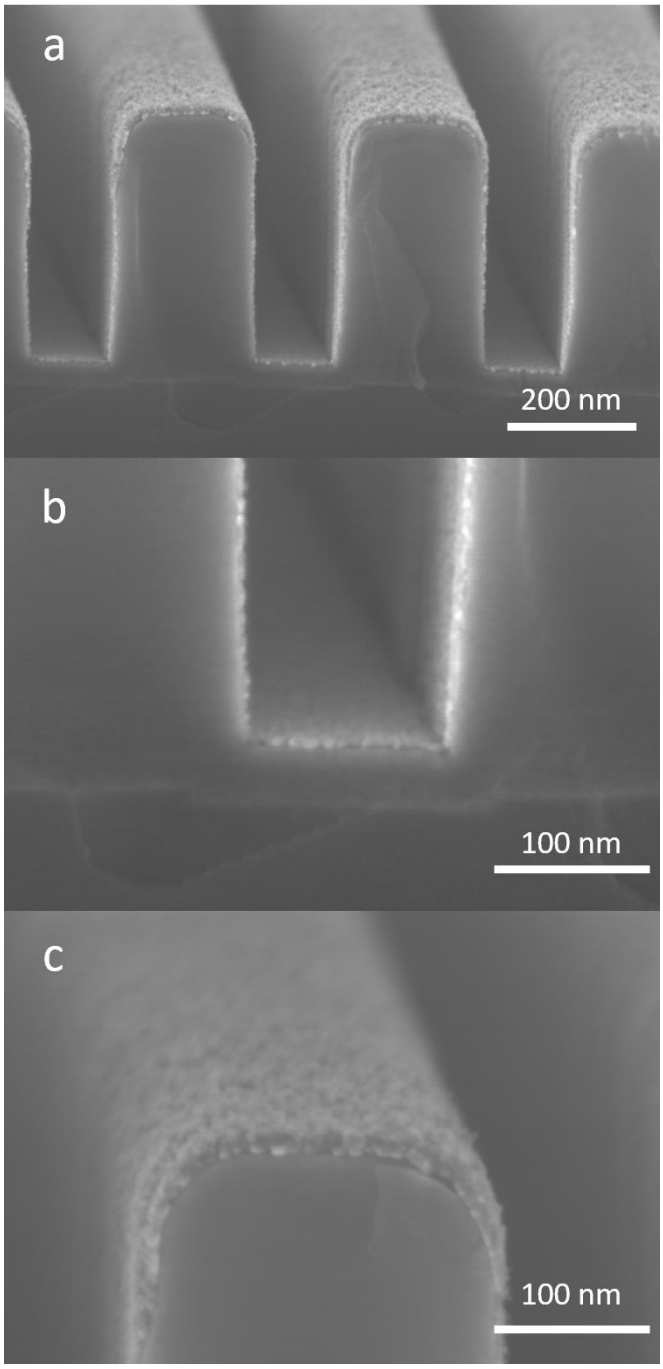

Figure 5.8. Cross-sectional SEM images of Pt in trenches. The growth proceeds in the presence of an oxygen plasma. The aspect ratio of the trenches is 3. (b) and (c) are enlarged areas for the bottom and top of the trench, respectively, in (a). The total growth time is 30 min.

5.6 References

1. J. W. Arblaster, "Selected electrical resistivity values for the platinum group of metals part i: Palladium and platinum improved values obtained for liquid phases of palladium and platinum," *Johnson Matthey Technology Review* **59,** 174-81 (2015).

2. B. C. Mallick, C.-T. Hsieh, K.-M. Yin, Y. A. Gandomi, and K.-T. Huang, "Review—on atomic layer deposition: Current progress and future challenges," *ECS Journal of Solid State Science and Technology* **8,** N55-N78 (2019).

3. T. Aaltonen, M. Ritala, T. Sajavaara, J. Keinonen, and M. Leskela, "Atomic layer deposition of platinum thin films," *Chemistry of Materials* **15,** 1924-8 (2003).

4. M. Hiratani, T. Nabatame, Y. Matsui, K. Imagawa, and S. Kimura, "Platinum film growth by chemical vapor deposition based on autocatalytic oxidative decomposition," *Journal of The Electrochemical Society* **148,** C524-C7 (2001).

5. T. H. Baum and P. B. Comita, "Laser-induced chemical vapor deposition of metals for microelectronics technology," *Thin Solid Films* **218,** 80-94 (1992).

6. J. C. Hierso, P. Serp, R. Feurer, and P. Kalck, "Mocvd of rhodium, palladium and platinum complexes on fluidized divided substrates: Novel process for one-step preparation of noble-metal catalysts," *Applied Organometallic Chemistry* **12,** 161-72 (1998).

7. C. Dossi, R. Psaro, A. Bartsch, A. Fusi, L. Sordelli, R. Ugo, M. Bellatreccia, R. Zanoni, and G. Vlaic, "Chemical-vapor-deposition of platinum hexafluoroacetylacetonate inside kl zeolite - a new route to nonacidic platinum-in-zeolite catalysts," *Journal of Catalysis* **145,** 377-83 (1994).

8. P. Serp, P. Kalck, and R. Feurer, "Chemical vapor deposition methods for the controlled preparation of supported catalytic materials," *Chem Rev* **102,** 3085-128 (2002).

9. E. Slavcheva, G. Ganske, G. Topalov, W. Mokwa, and U. Schnakenberg, "Effect of sputtering parameters on surface morphology and catalytic efficiency of thin platinum films," *Applied Surface Science* **255,** 6479-86 (2009).

10. P. Brault, A. Caillard, A. L. Thomann, J. Mathias, C. Charles, R. W. Boswell, S. Escribano, J. Durand, and T. Sauvage, "Plasma sputtering deposition of platinum into porous fuel cell electrodes," *Journal of Physics D: Applied Physics* **37,** 3419-23 (2004).

11. W. Macherzyński, M. Wośko, B. Paszkiewicz, B. Ściana, R. Paszkiewicz, and M. Tłaczała, "Fabrication of ohmic contact based on platinum to p-type compositionally graded algaas layers," *Journal of Physics: Conference Series* **146,** 012034 (2009).

12. M. Baumgärtner and J. Raub, "The electrodeposition of platinum and platinum alloys," *Platinum Metals Review* **32,** 188-97 (1988).

13. M. Ritala, J. Niinisto, S. Krumdieck, P. Chalker, H. Aspinall, M. E. Pemble, W. L. Gladfelter, B. Leese, R. A. Fischer, and H. Parala, *Chemical vapour deposition: Precursors, processes and applications* (Royal Society of Chemistry, 2008). [DOI:

14. A. J. M. Mackus, D. Garcia-Alonso, H. C. M. Knoops, A. A. Bol, and W. M. M. Kessels, "Room-temperature atomic layer deposition of platinum," *Chemistry of Materials* **25,** 1769-74 (2013).

15. H. Knoops, A. Mackus, M. Donders, M. Van De Sanden, P. Notten, and W. Kessels, "Remote plasma ald of platinum and platinum oxide films," *Electrochemical and Solid-State Letters* **12,** G34-G6 (2009).

16. S. Jayaraman, Y. Yang, D. Y. Kim, G. S. Girolami, and J. R. Abelson, "Hafnium diboride thin films by chemical vapor deposition from a single source precursor," *Journal of Vacuum Science & Technology A* **23,** 1619-25 (2005).

17. T. K. Talukdar, S. Liu, Z. Zhang, F. Harwath, G. S. Girolami, and J. R. Abelson, "Conformal mgo film grown at high rate at low temperature by forward-directed chemical vapor deposition," *Journal of Vacuum Science & Technology A* **36,** 051504 (2018).

18. J. Lee, H. J. Yang, J. H. Lee, J. Y. Kim, W. J. Nam, H. J. Shin, Y. K. Ko, J. G. Lee, E. G. Lee, and C. S. Kim, "Highly conformal deposition of pure co films by mocvd using co-2(co)(8) as a precursor," *Journal of the Electrochemical Society* **153,** G539-G42 (2006).

19. W. B. Wang, N. N. Chang, T. A. Codding, G. S. Girolami, and J. R. Abelson, "Superconformal chemical vapor deposition of thin films in deep features," *Journal of Vacuum Science & Technology A* **32,** 051512 (2014).

20. T. K. Talukdar, W. B. Wang, G. S. Girolami, and J. R. Abelson, "Superconformal coating and filling of deep trenches by chemical vapor deposition with forward-directed fluxes," *Journal of Vacuum Science & Technology A* **36,** 051513 (2018).

21. Y. Hwang, B. M. Nguyen, and S. A. Dayeh, "Atomic layer deposition of platinum with enhanced nucleation and coalescence by trimethylaluminum pre-pulsing," *Applied Physics Letters* **103,** 263115 (2013).

22. C. Thurier and P. Doppelt, "Platinum omcvd processes and precursor chemistry," *Coordination Chemistry Reviews* **252,** 155-69 (2008).

23. G. Malandrino, R. L. Nigro, and I. L. Fragalà, "Mocvd of platinum (100) films on random hastelloy c276," *Chemical Vapor Deposition* **5,** 59-61 (1999).

24. A. J. M. Mackus, N. Leick, L. Baker, and W. M. M. Kessels, "Catalytic combustion and dehydrogenation reactions during atomic layer deposition of platinum," *Chemistry of Materials* **24,** 1752-61 (2012).

25. C. D. Tagge, R. D. Simpson, R. G. Bergman, M. J. Hostetler, G. S. Girolami, and R. G. Nuzzo, "Synthesis of a novel volatile platinum complex for use in cvd and a study of the

mechanism of its thermal decomposition in solution," *Journal of the American Chemical Society* **118,** 2634-43 (1996).

26. M. Aktary, C. E. Lee, Y. Xing, S. H. Bergens, and M. T. McDermott, "Surface-directed deposition of platinum nanostructures on graphite by chemical vapor deposition," *Langmuir* **16,** 5837-40 (2000).

27. R. U. Kirss, "Organometallic chemical vapor deposition using allyl precursors," *Applied Organometallic Chemistry* **6,** 609-17 (1992).

28. X. Jiang and S. F. Bent, "Area-selective atomic layer deposition of platinum on ysz substrates using microcontact printed sams," *Journal of The Electrochemical Society* **154,** D648-D56 (2007).

29. Y. Zhu, K. A. Dunn, and A. E. Kaloyeros, "Properties of ultrathin platinum deposited by atomic layer deposition for nanoscale copper-metallization schemes," *Journal of Materials Research* **22,** 1292-8 (2011).

30. T. Aaltonen, M. Ritala, Y.-L. Tung, Y. Chi, K. Arstila, K. Meinander, and M. Leskelä, "Atomic layer deposition of noble metals: Exploration of the low limit of the deposition temperature," *Journal of Materials Research* **19,** 3353-8 (2004).

31. P. Baumann, P. Doppelt, K. Fröhlich, L. Gueroudji, V. Cambel, D. Machajdik, M. Schumacher, J. Lindner, F. Schienle, and D. Burgess, "Platinum, ruthenium and ruthenium dioxide electrodes deposited by metal organic chemical vapor deposition for oxide applications," *Integrated Ferroelectrics* **44,** 135-42 (2002).

32. Z. Xue, M. J. Strouse, D. K. Shuh, C. B. Knobler, H. D. Kaesz, R. F. Hicks, and R. S. Williams, "Characterization of (methylcyclopentadienyl)trimethylplatinum and low-temperature organometallic chemical vapor deposition of platinum metal," *Journal of the American Chemical Society* **111,** 8779-84 (1989).

33. Z. Xue, H. Thridandam, H. D. Kaesz, and R. F. Hicks, "Organometallic chemical vapor deposition of platinum. Reaction kinetics and vapor pressures of precursors," *Chemistry of Materials* **4,** 162-6 (1992).

34. J. Dendooven, R. K. Ramachandran, K. Devloo-Casier, G. Rampelberg, M. Filez, H. Poelman, G. B. Marin, E. Fonda, and C. Detavernier, "Low-temperature atomic layer deposition of platinum using (methylcyclopentadienyl)trimethylplatinum and ozone," *The Journal of Physical Chemistry C* **117,** 20557-61 (2013).

35. A. J. M. Mackus, M. A. Verheijen, N. Leick, A. A. Bol, and W. M. M. Kessels, "Influence of oxygen exposure on the nucleation of platinum atomic layer deposition: Consequences for film growth, nanopatterning, and nanoparticle synthesis," *Chemistry of Materials* **25,** 1905-11 (2013).

36. S. Jayaraman, E. J. Klein, Y. Yang, D. Y. Kim, G. S. Girolami, and J. R. Abelson, "Chromium diboride thin films by low temperature chemical vapor deposition," *Journal of Vacuum Science & Technology A* **23,** 631-3 (2005).

37. S. Babar, E. Mohimi, B. Trinh, G. S. Girolami, and J. R. Abelson, "Surface-selective chemical vapor deposition of copper films through the use of a molecular inhibitor," *Ecs Journal of Solid State Science and Technology* **4,** N60-N3 (2015).

38. A. A. Zinn, "Chemical vapor deposition of tungsten," in *The chemistry of metal cvd*, edited by T. T. K. a. M. J. Hampden-Smith (2007), p. 147. [DOI: doi:10.1002/9783527615858.ch3]

39. J. R. Sambles, "The resistivity of thin metal films—some critical remarks," *Thin Solid Films* **106,** 321-31 (1983).

40. "Basic concepts," in *The electrical resistivity of metals and alloys*, edited by P. L. Rossiter (Cambridge University Press, Cambridge, 1987), p. 1-29. [DOI: DOI: 10.1017/CBO9780511600289.002]

41. A. F. Mayadas and M. Shatzkes, "Electrical-resistivity model for polycrystalline films: The case of arbitrary reflection at external surfaces," *Physical Review B* **1,** 1382-9 (1970).

42. T. Aaltonen, A. Rahtu, M. Ritala, and M. Leskelä "Reaction mechanism studies on atomic layer deposition of ruthenium and platinum," *Electrochem. Solid-State Lett.* **6,** C130-C3 (2003).

43. H. C. M. Knoops, A. J. M. Mackus, M. E. Donders, M. C. M. van de Sanden, P. H. L. Notten, and W. M. M. Kessels, "Remote plasma ald of platinum and platinum oxide films," *Electrochem. Solid-State Lett.* **12,** G34-G6 (2009).

44. J. Thornton, *Structure-zone models of thin films*, Vol. 0821 (SPIE, 1988). [DOI:

45. A. Yanguas-Gil, N. Kumar, Y. Yang, and J. R. Abelson, "Highly conformal film growth by chemical vapor deposition. Ii. Conformality enhancement through growth inhibition," *Journal of Vacuum Science & Technology A* **27,** 1244-8 (2009).

46. A. Yanguas-Gil, Y. Yang, N. Kumar, and J. R. Abelson, "Highly conformal film growth by chemical vapor deposition. I. A conformal zone diagram based on kinetics," *Journal of Vacuum Science & Technology A* **27,** 1235-43 (2009).

47. E. Mohimi, Z. V. Zhang, J. L. Mallek, S. Liu, B. B. Trinh, P. P. Shetty, G. S. Girolami, and J. R. Abelson, "Low temperature chemical vapor deposition of superconducting vanadium nitride thin films," *Journal of Vacuum Science & Technology A* **37,** 031509 (2019).

CHAPTER 6

INFRARED REFLECTION SPECTROSCOPY OF ADSORBED INTERMEDIATES DURING CHEMICAL VAPOR DEPOSITION OF OXIDES

6.1 Introduction

Our group has developed several chemical vapor deposition (CVD) processes that afford highly conformal and superconformal coating of thin films in deep trenches [1-4]. These processes exhibit growth rate kinetics that are consistent with competitive adsorption between a precursor molecule and a co-reactant or a growth inhibitor. Microscopic models based on Langmuir isotherms have been proposed to explain the observations [5,6]; however, the actual coverage of the adsorbates on the surface during deposition has not been measured experimentally. It is experimentally challenging to measure the surface coverage in-situ and in real time during a CVD process because the adsorbed quantities are sub-monolayer, there is a partial pressure of precursor molecules in the chamber and electron spectroscopies cannot be used because the electron beam will stimulate chemical reactions. Besides, film growth is a dynamic process, which means that the optical response of the film-on-substrate combination may change during the IR measurement. For these reasons, we apply infrared spectroscopy (IR) in reflectance mode from a planar substrate to detect the identity and concentration of surface adsorbates during CVD.

IR has previously been used to evaluate surface reactions during film growth by atomic layer deposition (ALD) [7-9]. In ALD, the measurement problem is considerably simpler because precursor molecules and co-reactants are introduced sequentially; after each pulse the chamber is evacuated and the molecules adsorbed on the growth surface are quasi-static (they remain until the co-reactant molecules are injected on the following pulse). A large number of interferometer scans can be taken during the quasi-static period; and the chamber windows can be protected from adsorption (covered) during the gas pulses.

It is more challenging to apply FTIR in real time during CVD because (i) gas phase molecules in the beam path, and molecules adsorbed on the IR chamber windows, contribute a significant background adsorption that may mask the signal from the growth surface; and (ii) continuous growth of the film on the substrate may change the IR background or sensitivity to the adsorbates.. Real-time FTIR has been used for CVD, but only to detect gas phase species [10,11]. Our group previously used FTIR in real time to analyze reactive sputter deposition of hydrogenated amorphous silicon films [12-15]. In that system, the IR modes of gas phase species do not overlap with those in the film, which eliminates problem (i); and we used a carefully designed multilayer substrate to eliminate problem (ii).

Since the pioneering work of Greenler [16], infrared reflection absorption spectroscopy (IRRAS) has been widely used to study thin films [17], gas-liquid interfaces [18], Langmuir-Blodgett monolayers [19], or solution-based surface adsorption and reaction [20] on metallic substrates. These applications use polarized light at grazing incident angle; in p-polarization the superposition of incident and reflected waves enhances the surface electric field and the absorption strength, whereas in s-polarization there is no surface electric field and no surface absorption. By contrast, absorption from molecules in the beam path, and molecules adsorbed on windows (at normal incidence) is not polarization dependent. *Thus, subtraction of the s-polarized signal from the p-polarized signal removes the unpolarized component and affords pure surface absorption.* Subtraction has been used for ultra-thin film to remove background instability [17] and solution-based experiments to remove absorption along the beam path [20].

The present work shows that it is possible to measure, in real time, adsorbed precursor molecules on an oxide surface during film growth by chemical vapor deposition (CVD) using a metal-coated substrate with the IR beam at grazing incidence. We perform optical calculations for the case of a very thin oxide layer on a metal substrate; these confirm that s-polarized light has a negligible sensitivity, and that the sensitivity of p-polarized light is a function of the oxide thickness and index, and of the incident angle. For grazing angles above 70°, the sensitivity is high but depends on the oxide thickness and index, i.e., the sensitivity changes dynamically during oxide growth; for angles of ~ 60-70°, the sensitivity is smaller but still usable, and is independent of the oxide thickness from 0–100 nm and independent of its refractive index from 1–2.5. We use an angle of 60° to provide constant sensitivity, and a data acquisition of 1000

scans such that the signal to noise ratio affords sub-monolayer resolution. Thus, experiments can be performed using a conventional vacuum deposition system in which the internal beam path is 10s of cm.

We apply IRRAS to analyze adsorbed precursor during the CVD of HfO_2 at 120 °C using the precursor tetrakis(dimethylamino)hafnium (TDMAH), co-reactant water, plus the growth rate inhibitor magnesium N, N-dimethylaminodiboranate, $Mg(DMADB)_2$. We previously showed that an inhibitor can be used during trench filling to suppress the oxide growth rate near to a trench opening, called the 'breadloaf' effect, and thus eliminate 'keyhole' defects due to pinch-off of the opening [21]. That work presented no evidence on, the mechanistic role of the inhibitor. Here we study a related precursor-inhibitor combination and show that the inhibitor, by competitive adsorption, acts to reduce the dynamic quantity of adsorbed TDMAH available for film growth.

6.2 Modelling

Infrared spectroscopy is based on the interaction between infrared light and the bonds of a molecule that are polarized or polarizable, such that IR absorption excites vibrational modes. An infrared spectrum is obtained by determining what fraction of the incident radiation is adsorbed at a particular photon energy (IR wavenumber), detected by the reduction of the intensity in reflectance (this work) or in transmission. When the frequency of the light matches the eigen frequency of a dipole-active oscillator, the absorption is strong, leading to a peak in the spectrum. The use of a Fourier-transform light source, and inverse Fourier transform of the signal collected by a broadband IR detector, affords parallel data collection across a wide spectral range.

We calculate the reflectance due to adsorbed molecules with fractional coverage θ on an oxide surface on a metal film (Fig. 6.1). This is a planar optical stack with thickness d_1 for adsorbed molecules, d_2 for the oxide film and the optical constants of each component, including the metal. Because these layers are thin relative to the wavelength of the incident light, interference effects are phase coherent. This problem in multilayer optics can be solved by calculating recurrence relations connecting electric and magnetic field components in each

interface using the boundary conditions of Maxwell's equations, which has been covered in [16,22,23] and is summarized as below:

$$\begin{pmatrix} B \\ C \end{pmatrix} = \left[\prod_{j=1}^{n} \begin{pmatrix} \cos\delta_j & \frac{i\sin\delta_j}{\eta_j} \\ i\eta_j \sin\delta_r & \cos\delta_j \end{pmatrix} \right] \begin{pmatrix} 1 \\ \eta_s \end{pmatrix},$$

where B and C define the optical admittance of the assembly, $Y = C/B$. Here, $n = 2$.

$$\delta_j = \frac{2\pi d_j}{\lambda}\left(\alpha_j \cos\theta_j - i\beta_j\right),$$

$$\eta_j = \frac{(n_j - ik_j)^2}{\alpha_j \cos\theta_j - i\beta_j}, \text{for p polarization,}$$

$$\eta_j = \alpha_j \cos\theta_j - i\beta_j, \text{ for s polarization,}$$

where λ is the wavelength of the incident light, n_j is the refractive index, k_j is the extinction coefficient; when the layer is a dielectric, $k_j = 0$. θ_j is the angle of incidence in the jth layer. θ_j, α_j and β_j follow the 3 equations below (Snell's law in absorbing materials):

$$\delta_j = \frac{2\pi d_j}{\lambda}\left(\alpha_j \cos\theta_j - i\beta_j\right),$$

$$\alpha_j{}^2 - \beta_j{}^2 = n_j{}^2 - k_j{}^2,$$

$$\beta_j\left(\alpha_j \cos\theta_j\right) = n_j k_j.$$

And reflectance (R) is given as:

$$R = \rho\rho^*, \rho = \frac{\eta_0 - Y}{\eta_0 + Y}.$$

Based on the above equations, we compare the sensitivity by calculating the absorption factor: $AF = (R_0 - R)/R_0$, where R is the measured reflectance and R_0 is the baseline reflectance if the film were non-absorbing (here, $k_1 = 0$); in general R_0 is not measurable, however, the reflectance of the substrate only, R_{sub}, can be measured (covered in the next

paragraph). *AF* indicates the depth of an infrared absorption band obtained from the reflection sampling system [16].

In practice, FTIR spectra usually report absorbance, defined as:

$$A = -\log\left(\frac{I}{I_0}\right) = -\log\left(\frac{R}{R_{sub}}\right),$$

where I_0 is the radiant intensity, which is received by the detector when only the substrate is present (which is termed as the background). Here, this means when $d_1 = 0$ and $d_2 = 0$ (or $n_1 = n_2 = 1\ and\ k_1 = k_2 = 0$). R_{sub} is the reflectance of the substrate. I_0 and R are the radiant intensity and reflectance when a thin film is being deposited and there are precursor molecules adsorbed on the growth surface. When $R \approx R_{sub}$, $A \approx (R_{sub} - R)/R_{sub}$. *A* and *AF* are not the same because the reflectance will be altered in the presence of films even if they are non-absorbing (R_0 vs. R_{sub}). This is demonstrated qualitatively in Fig. 6.2. Here, it is sufficient to discuss *AF* since the presence of non-absorbing films only shifts the baseline.

In the calculated result, the absorption due to adsorbed molecules depends linearly on the thickness (coverage) of layer 1 (for a fixed oxide thickness). In the real case, n_1 and k_1 are coverage-dependent [12]; thus, the surface coverage cannot be extracted from absorption without independent knowledge of the *n, k* dependence on coverage. However, the coverage is monotonically correlated with the data, so we can obtain useful information, such as whether the coverage increases or decreases upon changes in the molecular flux incident on the surface.

6.3 Experimental

The IR experimental setup is shown in Fig. 6.3. The CVD chamber is turbopumped with a base pressure of 1×10^{-7} Torr under full pumping. During experiments, the gate valve is slightly throttled to establish the partial pressures stated below. The substrate is maintained at 120 °C by thermal conduction from the substrate holder, which is heated by two embedded cartridge heaters. The temperature is measured by a K-type thermocouple attached to the sample holder.

A parallel IR beam is generated by a Michelson interferometer, focused by mirrors onto the substrate and collected by a cooled HgCdTe (MCT) detector. The beam has a divergence of

~ 10°, thus, the angle of incidence at the substrate varies from ~ 55 to 65°. A ZnSe wire grid polarizer, mounted on a motorized rotational stage, is placed in the path before the detector to select either p- or s-polarized light. The beam enters and exits the chamber through IR transparent KBr windows. The external beam path is enclosed in nitrogen-purged plastic boxes to minimize stray absorption from impurities (such as CO_2 and H_2O) in the atmosphere.

The precursor TDMAH is supplied by Sigma-Aldrich and used as received; the inhibitor $Mg(DMADB)_2$ is synthesized by G.S.G. [24]. Deionized water is used as the coreactant; the water injection rate (partial pressure) is controlled using a needle valve. All molecules are maintained at room temperature and delivered to the chamber without a carrier gas. TDMAH and water are supplied through two separate 0.4 cm i.d. stainless steel tubes aimed at the substrate to establish partial pressures of 0.70 and 0.15 mTorr, respectively. The TDMAD partial pressure is chosen so that so the surface coverage is high enough to be detected by IR absorption. The inhibitor $Mg(DMADB)_2$ is supplied through a tube of the same i.d., but aimed towards the back side of the chamber to establish an isotropic partial pressure of either 0 or 2 mTorr.

Within the pressure range used in the present experiments, $Mg(DMADB)_2$ and TDMAH do not react with water on the room-temperature reactor walls or the KBr windows. $Mg(DMADB)_2$ can also be used as a precursor used for MgO deposition at >220 °C [25,26], however, it does not react at an appreciable rate with water at 120 °C. Here it is used as a growth inhibitor.

The substrate is prepared by depositing 50-nm Au with 5-nm Cr as adhesion layer, on (1 0 0) Si using an e-beam evaporator. The substrate is loaded in the chamber and IR backgrounds are acquired in p- and s-polarizations. Finally, ~ 20 nm of HfO_2 is deposited using TDMAH and water to establish a continuous oxide surface (i.e., to avoid the changing morphology associated with initial nucleation and coalescence).

During the experiments, TDMAH and water are continuously injected to grow HfO_2, while IRRAS spectra in p- and s-polarizations are taken sequentially. The interferometer is set to acquire data at a resolution of 8 cm^{-1}; 1000 scans are averaged for each spectrum, which takes about 2.5 min to collect (5 min for a pair of spectra). Whenever a growth condition is changed, e.g., upon introduction of $Mg(DMADB)_2$, data collection begins after a 2 min waiting time in

order to allow the surface populations to reach a steady state. The steady state is confirmed by taking at least a second spectrum in succession and comparing data. To extract the absorption from the substrate surface, each s-polarized spectrum is subtracted from the one in p-polarization as explained above.

The areal density of Hf atoms is measured ex-situ by Rutherford backscattering spectrometry (RBS), and then converted to equivalent HfO_2 thickness using the bulk density for the Hf sublattice. The growth rate is determined by the equivalent film thickness divided by the growth time. Films grown by CVD at low temperature typically have a lower density than perfect crystalline materials; for example, at 200 °C the HfO_2 density is only 86 % of the bulk value [21]. Thus, the physical thickness is larger than the equivalent thickness. A film grown in the presence of $Mg(DMADB)_2$ is also analyzed by X-ray photoelectron spectroscopy (XPS) to check for possible Mg contamination.

6.4 Results and discussion

6.4.1 Calculation of sensitivity on metal substrates

A sub-monolayer of adsorbed small molecules is represented by a thin film of optical constants n_1, k_1 and thickness d_1. For an ultra-thin layer, a typical value for *n* is 1.3 [16]. The extinction coefficient k_1 is set at 0.1 to represent a moderately strong IR absorption band. The thicknesses of the layer (d_1) is set at 1 nm. We set $n_s = 7$ and $k_s = 32$ for the Au substrate. The wavelength λ is set to 4000 nm, close to the relevant characteristic IR band of TDMAH molecules studied experimentally. In fact, it is the value of λ/d_1 that determines the absorption for given values of *n* and *k*.

The thickness of the oxide film, which increases during deposition, can affect the sensitivity. Fig. 6.4a shows how the absorption factor changes with angle of incidence (θ_0) for several thicknesses of the oxide layer (d_2) for a refractive index of 2. The absorption factor (sensitivity) for p polarization is much higher than for s polarization at high angle of incidence ($\theta_0 > 60°$). The ratio of p- to s- is at least a factor of 30, and for some conditions it is a factor of 100 to 1000. We therefore neglect absorption in s-polarization. As θ_0 increases from 0° to 90°,

the absorption factor for p-polarization increases to a maximum and then drops quickly. For example, when $d_2 = 0\ nm$, the maximum occurs at 88°, where it is 6000 times larger than that at 0°. The spectra with the best SNR can be realized at this angle (for a beam of nearly zero divergence, and for a growth surface that is uniform over the extended illuminated area). However, the absorption factor at this angle, is more sensitive to the thickness of the underlying oxide layer (Fig. 6.4b). For example, it declines by 20 % when d_2 increases from 0 to 10 nm, and by 90% when d_2 is 100 nm. This makes it difficult to make quantitative comparisons between spectra collected in the early stage (when the oxide is thin) and later stage (when the oxide is thick). When θ_0 is smaller, the dependence on d_2 is less significant. At 80°, the absorption factor declines by only 40 % when d_2 increases from 0 to 100 nm. At 60°, the change is only 0.5 %. For s-polarization, the absorption factor is more sensitive to d_2 at lower angle (Fig. 6.4c), but the magnitude in s- is always negligible compared with that in p-polarization. Thus, we can improve the stability of the absorption factor at the cost of losing sensitivity by using an incident angle well below 88°; experimentally we use 60°.

The refractive index of bulk oxides (n_2) typically has a range of 1.5–2.5, however, when an oxide is very thin, the index may be lower and thickness-dependent [12]. Also, the growth conditions may affect n_2, e.g., when the physical density is below bulk [21]. Fig. 6.5a shows how the absorption changes with variation of refractive index for different angles of incidence. d_2 is set as 10 nm. For p-polarization, when θ_0 is close to 88°, the absorption factor depends on the value of n_2, especially for n_2 close to 1 (Fig. 6.5b). The absorption factor for s-polarization is low and almost independent of n_2 (Fig. 6.5c). As above, using an incident angle well below 88° minimizes the effect of n_2 on the absorption factor.

6.4.2 IR absorption from adsorbed TDMAH during CVD of HfO_2

The CVD of HfO_2 using TDMAH and water, in the absence and presence of the inhibitor $Mg(DMADB)_2$, is analyzed using IRRAS. All spectra are taken in the presence of gas-phase TDMAH and water. The substrate temperature, and the pressure ratio of TDMAH and water, are chosen to afford reaction-rate limited growth with a high surface coverage of TDMAH. Under these conditions, the growth rate is 1.6 Å/min and 0.30 Å/min in the absence and presence of

$Mg(DMADB)_2$, respectively. A much slower growth rate than in typical CVD experiments also affords more time for data acquisition, thus a higher SNR.

Fig. 6.6 shows the spectra in p- and s-polarization from 850 to 4000 cm^{-1}, in the absence and presence of $Mg(DMADB)_2$. Multiple peaks from TDMAH can be detected both in p- and s-polarization (spectrum 1 and 2 in Fig. 6.6a and 6.6b, respectively). Among them, TDMAH has two characteristic peaks [27] at 2781 cm^{-1}, which is the Bohlmann-type band of C-H stretching, and 945 cm^{-1}, which is the Hf-N-C stretching (indicated by two red arrows in Fig. 6.6 and Fig. 6.7). In reference [27], reaction of a pre-adsorbed TDMAH with water leads to loss of dimethylamine (DMA) ligands and reduced peak intensity. Molecular DMA also has the Bohlmann-type band but at a different position (2810 cm^{-1}), which was not detected. We therefore rely on the peaks at 2781 cm^{-1} and 945 cm^{-1} to show changes in the dynamic surface coverage of TDMAH. Other peaks are less useful because byproducts or other molecules may share the same positions (e.g., $Mg(DMADB)_2$ has a CH_3 rocking peak at ~1450 cm^{-1}).

The heights of these two peaks (2781 and 945 cm^{-1}) increase slowly with time (lines 1, 2, 7 and 8 in Fig. 6.6a and 6.6c). As we describe below, the growth surface is in steady state and adsorbed precursor coverage does not change with time (lines 1, 2, 7 and 8 in Fig. 6.7). Thus, absorption from the IR windows must be increasing gradually, presumably by molecular condensation. However, this process is slow such that the difference is not significant when comparing two spectra collected within a few minutes, i.e., the signal from windows and gas phase are stable enough to allow subtraction of each spectrum in s-polarization from that in p-polarization, if we measure the pair sequentially.

Introduction of $Mg(DMADB)_2$ adds a few more peaks and the height of some peaks increase with time (such as the one close to 1320 cm^{-1} for lines 3, 4 and 5 in Fig. 6.6a and 6.6b,). The peak at ~1320 cm^{-1} is negligible when s- and p- spectra are subtracted (Fig. 6.7c), indicating it is not from surface absorption. We attribute this change to condensation of $Mg(DMADB)_2$ on the room-temperature windows. When $Mg(DMADB)_2$ stops flowing, many peaks are still visible both in p- and s-polarization, but with slightly lower intensity. The twin peaks that exist in all spectra, from 2200 to 2400 cm^{-1}, are attributed to a variation in the residual concentration of CO_2 in the nitrogen-purged external beam path.

In Fig. 6.7, the difference spectra are arranged according to time from bottom to top. Before $Mg(DMADB)_2$ molecules are introduced (spectrum 1 and 2), there are only a few peaks: C-H stretching from 2750 to 2900 cm^{-1}, CH_3 bending at ~1450 cm^{-1} and H-C-N stretching at ~950 cm^{-1}. The peak at ~900 cm^{-1} is unassigned yet. It appears to increase with time but is not affected by $Mg(DMADB)_2$. Also, there is no sign of DMA adsorption on the surface. Introduction of $Mg(DMADB)_2$ adds two peaks from 2900 to 3000 cm^{-1} (C-H stretching), a broad peak from 2000 to 2500 cm^{-1} (B-H stretching), a peak at ~1140 cm^{-1} and a peak at ~ 1020 cm^{-1}. These peaks are only slightly reduced when $Mg(DMADB)_2$ flow is turned off, *signifying incorporation of $Mg(DMADB)_2$ products in the film*. However, Mg atoms are barely detectable by XPS (Fig. 6.8) in another sample grown for 50 min (1.5 nm in thickness) under otherwise identical conditions in the presence of $Mg(DMADB)_2$.

The addition of $Mg(DMADB)_2$ also affects existing peaks: the height of the peak at ~1450 cm^{-1} is increased and remains unchanged when $Mg(DMADB)_2$ is removed, indicating extra hydrocarbon on the surface or incorporated into the film. Fig. 6.9 displays the height of the C-H stretching peaks (2781 cm^{-1} and 945 cm^{-1}) for all spectra in Fig. 6.7. In the absence of $Mg(DMADB)_2$, these heights do not change with film thickness. Considering that the optical sensitivity is constant in this range, we conclude that TDMAH molecules are not incorporated into the film (they are adsorbed on the surface). All peaks have only modest SNR; however, it is clear that *the heights of peaks for TDMAH are reduced by approximately 50% with an introduction of $Mg(DMADB)_2$, which correlates with a drop in the HfO_2 growth rate by a factor of > 5*. As noted above, the peak heights may be non-linear in surface coverage.

It takes time for the surface coverage to stabilize when $Mg(DMADB)_2$ flow is turned on or off (the first spectra after a change in $Mg(DMADB)_2$ flow does not represent steady-state, line 3 and 6 in Fig. 6.7). However, at 2 mTorr of $Mg(DMADB)_2$ pressure, the time required to deliver 1 Langmuir of molecules to the surface is ~1/2000 s. And thus, the observed delay reveals that adsorbates ($Hf(N(CH_3)_2)_x$) are slow to desorb from or to react on the surface.

A likely possibility for growth inhibition is that partially-decomposed $Mg(DMADB)_2$ covers part of the oxide surface and blocks adsorption of TDMAH. The strength of this effect (that the growth rate falls by a factor of > 5) may imply the importance of effects beyond Langmuirian site-blocking; potential mechanisms include, but are not limited to, strong steric

hindrance by the inhibitor, blocking of specific adsorption sites, or a higher-order dependence of precursor reaction on the density of available sites. With the present sensitivity, it is not possible to determine whether $Mg(DMADB)_2$ (or its dissociation products) reacts directly with TDMAH to form an intermediate with lower reactivity. We note that formation of low-reactivity surface intermediates is thought to be very important in area-selective deposition by CVD (Chapter 2).

6.4.3 Limitations and future work

We discuss limitations and possible methods to improve IRRAS for application in CVD. The major limitation in our setup is a lack of sensitivity, resulting in a low SNR. To improve the SNR, with no change in sensitivity, a longer measurement time is required. That would, however, compromise the temporal resolution. A second issue is the stability of the system between data acquisition in p- and s-polarization. Because data reduction requires the subtraction of relatively large signals, minute instabilities can reduce the SNR. For example, we suspect that the time scale for molecular adsorption and desorption on the IR windows affects the data. The stability problem can be mitigated using polarization-modulated FTIR such that a pair of p- and s-polarized scans can be acquired in less than a second [17-19]. And of course, the SNR can be improved using a lower resolution.

Low sensitivity ultimately limits the application when the surface coverage of an adsorbate is small. One solution is to employ a higher angle of incidence (such as 80°) to improve the sensitivity. The sensitivity will then have a dependence on the underlying oxide thickness; however, this effect will be partially compensated by the shorter time required to achieve a desired SNR. Of course, there is no problem with changing sensitivity if molecular adsorption occurs directly on a metal surface; this would be the case for studies of metal CVD when the metal is thick enough to be optically opaque. A second possible solution is to use a multi-reflection setup, such as one in which two substrates face each other in [28]. A third solution is to use a multiple internal reflection substrate [29]. However, the latter affords sensitivity in both p- and s-polarizations on the surface, so it would also be necessary to suppress absorptions from molecules in the beam path and on the windows; this is possible, but non-trivial, to implement experimentally.

6.5 Conclusion

We use IRRAS to measure, in real time, the sub-monolayer surface coverage of molecular intermediates during CVD of oxides on a metal-coated planar substrate. To optimize the experiment, we first calculate the optical sensitivity as a function of the incident angle and substrate configuration. Use of a metal-coated substrate at high angle of incidence affords enhanced sensitivity in p-polarization, and suppressed sensitivity in s-polarization. The unwanted adsorption due to precursor in the gas phase beam path and adsorbed on the IR windows is cancelled out by subtraction of the p and s spectra. The sensitivity for p polarization is predicted to increase with glancing angle to a maximum at 88°, then to drop quickly. However, for angles above ~ 70° the sensitivity is also a function of the thickness and refractive index of the underlying oxide layer. Here, a 60° angle of incidence is used so that the sensitivity remains constant for oxide thicknesses at least below 100 nm.

We investigate CVD of HfO_2 from TDMAH and water with the addition of $Mg(DMADB)_2$ as a molecular growth inhibitor. We show that the reduction in HfO_2 growth rate upon addition of the inhibitor corresponds to a drop in the surface coverage of TDMAH molecules, i.e., we find that the microscopic role of the inhibitor is to reduce surface coverage of TDMAH.

6.6 Figures

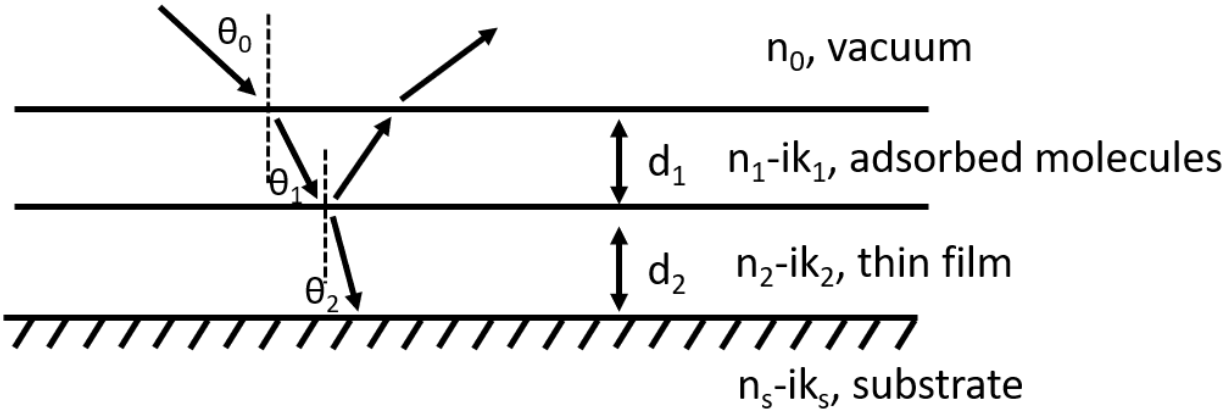

Figure 6.1. Schematic representation of two coherent layers on a semi-infinite substrate.

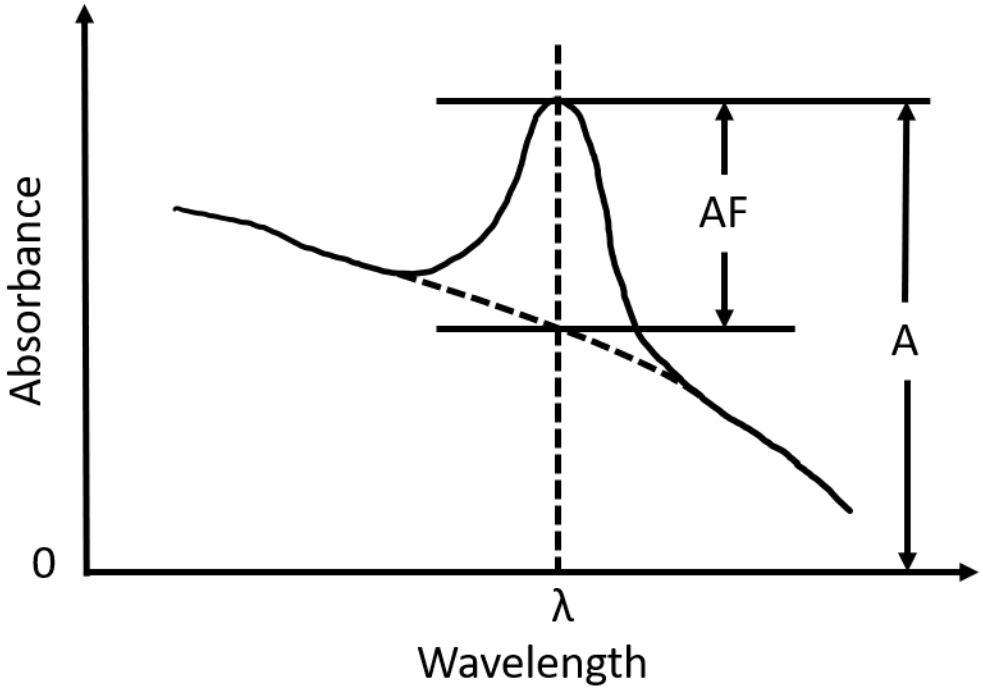

Figure 6.2. Schematic representation of absorption factor ($AF = (R_0 - R)/R_0$) and absorption $A = (R_{sub} - R)/R_{sub}$. See text for details.

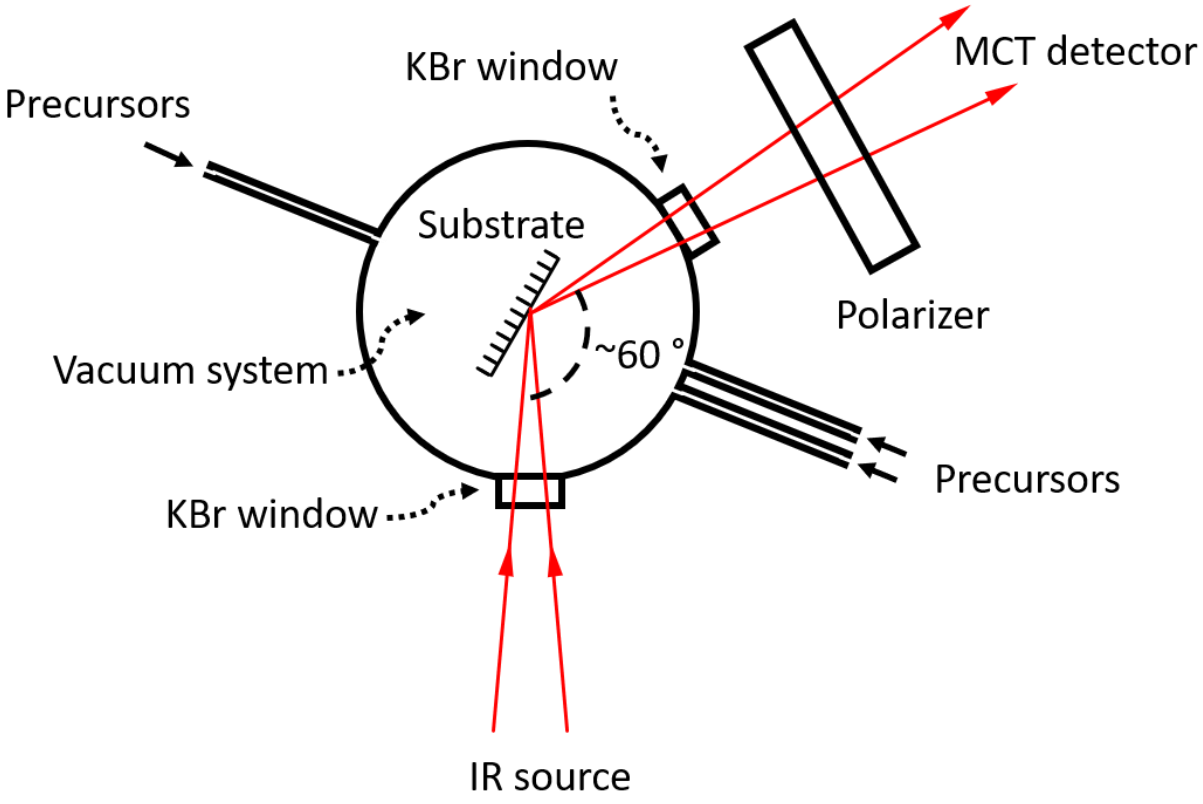

Figure 6.3. Schematic representation of the infrared reflection absorption spectroscopy and CVD system.

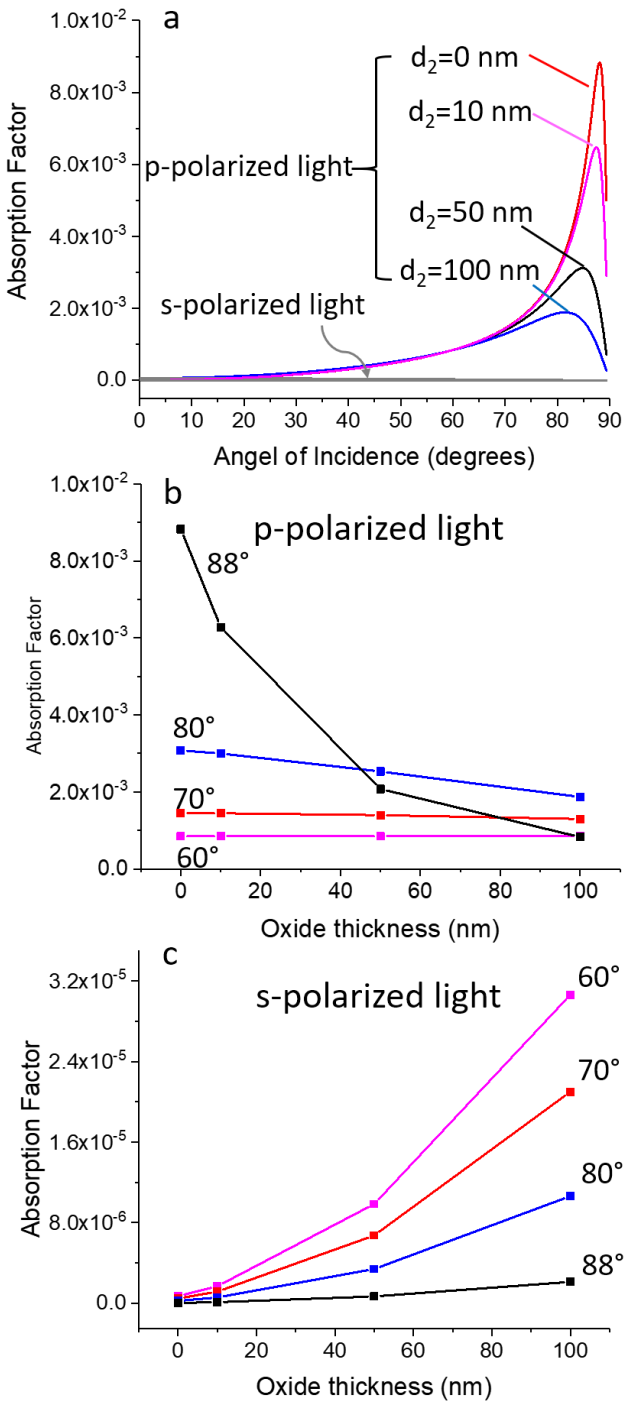

Figure 6.4. Calculated absorption factor for p and s polarizations in the molecular layer on a metal substrate covered by an oxide layer as a function of incidence angle for variation of the thickness of the oxide layer (a); as a function of thickness of the oxide layer for variation of incidence angle in p-polarization (b) and s-polarization (c).

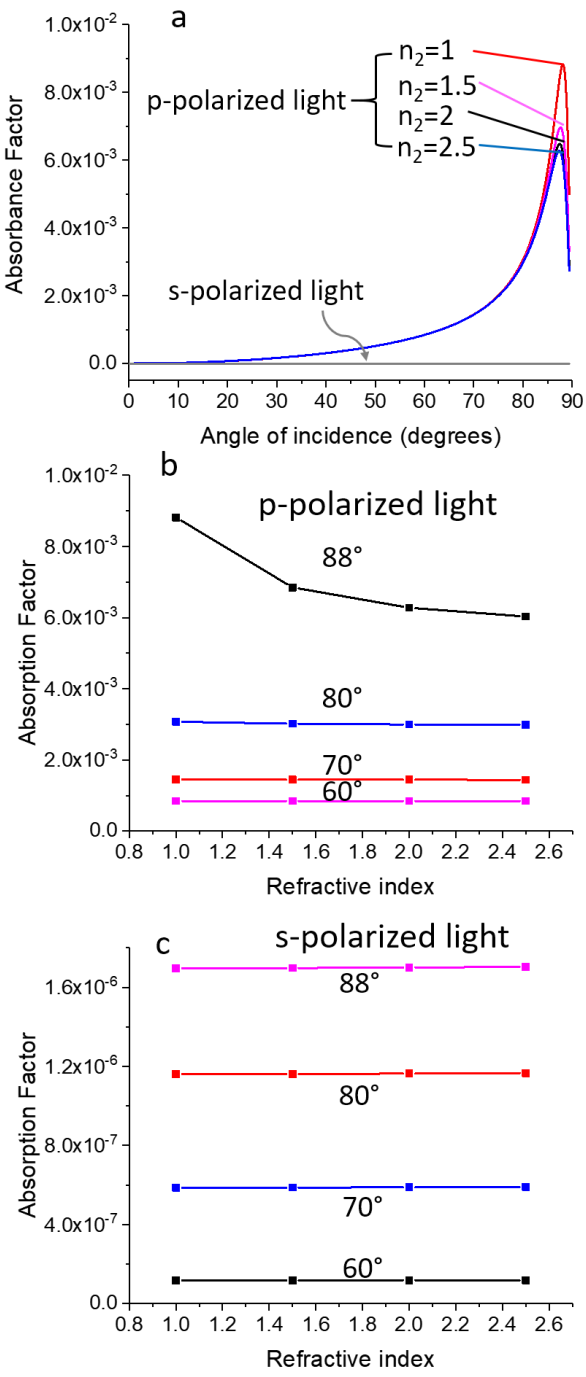

Figure 6.5. Calculated absorption factor for p and s polarizations in the molecular layer on a metal substrate covered by an oxide layer as a function of incidence angle for variation of the refractive index of the oxide layer (a); as a function of refractive index of the oxide layer for variation of incidence angle in p-polarization (b) and s-polarization (c).

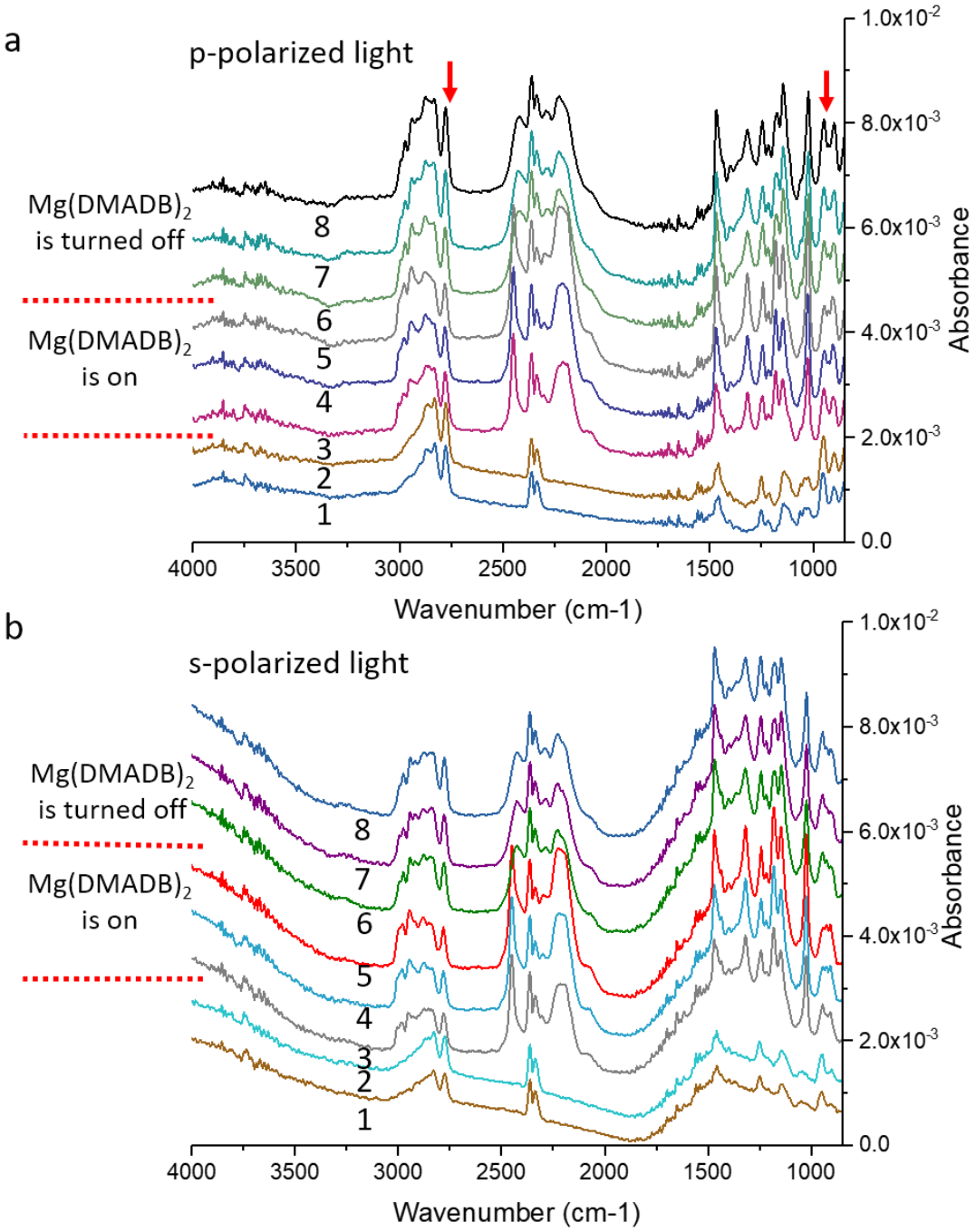

Figure 6.6. IR spectra in p (a) and s (b) polarization for CVD of HfO_2 from TDMAH and water, in the absence and presence of $Mg(DMADB)_2$. Spectra are arranged according to time from 1 to 8. $Mg(DMADB)_2$ is introduced after spectrum 2 and turned off after spectrum 5. Each spectrum in s is collected right after spectrum in p with the same number. Red arrows indicate positions of characteristic peaks for TDMAH at wavenumbers 2781 cm^{-1} and 945 cm^{-1}. In Fig. 6.7, subtraction is used to extract the signal from surface adsorbates. See text for details.

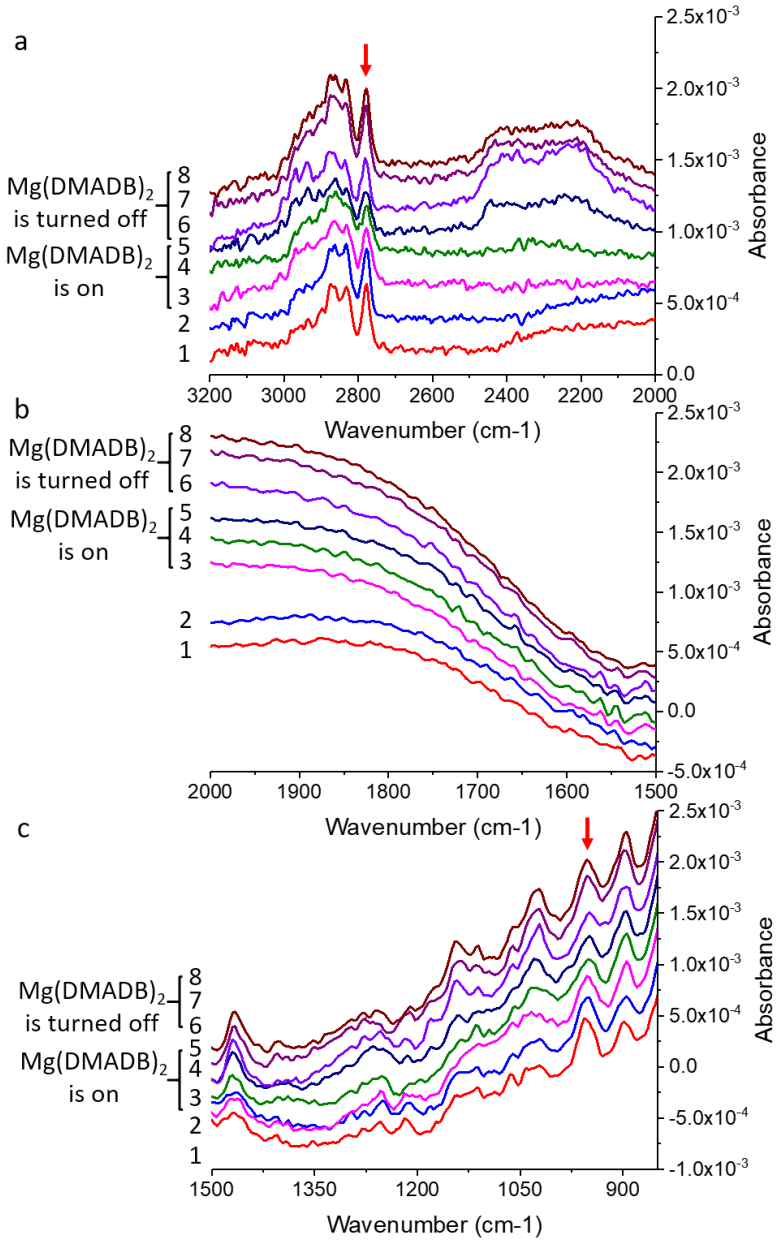

Figure 6.7. IR spectra absorption from substrate by subtracting spectra in s polarization from that in p polarization, for CVD of HfO_2 from TDMAH and water, in the absence and presence of $Mg(DMADB)_2$. Spectra are arranged according to time from 1 to 8. $Mg(DMADB)_2$ is introduced after spectrum 2 and turned off after spectrum 5. Red angles indicate positions of characteristic peaks for TDMAH. The subtle height changes are shown in Fig. 6.9. See text for details.

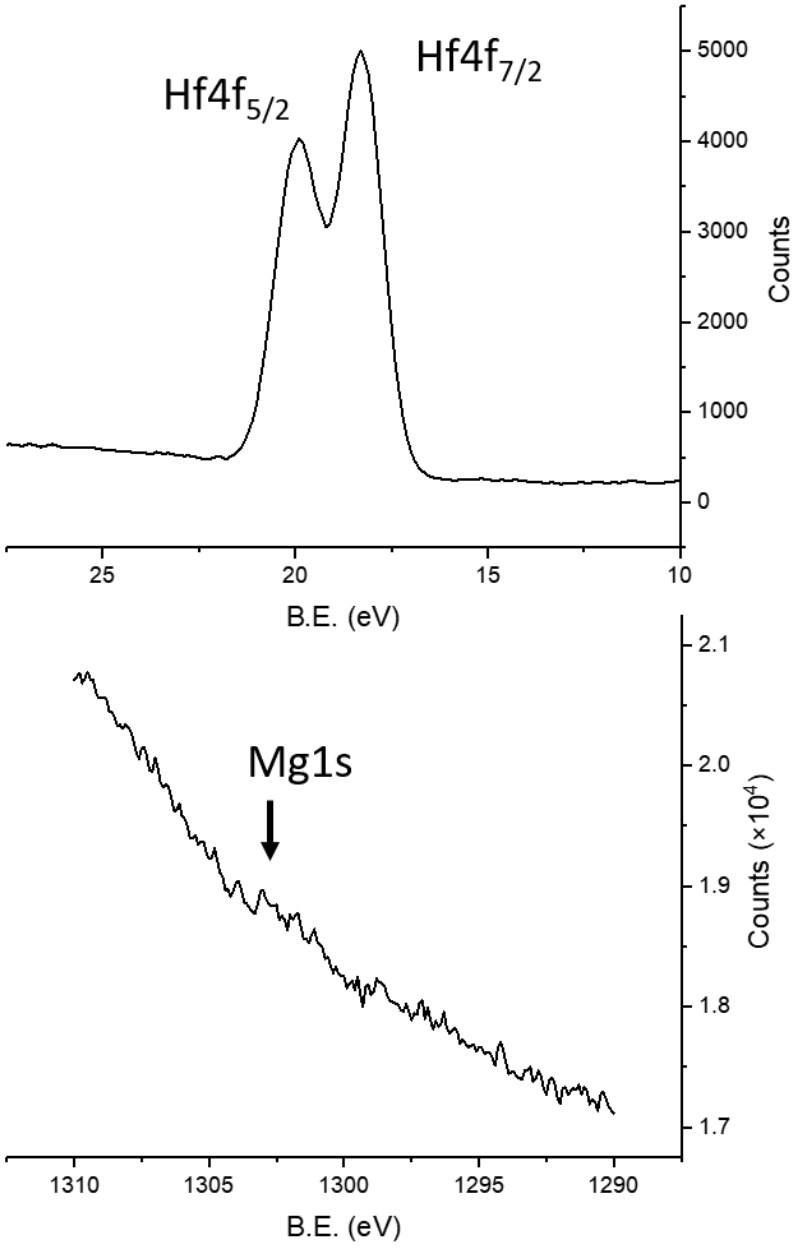

Figure 6.8. XPS Hf (4f) and Mg (1s) peaks for a HfO_2 films grown in the presence of $Mg(DMADB)_2$. The total equivalent thickness is 1.5 nm.

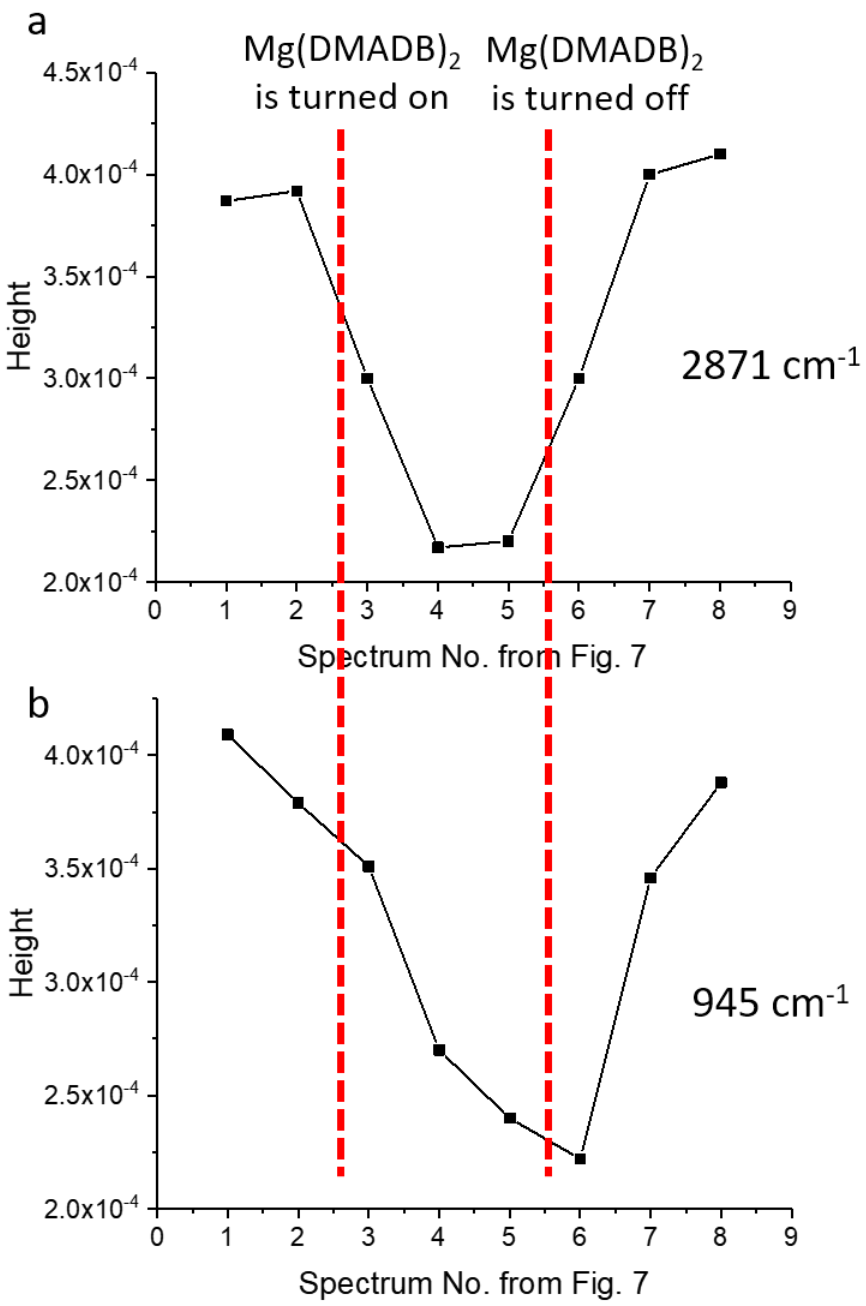

Figure 6.9. The heights of absorption peaks at 2781 cm^{-1} and 945 cm^{-1} for all spectra from Fig. 6.7.

6.7 References

1. S. Jayaraman, Y. Yang, D. Y. Kim, G. S. Girolami, and J. R. Abelson, "Hafnium diboride thin films by chemical vapor deposition from a single source precursor," *Journal of Vacuum Science & Technology A* **23,** 1619-25 (2005).

2. W. B. Wang, N. N. Chang, T. A. Codding, G. S. Girolami, and J. R. Abelson, "Superconformal chemical vapor deposition of thin films in deep features," *Journal of Vacuum Science & Technology A* **32,** 051512 (2014).

3. T. K. Talukdar, W. B. Wang, G. S. Girolami, and J. R. Abelson, "Superconformal coating and filling of deep trenches by chemical vapor deposition with forward-directed fluxes," *Journal of Vacuum Science & Technology A* **36,** 051513 (2018).

4. E. Mohimi, Z. V. Zhang, J. L. Mallek, S. Liu, B. B. Trinh, P. P. Shetty, G. S. Girolami, and J. R. Abelson, "Low temperature chemical vapor deposition of superconducting vanadium nitride thin films," *Journal of Vacuum Science & Technology A* **37,** 031509 (2019).

5. N. Kumar, A. Yanguas-Gil, S. R. Daly, G. S. Girolami, and J. R. Abelson, "Growth inhibition to enhance conformal coverage in thin film chemical vapor deposition," *Journal of the American Chemical Society* **130,** 17660-1 (2008).

6. W. B. Wang and J. R. Abelson, "Filling high aspect ratio trenches by superconformal chemical vapor deposition: Predictive modeling and experiment," *Journal of Applied Physics* **116,** 194508 (2014).

7. Y. Wang, M. Dai, M. T. Ho, L. S. Wielunski, and Y. J. Chabal, "Infrared characterization of hafnium oxide grown by atomic layer deposition using ozone as the oxygen precursor," *Applied Physics Letters* **90,** 022906 (2007).

8. M. J. Kelly, J. H. Han, C. B. Musgrave, and G. N. Parsons, "In-situ infrared spectroscopy and density functional theory modeling of hafnium alkylamine adsorption on si−oh and si−h surfaces," *Chemistry of Materials* **17,** 5305-14 (2005).

9. D. N. Goldstein, J. A. McCormick, and S. M. George, "Al2o3 atomic layer deposition with trimethylaluminum and ozone studied by in situ transmission ftir spectroscopy and quadrupole mass spectrometry," *The Journal of Physical Chemistry C* **112,** 19530-9 (2008).

10. S.-W. Kang, Y.-J. Park, Y.-S. Kim, Y.-H. Shin, and J.-Y. Yun, "Real-time evaluation of aluminum borohydride trimethylamine for aluminum chemical vapor deposition," *Journal of The Electrochemical Society* **156,** H333-H9 (2009).

11. V. Hopfe, D. W. Sheel, C. I. M. A. Spee, R. Tell, P. Martin, A. Beil, M. Pemble, R. Weiss, U. Vogt, and W. Graehlert, "In-situ monitoring for cvd processes," *Thin Solid Films* **442,** 60-5 (2003).

12. M. Katiyar and J. R. Abelson, "Methods to enhance absorption signals in infrared reflectance spectroscopy: A comparison using optical simulations," *Journal of Vacuum Science & Technology A* **13,** 2005-12 (1995).

13. N. Maley, I. Szafranek, L. Mandrell, M. Katiyar, J. R. Abelson, and J. A. Thornton, "Infrared relfectance spectroscopy of very thin films of a-sih," *Journal of Non-Crystalline Solids* **114,** 163-5 (1989).

14. M. Katiyar, G. F. Feng, Y. H. Yang, J. R. Abelson, and N. Maley, "Hydrogen incorporation in the early stages of hydrogenated amorphous silicon deposition evaluated by real time infrared reflectance spectroscopy," *Applied Physics Letters* **63,** 461-3 (1993).

15. M. Katiyar, Y. H. Yang, and J. R. Abelson, "Hydrogen-surface reactions during the growth of hydrogenated amorphous silicon by reactive magnetron sputtering: A real time kinetic study by in situ infrared absorption," *Journal of Applied Physics* **77,** 6247-56 (1995).

16. R. G. Greenler, "Infrared study of adsorbed molecules on metal surfaces by reflection techniques," *Journal of Chemical Physics* **44,** 310-& (1966).

17. T. Buffeteau, B. Desbat, and J. Turlet, "Polarization modulation ft-ir spectroscopy of surfaces and ultra-thin films: Experimental procedure and quantitative analysis," *Applied Spectroscopy* **45,** 380-9 (1991).

18. D. Blaudez, T. Buffeteau, J. C. Cornut, B. Desbat, N. Escafre, M. Pezolet, and J. M. Turlet, "Polarization modulation ftir spectroscopy at the air-water interface," *Thin Solid Films* **242,** 146-50 (1994).

19. D. Blaudez, T. Buffeteau, B. Desbat, M. Orrit, and J. M. Turlet, "Characterization of langmuir-blodgett monolayers using polarization modulated ftir spectroscopy," *Thin Solid Films* **210-211,** 648-51 (1992).

20. K. Kunimatsu, H. Seki, W. G. Golden, J. G. Gordon, and M. R. Philpott, "Electrode/electrolyte interphase study using polarization modulated ftir reflection-absorption spectroscopy," *Surf Sci* **158,** 596-608 (1985).

21. T. K. Talukdar, G. S. Girolami, and J. R. Abelson, "Seamless fill of deep trenches by chemical vapor deposition: Use of a molecular growth inhibitor to eliminate pinch-off," *Journal of Vacuum Science & Technology A* **37,** 021509 (2019).

22. O. S. Heavens, *Optical properties of thin solid films* (Courier Corporation, 1991). [DOI:

23. Y. J. Chabal, "Surface infrared spectroscopy," *Surf Sci Rep* **8,** 211-357 (1988).

24. D. Y. Kim and G. S. Girolami, "Highly volatile magnesium complexes with the aminodiboranate anion, a new chelating borohydride. Synthesis and characterization of mg(h3bnme2bh3)2 and related compounds," *Inorg Chem* **49,** 4942-8 (2010).

25. T. K. Talukdar, S. Liu, Z. Zhang, F. Harwath, G. S. Girolami, and J. R. Abelson, "Conformal mgo film grown at high rate at low temperature by forward-directed chemical vapor deposition," *Journal of Vacuum Science & Technology A* **36,** 051504 (2018).

26. W. B. Wang, Y. Yang, A. Yanguas-Gil, N. N. Chang, G. S. Girolami, and J. R. Abelson, "Highly conformal magnesium oxide thin films by low-temperature chemical vapor deposition from mg(h3bnme2bh3)2 and water," *Applied Physics Letters* **102,** 101605 (2013).

27. K. Li, S. Li, N. Li, D. A. Dixon, and T. M. Klein, "Tetrakis(dimethylamido)hafnium adsorption and reaction on hydrogen terminated si(100) surfaces," *The Journal of Physical Chemistry C* **114,** 14061-75 (2010).

28. R. G. Greenler, "Design of a reflection–absorption experiment for studying the ir spectrum of molecules adsorbed on a metal surface," *Journal of Vacuum Science and Technology* **12,** 1410-7 (1975).

29. C. L. Platt, N. Li, K. Li, and T. M. Klein, "Atomic layer deposition of hfo2: Growth initiation study on metallic underlayers," *Thin Solid Films* **518,** 4081-6 (2010).

CHAPTER 7

SUPERCONFORMAL DEPOSITION BY CONSUMABLE-INHIBITOR METHOD AND TWO-PRECURSOR METHOD: EXPERIMENT AND MODELING

7.1 Introduction

Void-free filling of recessed features, such as trenches and vias, is to fabricate integrated circuits, such as interconnects [1] and shallow trench isolation [2]. Chemical vapor deposition (CVD) and atomic layer deposition (ALD) can afford highly conformal coating by operating in a regime that is kinetically limited by the surface reaction rate [3,4]. However, even a perfectly conformal coating process cannot afford void-free filling when the feature has parallel sidewalls: as film builds up on the walls the aspect ratio (AR) increases asymptotically to infinity, and the decrease in precursor diffusivity degrades the conformality, which leaves a seam along the centerline [5]. This seam leads to a degradation of performance, including thermal and mechanical properties [6,7], electrical conductivity [8-10] and non-uniform etch rate [5].

Superconformal deposition [5,11,12] – in which the deposition rate at the bottom of the structure is faster than at the top – creates a V-shaped taper that favors seamless filling in a trench [13]. We previously demonstrated three distinct kinetic processes that afford superconformal growth: **1**) a competition for surface adsorption sites between precursor and water co-reactant in combination with a large ratio in molecular diffusivity between the high-mass precursor and low-mass water [11]; **2**) ballistic transport of the rate-limiting reactant to the bottom of the feature [5]; and **3**) a suppression of the growth rate near to the trench opening using a consumable inhibitor [14]. All three methods enjoy a regime of applicability but have particular limitations: **1** requires the use of a co-reactant, competitive adsorption, the absence of gas phase or wall reactions, and a large mass difference between the precursor and co-reactant; relatively few pairs of molecules meet all of these requirements. **2** requires a special design for precursor injection to obtain a uniformly distributed forward-directed flux, which is a difficult engineering challenge. **3** works for single-source CVD and does not have uniformity issues,

however, the films may be contaminated by elements contained in the inhibitor. For example, HfB_2 films grown with atomic nitrogen as the inhibitor contain 15 at. % nitrogen [14]. Thus, it would be very attractive to develop a new superconformal growth process that avoids the above issues.

First, we demonstrate a superconformal CVD process for cobalt using the single source $Co_2(CO)_8$ precursor with the aid of a consumable inhibitor [5], tetrakis(dimethylamino)vanadium (TDMAV). We focus on cobalt because it is of strong interest for back-end metallization and as a transistor contact in microelectronics [1,15]. Interestingly, neither of these molecules, when used alone, affords a conformal deposit. For $Co_2(CO)_8$, the step coverage improves in the limit of very low growth temperature (60 °C) and high precursor pressure (> 30 mTorr), but these conditions are not very practical [16]. TDMAV has been used as a surface pretreatment to enhance nucleation [17,18] and as a precursor for the CVD and ALD of vanadium nitride [19] and vanadium oxide [20] at temperatures > 175 °C. Kinetic analyses in these studies indicate that TDMAV has a very high sticking probability; as discussed below, this property enables the present approach. However, the resulting Co films are alloyed with V and contaminated with ligand elements.

Second, we propose a new method for superconformal growth using two precursors that have very different rates of adsorption and reaction. One precursor has strong adsorption but a slow reaction rate; it dominates the kinetics near to the trench opening, which leads to a low growth rate. But as this precursor is depleted by wall reaction, the growth rate due to the second precursor increases with depth in the trench. Diffusion-reaction model calculations show that, even though growth from each precursor individually is sub-conformal, a broad range of (P,T) conditions exists for which the growth rate in the trench is superconformal. This approach does not require that the two species have a different molecular diffusivity or a forward-directed flux. In the special case where both precursors deposit the same type of film, it should be possible to deposit impurity-free films of constant composition.

7.2 Experimental

CVD experiments are performed in a cold wall high vacuum chamber of high vacuum construction described elsewhere [21,22]; the base pressure is 1×10^{-7} Torr, most of which is H_2. The pressure in the chamber background is measured by MKS Baratron® capacitance manometer (390HA-00001). Growth rate and composition measurements are done on 1.5 ×1.5 cm Au or Si substrates, respectively. Si substrates are cut from Si wafers used as received without further cleaning and Au substrates are obtained by depositing 50-nm Au on Si by e-beam evaporation. Samples for resistivity measurement is prepared on thermal SiO_2 substrates. For conformal coating studies, lithographically defined microtrenches with SiN_x walls are used. Substrates are radiatively heated, as measured by a K-type thermocouple attached to the front of the sample holder.

The precursor $Co_2(CO)_8$ is sold from as a mixture with 1-10 % hexane to improve shelf life; the hexane is removed by evacuation before the first use of the precursor. The hexane-free precursor is placed in a glass container, which is immersed in a water bath and delivered to the chamber without a carrier gas through a 0.4 cm i.d. stainless steel tube aimed at the substrate to sustain a chamber pressure of 0.005 to 0.03 mTorr. Hexacarbonyl(3,3-dimethyl-1-butyne)dicobalt (CCTBA) and TDMAV molecules are supplied by Sigma-Aldrich and used as received. They are maintained in separate metal containers and delivered to the chamber through separate tubes aimed at the substrate, at room temperature without carrier gas. The pressure of these molecules in the chamber is below the detection limit ($< 1 \times 10^{-6}$ Torr) of the capacitance manometer.

The atomic composition is measured ex-situ by Rutherford backscattering spectroscopy (RBS); Film thickness is measured by scanning electron microscopy (SEM and the growth rate is obtained from SEM film thickness divided by growth time. Resistivity is measured by the method of four-point probe method.

7.3 Results and discussion

7.3.1 Film conformality from $Co_2(CO)_8$ precursor

$Co_2(CO)_8$ is reported [18,23,24] to deposit Co films at a temperature range of 60 to 350 °C. Films deposited at lower temperature (< 100 °C) have little carbon contamination and good electrical properties. At elevated temperature, carbon exists in the films due to decomposition of CO on cobalt metal surface. Growth from Co_2CO_8 typically has bad conformality due to the high reactivity (sticking probability) of the molecule. Fig. 7.1a shows the growth rate at 70 °C vs. $Co_2(CO)_8$ pressure from 0.005 to 0.030 mTorr. At these conditions, the growth is transport limited, indicated by a linear correlation between growth rate and pressure. The sticking probability β on the planar substrate is approximately 9 %. This is high in terms of conformality: in trenches the consumption of precursor on the sidewalls leads to large pressure drop and a relatively poor step coverage, SC ≈ 64 % (Fig. 7.1b). The SC calculated from a diffusion-reaction model [13,14], assuming 9 % reaction probability, matches relatively well (SC ≈ 70 %) with the experimental result (Fig. 7.1c). This model neglects the directional flux that travel directly to the trench bottom, which may slightly underestimate the number of molecules in the depth of a trench.

In a vertical trench with precursor, the equation is:

$$\frac{D_k w}{kT}\frac{d^2P}{dz^2} = R = \beta\frac{P}{\sqrt{2\pi mkT}},$$

where w is the width of the trench, P is the partial pressure of each molecule, R is consumption rate. $D_k = \frac{w^2}{3(\frac{w}{\bar{v}}+\tau_0)}$ is Knudsen diffusivity, where $\bar{v} = \sqrt{\frac{8k_BT}{\pi m}}$ is arithmetic mean speed of the molecule, τ_0 counts for residence time of the molecules on surface. Here we set $\tau_0 = 0$ for simplification.

7.3.2 Film conformality from $Co_2(CO)_8$ in the presence of a consumable inhibitor

Here, we test TDMAV as a consumable inhibitor. When TDMAV is absent, the growth rate is ~ 2.7 nm/min at a $Co_2(CO)_8$ pressure of 0.03 mTorr and substrate temperature of 70 °C.

When TDMAV is present, the growth rate is reduced to ~ 0.25 nm/min. TDMAV pressure is much lower than that of $Co_2(CO)_8$ by a factor of > 30. This means TDMAV has a very strong inhibition effect. TDMAV is consumed in the process because vanadium is incorporated into the film, evidenced by the RBS spectrum (Fig. 7.2). The cobalt film contains ~ 6 at. % of vanadium. The film presumably also contains carbon and nitrogen, which are from TDMAV. The electrical resistivity is increased significantly from 11 ~ 15 μΩ·cm [18] to 125 μΩ·cm.

For conformal coating study, a cobalt film is grown on a trench substrate at otherwise identical condition in the presence of TDMAV for a total growth time of 80 min. Fig. 7.3 gives the cross-section images of the trenches with different ARs. For a trench with initial AR of 3, the growth is superconformal: the film thickness is 21 nm at the top and 40 nm in the bottom of the trench. The AR now becomes ~ 6. Initially the angle between the side wall and substrate normal is 2° and increases to 4° after 80-min growth. According to the theory from [13], 4° is sufficient for defect-filling even by a conformal process. For a trench with initial AR of 7, the growth is quite conformal but not superconformal, with a bread-loaf profile at the trench opening that may pinch-off if growth continues. When a trench with small AR (Fig. 7.3c), the growth is very conformal. To determine whether superconformal growth is attributed to forward-directed flux [5], a substrate is tilted so that precursor and inhibitor fluxes are 20° off the surface normal. The thickness is uniform on the vertical sidewall and parallel surface (Fig. 7.4). If the growth rate is affected by forward-directed flux, the film is thinner on surfaces that are shadowed [5].

Diffusion-reaction model is applied to describe the kinetics. In a vertical trench with precursor and growth inhibitor, the equations describing the kinetics are summarized as below:

$$\frac{D_{k,pre}w}{kT}\frac{d^2P_{pre}}{dz^2} = R_{pre},$$

$$\frac{D_{k,in}w}{kT}\frac{d^2P_{in}}{dz^2} = R_{in},$$

where subscript “pre” and “in” denote precursor and inhibitor, respectively.

The calculation is also based on the following assumptions and approximations:

1. The fractional coverage of inhibitor and precursor on the growth surface can be described by first order Langmuirian adsorption equilibria, and the reaction rate of precursor is proportional to its coverage on the surface: $R_{pre} \propto \theta_{pre} = \frac{K_{pre} \times P_{pre}}{1+K_{pre} \times P_{pre}+K_{in} \times P_{in}}$, where θ_{pre} is surface coverage, K_{pre} and K_{in} are adsorption-desorption equilibrium constants of precursor and inhibitor, P_{pre} and P_{in} are pressures of precursor and inhibitor, respectively.

In the absence of the inhibitor, the growth rate is observed to be linear with $Co_2(CO)_8$ pressure (Fig. 7.1 a). This implies that the term $K_{pre} \times P_{pre}$ is small; we therefore ignore it in denominator. Let $R_{pre,0}$ be the growth rate in the absence of the inhibitor: $R_{pre,0} \propto \theta = \frac{K_{pre} \times P_{pre}}{1+K_{pre} \times P_{pre}} \approx K_{pre} \times P_{pre}$, then $R_{pre} \approx \frac{R_{pre,0}}{1+K_{in} \times P_{in}}$. From the experimental results, $R_{pre,0}$ is 4.1×10^{18}/s·m^2, calculated from a growth rate of 2.7 nm/min and R_{pre} is 3.8×10^{17} /s·m^2, when calculated from a growth rate of 0.25 nm/min; thus $K_{in} \times P_{in} = 9.8$.

2. The reaction (consumption) rate for the growth inhibitor follows analogous kinetics such that: $R_{in} = k_{in}^r \frac{K_{in} \times P_{in}}{1+K_{in} \times P_{in}}$, where k_{in}^r is surface reaction rate constant of the adsorbed inhibitor. R_{in} near to the trench opening can be approximated from the V concentration (6 at. %) in the film on a planar substrate, which is ~ 2.9×10^{16} /s·m^2. Then k_{in}^r is derived considering $K_{in} \times P_{in} = 9.8$. In fact, this assumption is still under debate: the reference [14] suggests $R_{in} \propto \frac{K_{in} \times P_{in}}{1+K_{in} \times P_{in}}$ while reference [25] uses $R_{in} \propto P_{in}$. Also, none of the study considers the dependence of R_{in} on R_{pre}. Inhibitors may not lose to the surface when there is no film growth, indicating $R_{in} = 0$ when R_{pre} =0. Chemical interaction between inhibitors and precursors are not considered too. These are a subject of future work.

An important kinetic consideration is the role of K_{in} vs. the role of P_{in}. We run a series of simulations as a function of P_{in}, varying K_{in} inversely in order to keep the product $K_{in} \times P_{in}^0$ constant; the latter maintains a reaction rate R_{in} that corresponds to the observed V incorporation of 6 at. %. Then, by comparing the growth rate profiles in the trench with experimental data, we can approximately deduce the chamber pressure and sticking probability of TDMAV ($\beta_{in} = \frac{R_{in}}{F_{in}}$ and $F_{in} = \frac{P}{\sqrt{2\pi mkT}}$).

Fig. 7.5a, d, g show the calculated growth rate profiles in trenches (AR = 1, 5, 10, 20) with various values of P_{in} and sticking probability. The simulation in Fig. 7.5d is a close match to the experimental results of Fig. 7.3a, which indicate a TDMAV pressure of ~10^{-7} Torr and a sticking probability ~20 %. When the sticking probability of the inhibitor is very high (Fig. 7.5b and c, e and f), the growth rate profile initially increases with trench depth due to depletion of the inhibitor and then, above a certain AR, decreases due to depletion of the precursor. Conversely, if the sticking probability is low, the consumption rate on the sidewalls is low and the inhibitor pressure does not decline rapidly with depth (Fig. 7.5h); the resulting growth profile is relatively conformal, but not superconformal. When the AR is small (Fig. 7.3c and curves for AR = 1 in Fig. 7.5), there is nearly no drop in either the precursor or inhibitor pressures, and growth is conformal.

7.3.3 A potential method for contamination-free superconconformal growth by using two precursors.

With the aid of consumable inhibitors, the growth may be superconformal, however, the films are contaminated by elements from inhibitor molecules. Here, the cobalt film is contaminated by vanadium, and presumably carbon and nitrogen, which cause the degradation of electrical performance.

A possible solution is to replace the inhibitor molecule with another precursor that can deposit the same film (here, cobalt precursors other than $Co_2(CO)_8$). The equations for describing this process are almost identical to the case with a consumable inhibitor, except that the growth rate is determined by a sum from two precursors, not one. From first-order Langmuirian approximation, the equations are:

$$\frac{d^2P_A}{dz^2} = Ck_r^A\theta_A = Ck_A^r\frac{K_AP_A}{K_AP_A + K_BP_B + 1},$$

$$\frac{d^2P_B}{dz^2} = Ck_r^B\theta_B = Ck_B^r\frac{K_BP_B}{K_AP_A + K_BP_B + 1},$$

$$\text{and } GR = k_r^A\theta_A + k_r^B\theta_B,$$

where C is a function of temperature, trench dimension and molecular mass. Note that the only difference with the case of consumable inhibitors is the definition of GR. And we neglect the interaction between these two molecules except for the competition for adsorption sites. This means k_r^A is independent of precursor B and k_r^B is independent of precursor A.

One precursor (say precursor B) needs to cover most of the surface (large K_B) but have a relatively low growth rate (small k_B^r), so it behaves in effect as a growth inhibitor. Conversely, precursor A has small K_A but relatively high k_A^r. In the presence of B, growth from A will be suppressed. Only when B is depleted on sidewalls, growth from A will speed up. To demonstrate the feasibility of the idea, we assume that two precursors follow Langmuir reaction mechanism and obey curves in Fig. 7.6a and 7.6b, respectively. Pressure for precursor A is chosen as 2 mTorr and pressure for B is 0.03 mTorr. The process from precursor A is transport limited (constant sticking probability) while process from B is reaction limited.

To calculate the growth rate profile, both molecules are assumed to have the same molecular mass at 300 g/mol, which is a reasonable value (the mass for $Co_2(CO)_8$ is 342 g/mol). As C is proportional to the square root of the weight, the difference between molecular weight are less significant to C. The atomic density is assumed as 10^{16} / nm for a 1-nm film (the value for cobalt is 1.1×10^{16} / nm). k_A^r and k_B^r are chosen so precursor A and B have the growth rate profiles shown in Fig. 7.6c and d, respectively. Note that growth rate is much higher for A though surface coverage is small ($k_A^r \gg k_B^r$).

Growth from A or B alone is not conformal in the trench due to loss of precursors on the sidewalls. However, when processed with 2 mTorr precursor A and 0.03 mTorr precursor B, the growth is superconformal with a growth rate 4 times higher in the trench bottom (Fig. 7.6e). Most of the growth is contributed from A. Growth from B is slow although its surface coverage is high. Because $K_A P_A \ll K_B P_B$ and $1 \ll K_B P_B$, θ_A is approximately proportional to $\frac{P_A}{P_B}$ while θ_B is relatively stable. Thus, the pressure B plays a key role in determining the growth rate from A. As B depletes gradually in the trench, the growth rate from A increases and the total growth rate increases.

Fig. 7.7 shows how change of pressure A and B affect the growth rate profile in a trench with AR of 10. When the pressure of A is too low, growth contributed from A is small and

increase of the growth rate from A barely affects the total growth rate. The growth is sub-conformal due to depletion of B in this case (curve for 0.01 mTorr in Fig. 7.7a). As the pressure of A is increased, contribution from A increases and then growth is conformal or superconformal (curves for 0.1 and 2 mTorr in Fig. 7.7a). When the pressure is too high, $K_A P_A$ is comparable to or larger than $K_B P_B$, the rate change from the decreasing pressure of B is less significant ($\theta_A \propto \frac{P_A}{P_B}$ does not hold), and thus, the growth is less superconformal (curve for 0.1 mTorr in Fig. 7.7a).

Likewise, when pressure of B is too low, the inhibition effect is not strong enough and A is depleted quickly, leading to sub-conformal growth (curve for 0.001 mTorr in Fig. 7.7b). As the pressure of B increases, growth from A is inhibited and depleted slower in the trench. The growth is conformal or superconformal (curves for 0.004 and 0.03 mTorr in Fig. 7.7b). However, when pressure of B is too high, growth contributed from B is dominant (increase of growth rate from A contributes little to the total growth rate), and the growth is less superconformal (curve for 0.1 mTorr in Fig. 7.7b). *In short, for precursor A with small K_A and large k_A^r, the pressure is chosen so that the precursor is still in linear regime of Langmuir isotherm ($K_A P$ is small), and contributes most of the growth rate. Meanwhile, for precursor B with large K_B and small k_B^r, the pressure is chosen so inhibition is neither too weak nor too strong.* Note that this approach affords the possibility of *perfectly* conformal growth, which is a highly desirable outcome in many cases that do require complete filling.

A good precursor combination has not been found yet. We examine the growth of cobalt with $Co_2(CO)_8$ and CCTBA. At 250 °C, films grown by 0.03 mTorr $Co_2(CO)_8$ and < 10^{-6} Torr CCTBA is sub-conformal (Fig. 7.8a) because $Co_2(CO)_8$ is depleted fast on the sidewalls. At lower temperature (120 °C), the growth appears to be slightly superconformal (Fig. 7.8b), however, CCTBA does not grow cobalt at 120 °C. CCTBA is simply a consumable inhibitor in this case and incorporated in the film as partially decomposed molecules, and thus the film quality is compromised (resistivity is ~ 300 μΩ·cm), presumably with carbon and oxygen contaminations.

This idea has been demonstrated for the growth of alloy films, i.e., when the two precursors deposit different materials. For example, $Hf_{1-x}V_xB_y$ alloy films are grown at 220 °C,

using 0.3 mTorr $Hf(BH_4)_4$ and 0.002 mTorr TDMAV. Note that, due to the higher temperature, TDMAV acts as a precursor. The growth is superconformal leading to trench filling (Fig. 7.9).

7.4 Conclusion

We demonstrate that superconformal growth of cobalt films from $Co_2(CO)_8$ can be obtained by using a consumable inhibitor. Growth from $Co_2(CO)_8$ at 70 °C is not conformal in the absence of a growth inhibitor. When a co-flow of TDMAV is added, the growth rate on the exposed surface declines from 2.7 to 0.25 nm/min. In a deep trench, TDMAV is progressively consumed on the sidewalls, and the growth is superconformal. The coating profile is V-shaped with an outwards taper angle of 4° on each side, which affords defect-free trench fill. A diffusion-reaction model explain why consumable inhibitors with high sticking probability can render the growth superconformal; the sticking coefficient of TDMAV is found to be ~ 20 %. The films grown in the presence of TDMAV contain 6 % of vanadium and the resistivity is high at 125 μΩ·cm. A similar approach using two precursors that deposit the same film, but with very different rates of adsorption and reaction, is predicted to afford contamination-free superconformal growth.

7.5 Figures

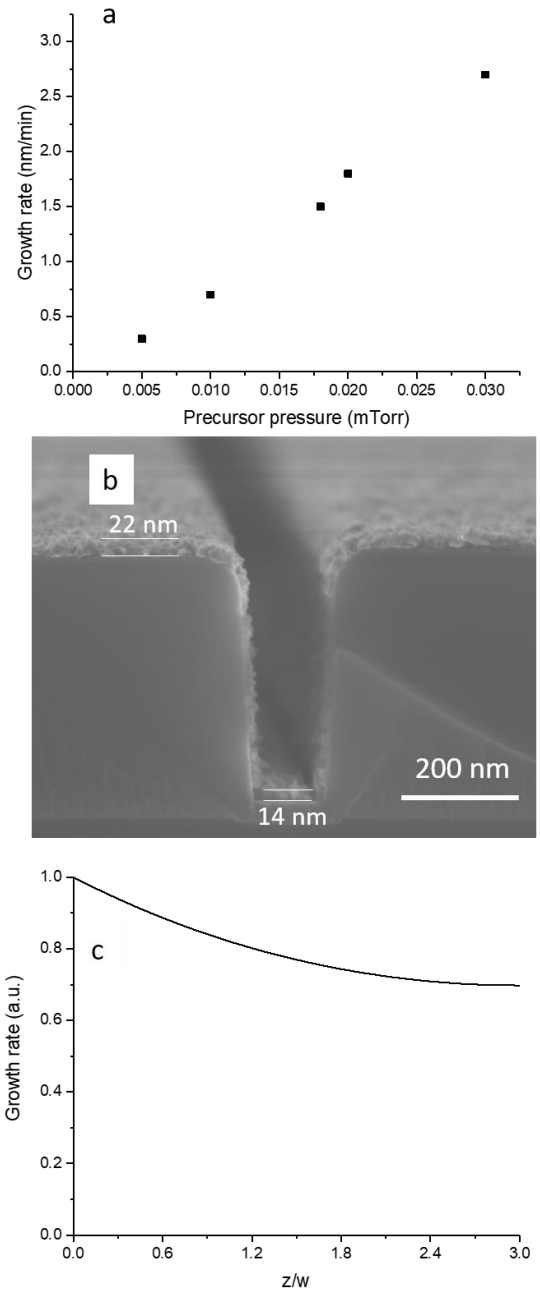

Figure 7.1. a) Plot of growth rate of cobalt vs. precursor pressure; b) cross-section SEM image of a trench coated with a cobalt film. The pressure of $Co_2(CO)_8$ is 0.02 mTorr. c) calculated growth rate profile with a constant sticking probability of 9 % in a trench with AR of 3. The growth temperature is 70 °C.

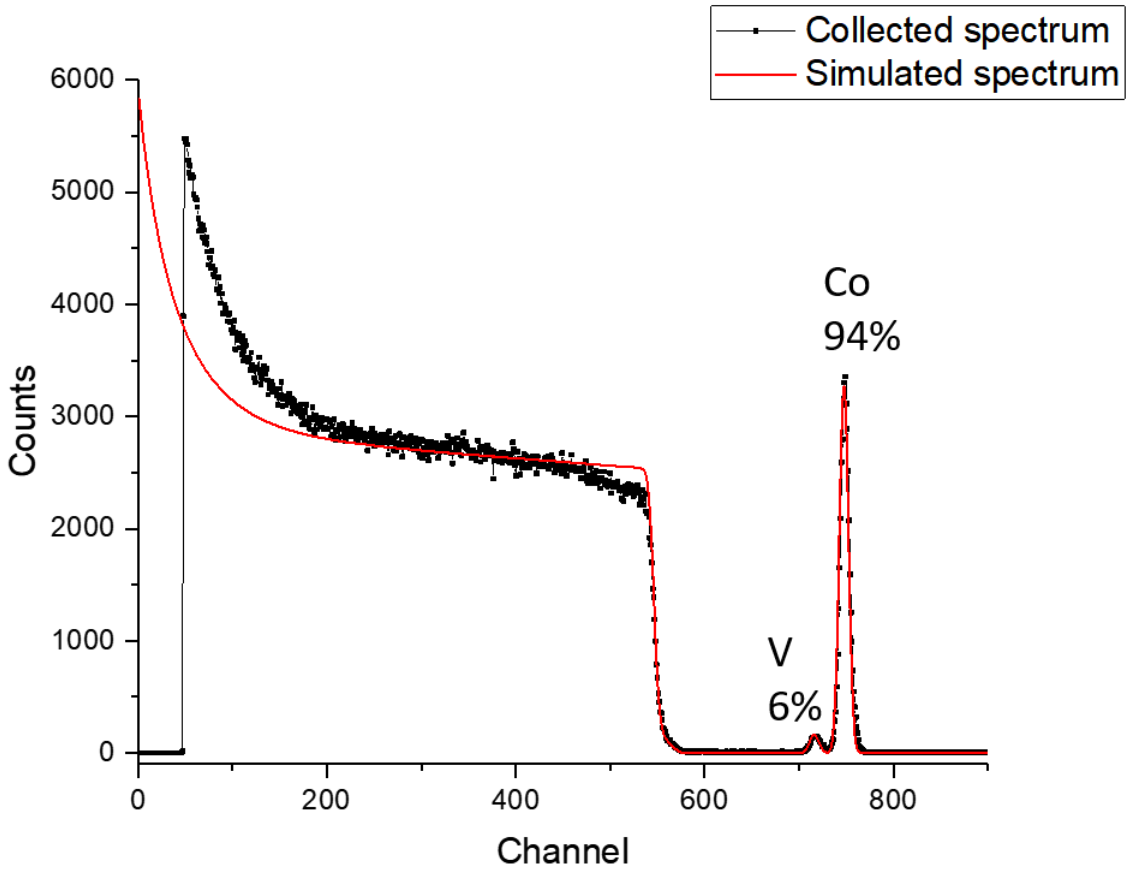

Figure 7.2. RBS spectrum of a cobalt film grown with 0.03 mTorr $Co_2(CO)_8$ and TDMAV on a planar Si substrate at 70 °C.

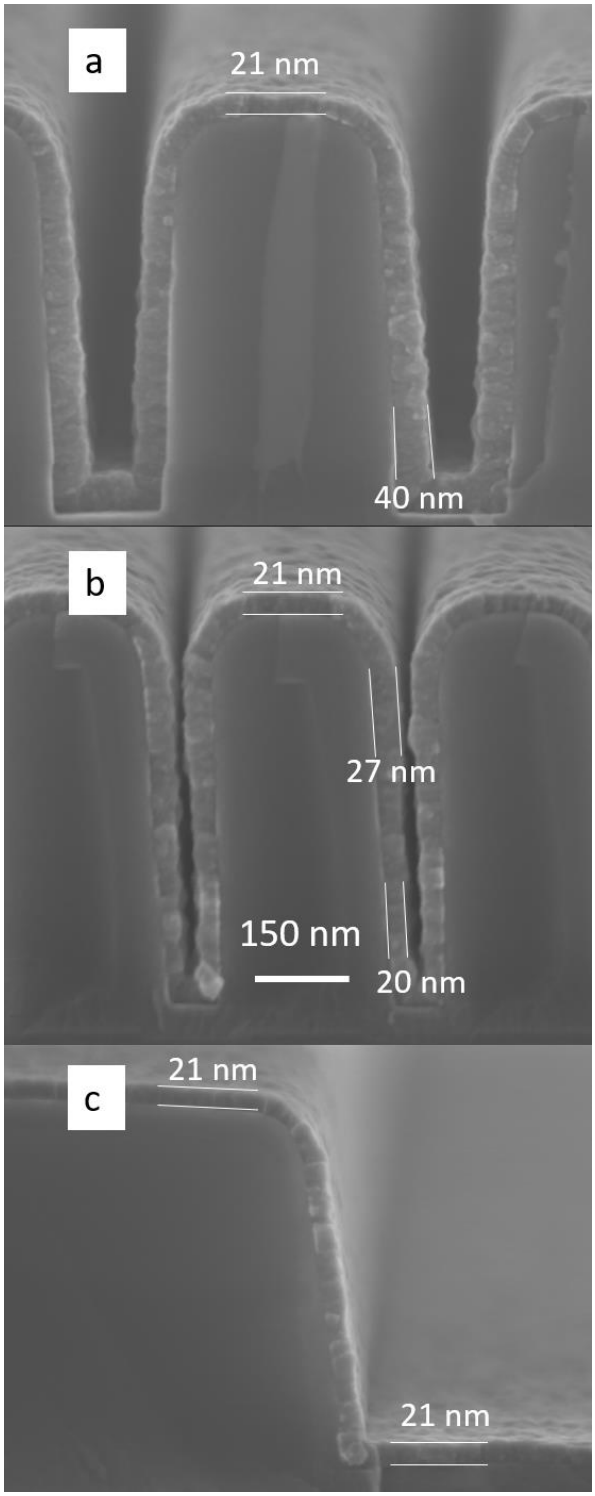

Figure 7.3. Cross-section SEM images of trenches coated with cobalt films from $Co_2(CO)_8$ in the presence of TDMAV, in trenches with various AR. The pressure of $Co_2(CO)_8$ is 0.03 mTorr. All images are collected from one sample.

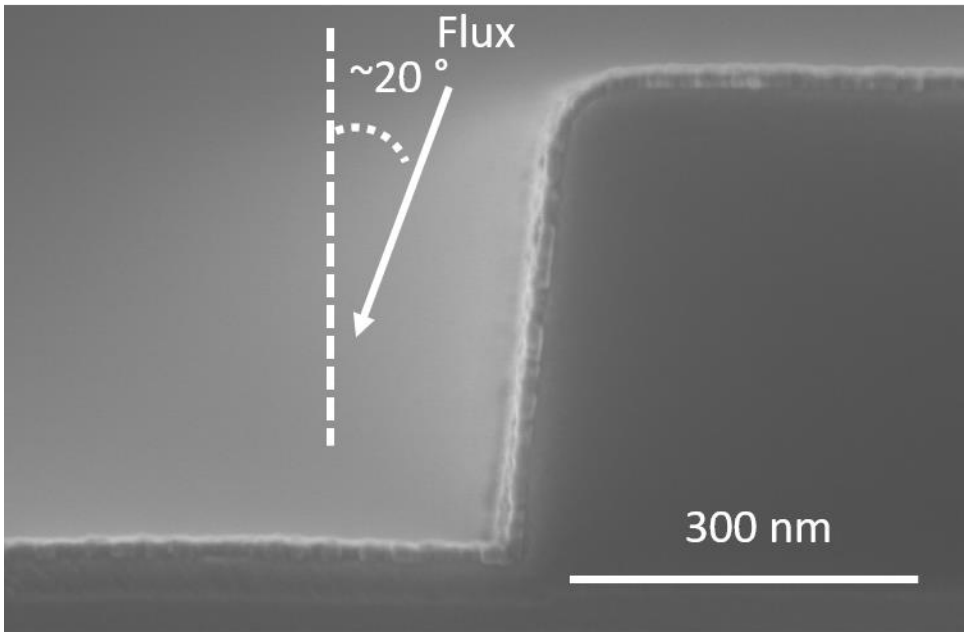

Figure 7.4. Cross-section SEM image of a trench with a cobalt film grown with the substrate tilted to an angle of 20° to incidence flux of $Co_2(CO)_8$ and TDMAV.

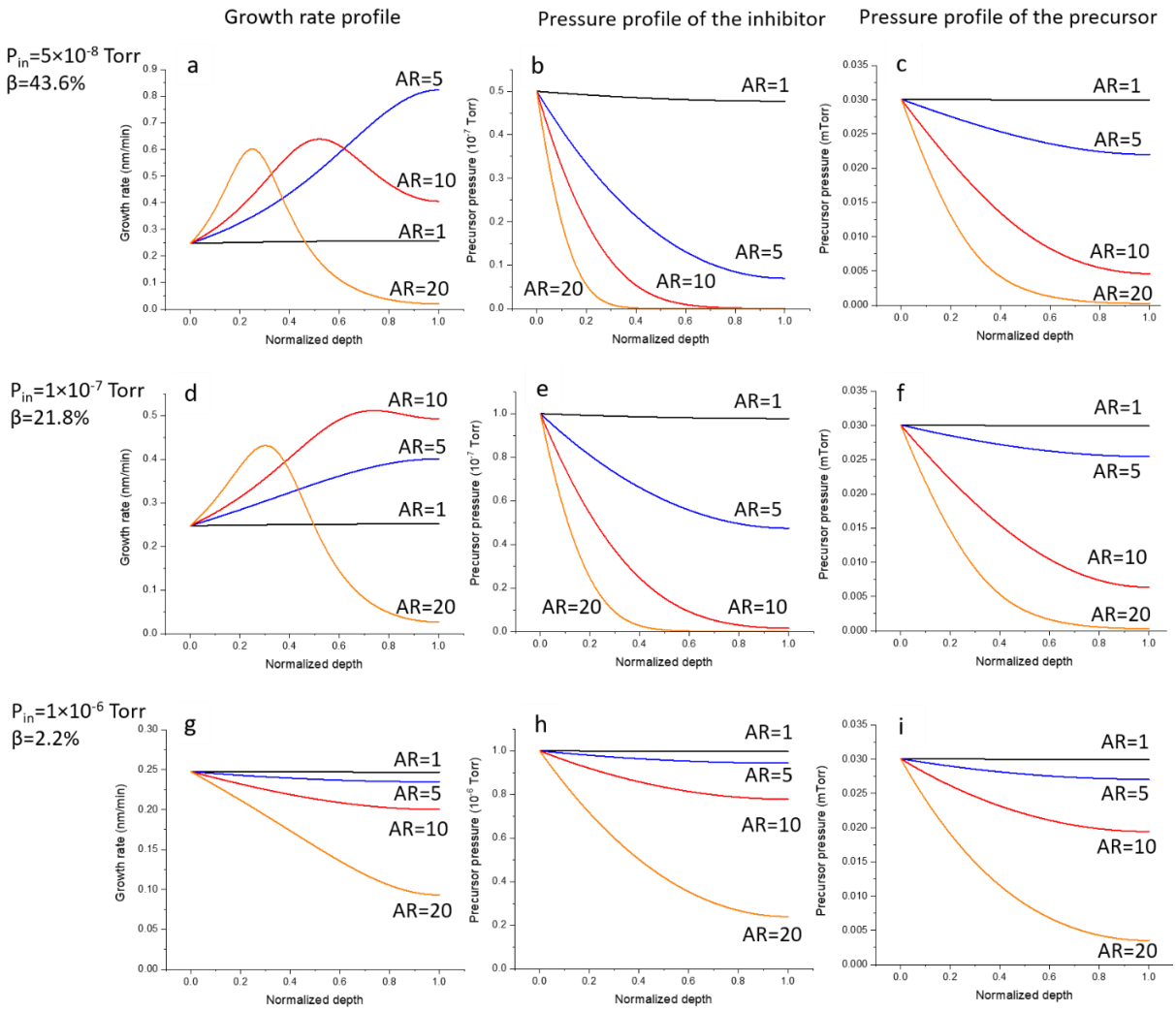

Figure 7.5. Calculated growth rate profiles (a, d, g), pressure profiles of inhibitor (b, e, h) and precursor (c, f, i). Note that normalized depth is used here, however, all profiles depend only on AR, not trench depth and trench width independently. β is the sticking coefficient of TDMAH at trench top. See text for details.

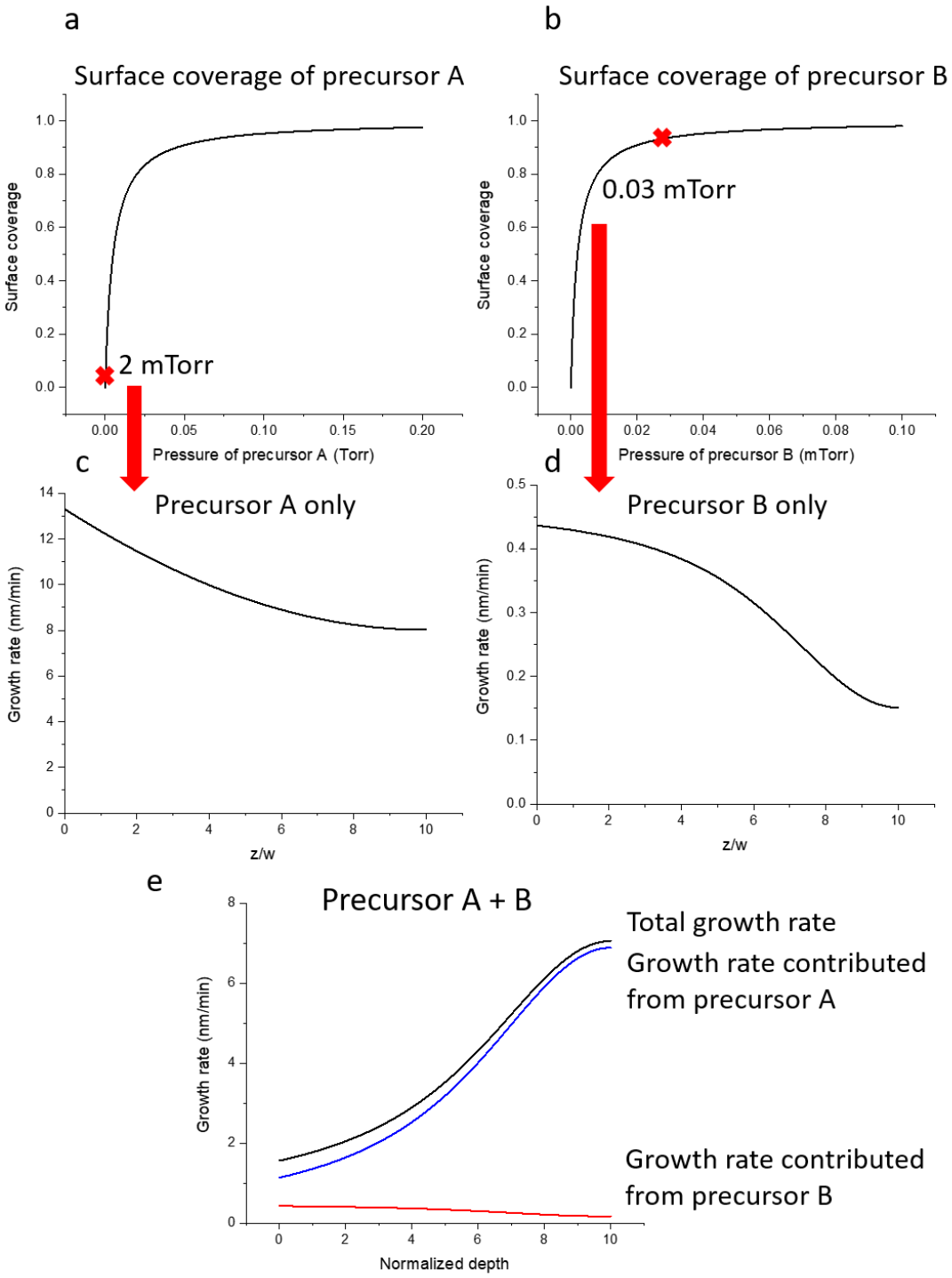

Figure 7.6. Calculated surface coverage of precursor A (a) and B (b) assuming Langmuir isotherm. Calculated growth rate profiles when only 2 mTorr of precursor A is flowed (c) and 0.03 mTorr of precursor B is flowed (d) in a trench with AR of 10. Calculated growth rate profile for a coflow of 2 mTorr of precursor A and 0.03 mTorr of precursor B (e). See text for details.

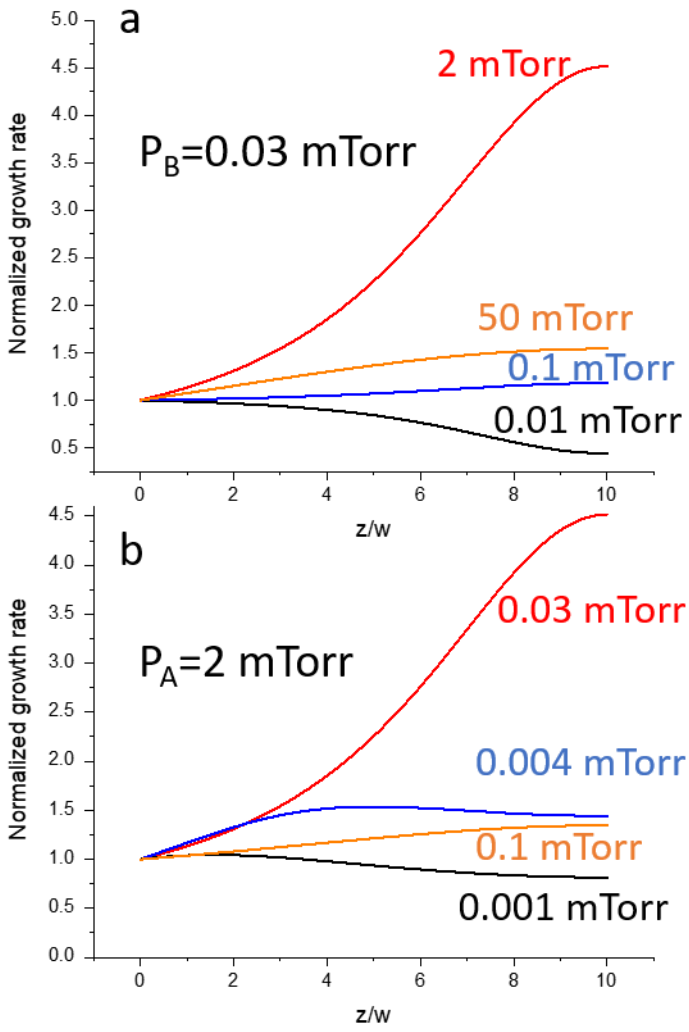

Figure 7.7. Calculated growth rate profiles for a trench with AR of 10, for various pressures of precursor A and precursor B. See text for details.

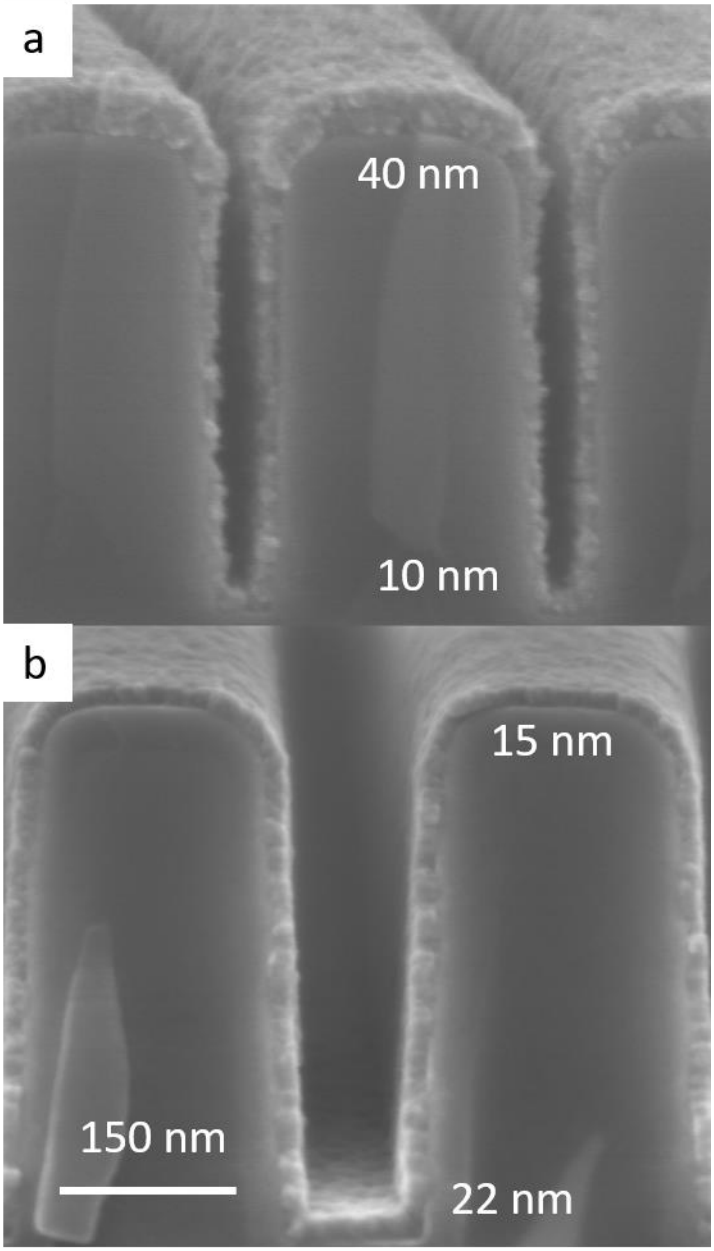

Figure 7.8. Cross-section SEM images of trenches coated with cobalt films from $Co_2(CO)_8$ and CCTBA at 250 °C (a) and 120 °C (b).

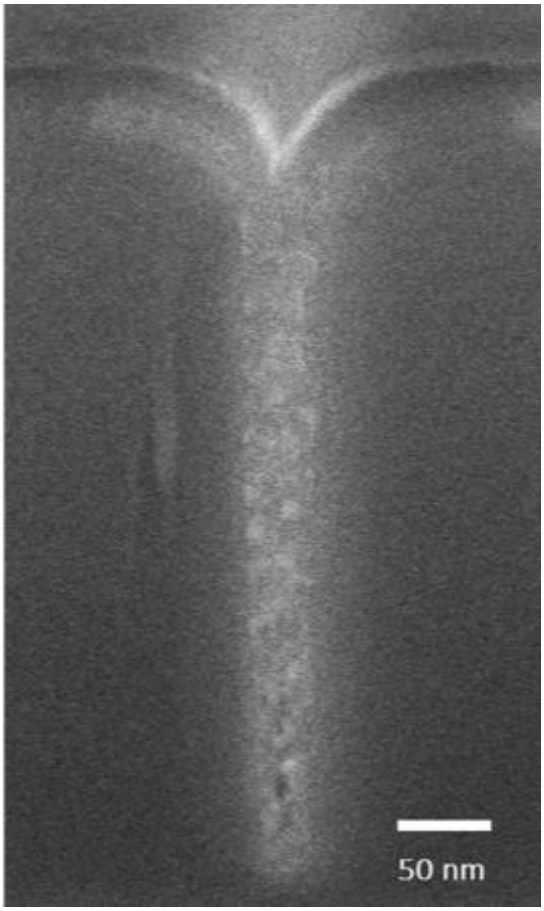

Figure 7.9. Cross-section SEM images of trenches coated with a $Hf_{1-x}V_xB_y$ alloy film from $Hf(BH_4)_4$ and TDMAV at 250 °C.

7.6 References

1. M. H. van der Veen, K. Vandersmissen, D. Dictus, S. Demuynck, R. Liu, X. Bin, P. Nalla, A. Lesniewska, L. Hall, K. Croes, L. Zhao, J. Bommels, A. Kolics, Z. Tokei, and Ieee, "Cobalt bottom-up contact and via prefill enabling advanced logic and dram technologies," *2015 IEEE International Interconnect Technology Conference and 2015 IEEE Materials for Advanced Metallization Conference***,** 25-7 (2015).

2. M. Nandakumar, A. Chatterjee, S. Sridhar, K. Joyner, M. Rodder, and I. Chen, "Shallow trench isolation for advanced ulsi cmos technologies," 1998, p. 133-6. [DOI: 10.1109/IEDM.1998.746297]

3. R. W. Johnson, A. Hultqvist, and S. F. Bent, "A brief review of atomic layer deposition: From fundamentals to applications," *Materials Today* **17,** 236-46 (2014).

4. T. K. Talukdar, S. Liu, Z. Zhang, F. Harwath, G. S. Girolami, and J. R. Abelson, "Conformal mgo film grown at high rate at low temperature by forward-directed chemical vapor deposition," *Journal of Vacuum Science & Technology A* **36,** 051504 (2018).

5. T. K. Talukdar, W. B. Wang, G. S. Girolami, and J. R. Abelson, "Superconformal coating and filling of deep trenches by chemical vapor deposition with forward-directed fluxes," *Journal of Vacuum Science & Technology A* **36,** 051513 (2018).

6. R. Abdolvand, H. Johari, G. K. Ho, A. Erbil, and F. Ayazi, "Quality factor in trench-refilled polysilicon beam resonators," *Journal of Microelectromechanical Systems* **15,** 471-8 (2006).

7. H. Schenk, P. Dürr, D. Kunze, H. Lakner, and H. Kück, "A resonantly excited 2d-micro-scanning-mirror with large deflection," *Sensors and Actuators A: Physical* **89,** 104-11 (2001).

8. C. C. Chen, I. C. Kao, H. C. Kuo, and H. J. Chien, "Studying of physical characteristics and optimizing of gap filling for tungsten," *Materials Science in Semiconductor Processing* **14,** 235-40 (2011).

9. A. Kubo, "An sio2 film deposition technology using tetraethylorthosilicate and ozone for interlayer metal dielectrics," *Journal of The Electrochemical Society* **143,** 1769 (1996).

10. X. Lin, X. Ma, and J. He, "Void-filling and loss reduction in pecvd silica waveguide devices using boron–germanium codoped upper cladding," *IEEE Photonics Technology Letters* **22,** 1491-3 (2010).

11. W. B. Wang, N. N. Chang, T. A. Codding, G. S. Girolami, and J. R. Abelson, "Superconformal chemical vapor deposition of thin films in deep features," *Journal of Vacuum Science & Technology A* **32,** 051512 (2014).

12. Y. Au, Y. Lin, and R. G. Gordon, "Filling narrow trenches by iodine-catalyzed cvd of copper and manganese on manganese nitride barrier/adhesion layers," *Journal of The Electrochemical Society* **158,** D248-D53 (2011).

13. W. B. Wang and J. R. Abelson, "Filling high aspect ratio trenches by superconformal chemical vapor deposition: Predictive modeling and experiment," *Journal of Applied Physics* **116,** 194508 (2014).

14. Y. Yang, "Chemical vapor deposition of metal diboride and metal oxide thin films from borohydride-bonded precursors," Thesis, University of Illinois at Urbana-Champaign, 2007.

15. S.-Q. Wang, "Barriers against copper diffusion into silicon and drift through silicon dioxide," *MRS Bulletin* **19,** 30-40 (2013).

16. J. Lee, H. J. Yang, J. H. Lee, J. Y. Kim, W. J. Nam, H. J. Shin, Y. K. Ko, J. G. Lee, E. G. Lee, and C. S. Kim, "Highly conformal deposition of pure co films by mocvd using co-2(co)(8) as a precursor," *Journal of the Electrochemical Society* **153,** G539-G42 (2006).

17. S. L. Zhejun Zhang, Gregory S. Girolami, John R. Abelson, (2020).

18. Z. V. Zhang, S. Liu, G. S. Girolami, and J. R. Abelson, "Area-selective chemical vapor deposition of cobalt from dicobalt octacarbonyl: Enhancement of dielectric-dielectric selectivity by adding a coflow of nh3," *Journal of Vacuum Science & Technology A* **38,** 033401 (2020).

19. E. Mohimi, Z. V. Zhang, J. L. Mallek, S. Liu, B. B. Trinh, P. P. Shetty, G. S. Girolami, and J. R. Abelson, "Low temperature chemical vapor deposition of superconducting vanadium nitride thin films," *Journal of Vacuum Science & Technology A* **37,** 031509 (2019).

20. X. Wang, Z. Guo, Y. Gao, and J. Wang, "Atomic layer deposition of vanadium oxide thin films from tetrakis(dimethylamino)vanadium precursor," *Journal of Materials Research* **32,** 37-44 (2016).

21. S. Jayaraman, Y. Yang, D. Y. Kim, G. S. Girolami, and J. R. Abelson, "Hafnium diboride thin films by chemical vapor deposition from a single source precursor," *Journal of Vacuum Science & Technology A* **23,** 1619-25 (2005).

22. S. Jayaraman, E. J. Klein, Y. Yang, D. Y. Kim, G. S. Girolami, and J. R. Abelson, "Chromium diboride thin films by low temperature chemical vapor deposition," *Journal of Vacuum Science & Technology A* **23,** 631-3 (2005).

23. A. E. Kaloyeros, Y. Pan, J. Goff, and B. Arkles, "Editors' choice—review—cobalt thin films: Trends in processing technologies and emerging applications," *ECS Journal of Solid State Science and Technology* **8,** P119-P52 (2019).

24. D. X. Ye, S. Pimanpang, C. Jezewski, F. Tang, J. J. Senkevich, G. C. Wang, and T. M. Lu, "Low temperature chemical vapor deposition of co thin films from co2(co)8," *Thin Solid Films* **485,** 95-100 (2005).

25. T. K. Talukdar, G. S. Girolami, and J. R. Abelson, "Seamless fill of deep trenches by chemical vapor deposition: Use of a molecular growth inhibitor to eliminate pinch-off," *Journal of Vacuum Science & Technology A* **37,** 021509 (2019).

CHAPTER 8

FUTURE POSSIBILITIES AND PRELIMINARY RESULTS

8.1 ASD of nucleation layer

ASD has mostly been reported for metal on metal (i.e., no growth on non-metallic surfaces) or oxide on oxide (i.e., no growth on metallic surfaces). Mixed metallic and non-metallic combination of film and substrate have been reported, but in general, such combinations are extremely challenging for ASD.

In chapter 2, we report an ASD process that can grow cobalt films on basic oxide but not on acidic oxide. This process may not be easy to extend to other material systems because we have hypothesized, ASD depends on the particular intermediates formed by dissociation of the $Co_2(CO)_8$ precursor, and the reactions of ammonia with this intermediate. However, cobalt films may be used as a nucleation layer for CVD of other materials. Via this route it is possible to obtain dielectric-dielectric selectivity for other metallic films: first, cobalt film is are selectively grown on the basic oxide; then the desired film is grown on cobalt by a traditional metal-on-metal process [1-3].

SAMs with ligands like thiol can block metal surface and prevent nucleation. However, in many cases metal deposition on oxide also suffers from the problem of slow nucleation in many cases [1,4-6]. Consequently, a metal-on-dielectric process is not well-established even with SAMs.

Adsorption of TDMA-M molecules provides a good nucleation layer (Chapter 3 and 4). The adsorption of TDMA-M typically requires either a hydroxylated oxide or metal surface [7-10]. TDMA-M may not adsorb well when metal is terminated by specific SAMs, e.g., with a tail of CH_3 group [11]. A metal-on-dielectric process could possibly be achieved by following steps: 1) metal surface is selectively covered by SAMs; 2) the oxide surface is selectively covered by adsorbed TDMA-M; 3) growth of the desired films occurs only on the TDMA-M adsorbed surface.

8.2 Nucleation enhancement by TDMA-M molecules

In Chapter 3 and chapter 4, the mechanism for nucleation enhancement on SiO_2 from TDMA-M molecules is not well established yet, thus, it is not easy to discover another substance that acts like TDMA-M, nor to provide guidelines for other systems. Preliminary experiments illustrate the strong differences between candidate molecules. We trialed TDMA-Si as the pretreatment molecule but it seemed not to adsorb well at our process temperature. Trimethylaluminum (TMA) is a great ALD precursor and it was discovered to improve nucleation for Pt deposition on oxides[12]. TMA molecules adsorb well on the surface at 70 °C, however, there is no evidence that TMA layer can enhance nucleation of cobalt from $Co_2(CO)_8$. Hexacarbonyl(3,3-dimethyl-1-butyne)dicobalt (CCTBA) is an ALD precursor for cobalt, and it adsorbs well on the surface. However, we find no evidence that CCTBA can enhance nucleation. A working hypothesis is that the molecule must contain an early-transition metal (like Ti, V or Hf) but ligands may also play an important role in precursor adsorption and reaction. For future work, other molecules like $Ti(Cl)_4$, or titanium butoxide could be trialed to investigate the dependence of the nucleation behavior on ligands.

8.3 Formation of MgAu and Mg_2Si in reaction of precursor with substrates

MgAu is an intermetallic compound that may be used as electrodes and typically is synthesized by reacting Mg with gold by electrodeposition [13,14]. Mg_2Si is an intermetallic compound with exhibits a high melting temperature, low density, high hardness and low thermal expansion [15]. It is also a semiconductor with narrow bandgap (0.3 ~ 0.6 eV) and has potential in photovoltaic and thermoelectric applications [16]. I discovered that the phase of Mg_2Si or MgAu (Fig. 1a and Fig. 2a) can form when Si or gold substrate is exposed to magnesium N, N-dimethylaminodiboranate ($Mg(DMADB)_2$) at 350 °C. From Auger electron spectroscopy (Fig. 1 b), the sample of Mg_2Si contains more carbon, oxygen and boron on the surface than in depth. Boron and carbon are originated from decomposition of $Mg(DMADB)_2$, and oxygen is presumably from air exposure or oxidation by background water during growth. Note MgO does react with Si to generate Mg_2Si. The Mg concentration is relatively stable but very low (10 at. %), indicating the major composition is still Si. $Mg(DMADB)_2$ does not self-decompose to deposit Mg (with oxidation state of 0) on substrates (e.g., HfB_2) that cannot form a compound

with Mg. Thus, Mg_2Si is presumably grown by direct reaction between $Mg(DMADB)_2$ and Si. For the sample of MgAu, it affords mixed phases of gold and MgAu. For future work, optimization of process conditions, such as temperature and pressure, is required to obtain high-quality products. Also, a chamber with a better vacuum is needed to prevent oxidation.

8.4 Aluminum nanorods

The unique optical and electronic properties from metal nanorods make them useful for applications in optoelectronics, photovoltaics, sensing and imaging [19,20]. Aluminum supports UV plasmon resonance, making it potentially a candidate for plasmonic applications. Synthesis of Al nanorods have been reported by photolithography [21] and by decomposition of triisobutyl aluminum [19].

In preliminary work, CVD of nanorods (FIG. 8.3) are synthesized on (100) Si substrate at 250 °C from trimethylamine alane (0.06 mTorr) with a coflow of ammonia (0.5 mTorr) and hafnium borohydride (0.2 mTorr).

For future work, study on crystallinity and composition of nanorods is required. Also, we need to figure out the role of individual processing molecules (trimethylamine alane, ammonia and hafnium borohydride) in nanorod synthesis so diameter, length, and density of nanorods can be well controlled.

8.5 Figures

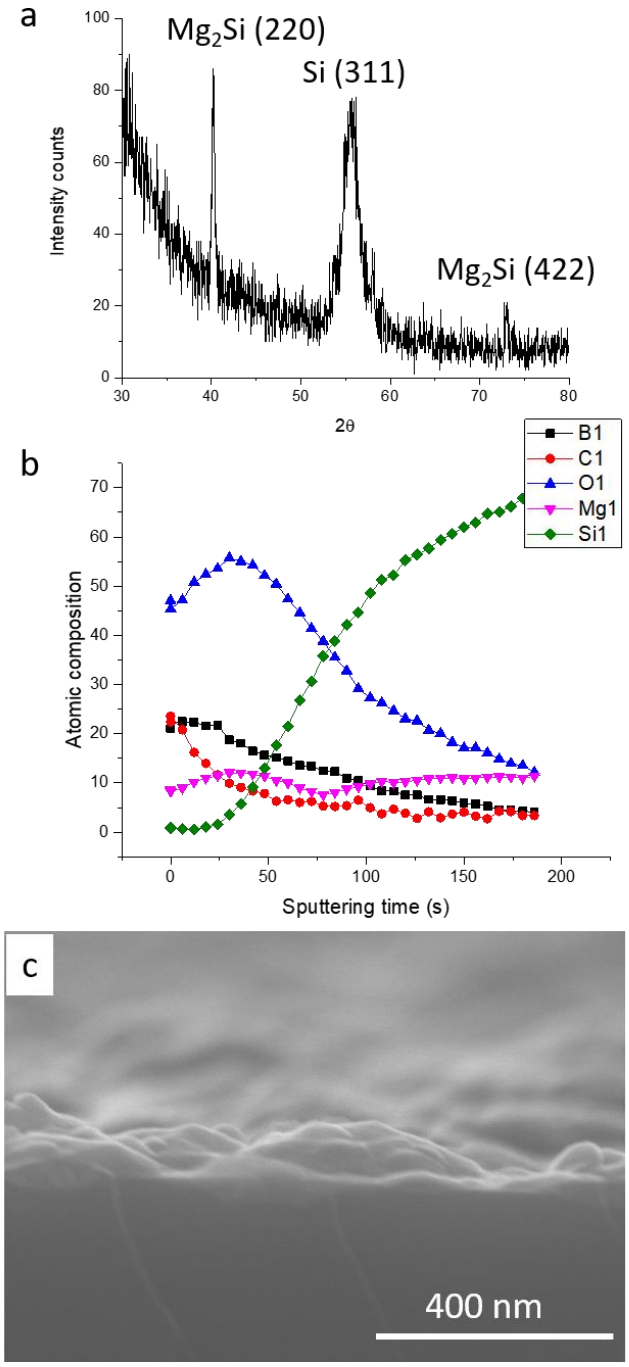

Figure 8.1. a) XRD pattern at grazing angle (1°), b) AES sputter depth profile, and c) cross-section SEM image of the Mg_2Si sample.

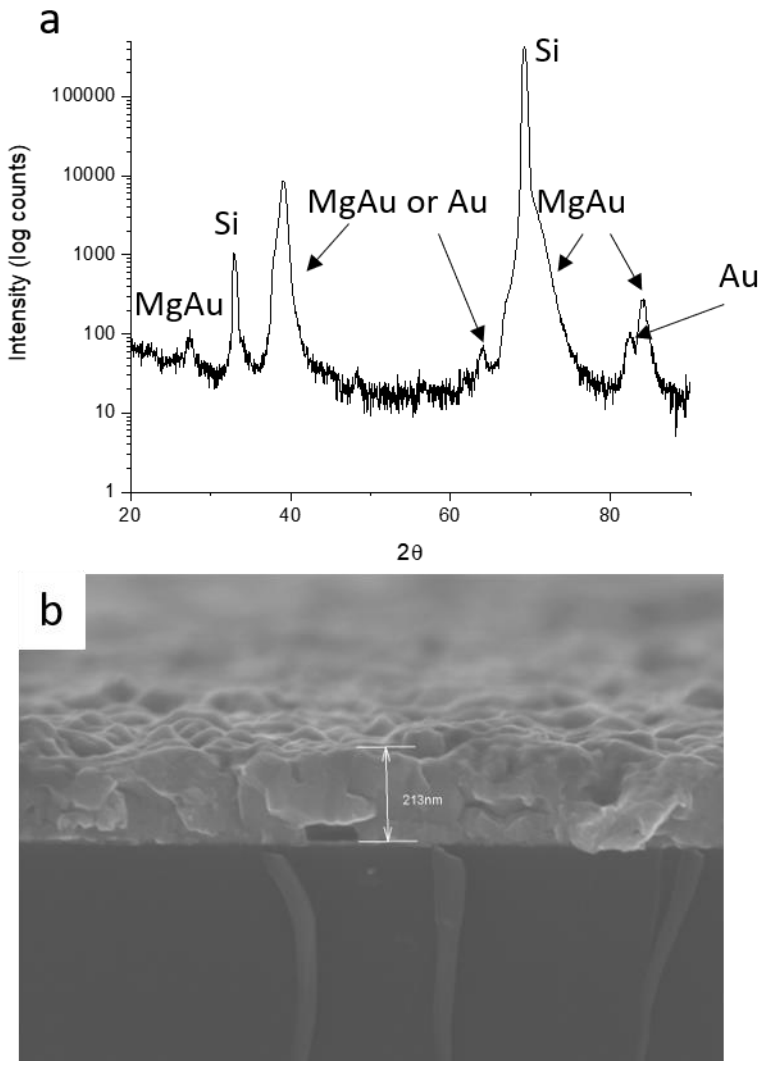

Figure 8.2. a) XRD pattern and b) cross-section SEM image of the MgAu sample. The XRD pattern is collected using omega-2theta method.

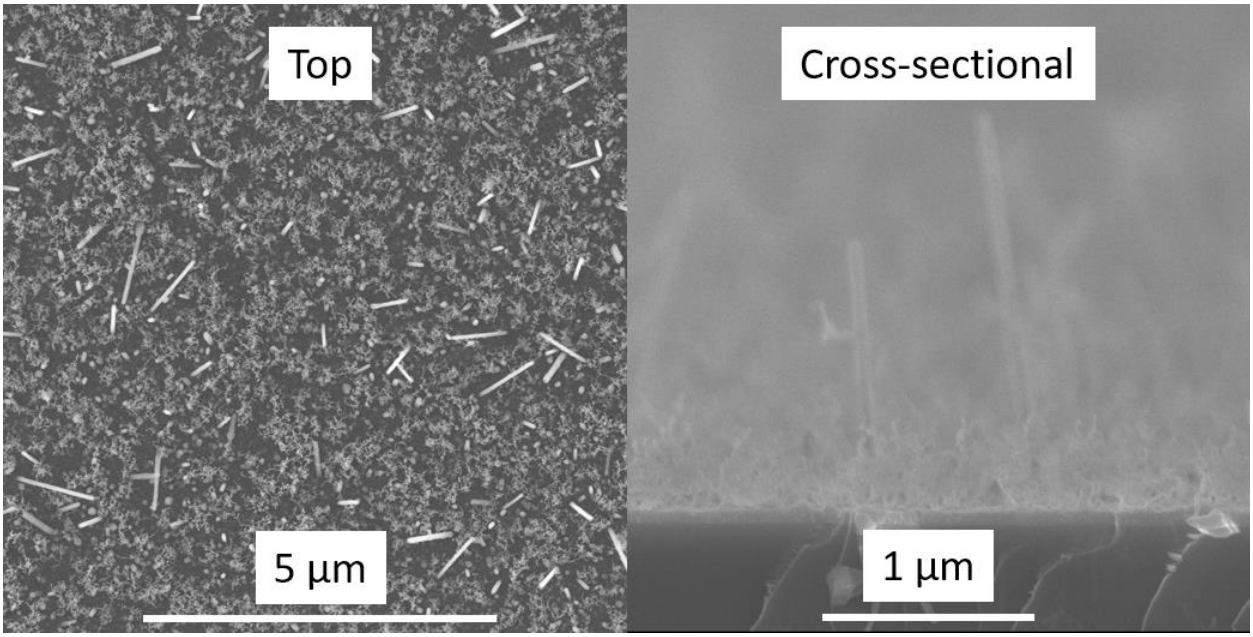

Figure 8.3. Top and cross-sectional views of nanorods

8.6 References

1. S. Babar, E. Mohimi, B. Trinh, G. S. Girolami, and J. R. Abelson, "Surface-selective chemical vapor deposition of copper films through the use of a molecular inhibitor," *Ecs Journal of Solid State Science and Technology* **4,** N60-N3 (2015).

2. J. Soethoudt, H. Hody, V. Spampinato, A. Franquet, B. Briggs, B. T. Chan, and A. Delabie, "Defect mitigation in area-selective atomic layer deposition of ruthenium on titanium nitride/dielectric nanopatterns," *Advanced Materials Interfaces* **6,** 1900896 (2019).

3. W. Xie and G. N. Parsons, "Thermal atomic layer etching of metallic tungsten via oxidation and etch reaction mechanism using o2 or o3 for oxidation and wcl6 as the chlorinating etchant," *Journal of Vacuum Science & Technology A* **38,** 022605 (2020).

4. A. E. Kaloyeros, Y. Pan, J. Goff, and B. Arkles, "Editors' choice—review—cobalt thin films: Trends in processing technologies and emerging applications," *ECS Journal of Solid State Science and Technology* **8,** P119-P52 (2019).

5. Z. V. Zhang, S. Liu, G. S. Girolami, and J. R. Abelson, "Area-selective chemical vapor deposition of cobalt from dicobalt octacarbonyl: Enhancement of dielectric-dielectric selectivity by adding a coflow of nh3," *Journal of Vacuum Science & Technology A* **38,** 033401 (2020).

6. S. L. Zhejun Zhang, Gregory S. Girolami, John R. Abelson, "Ultra-smooth cobalt films on sio2: Cvd using a nucleation promoter and a growth inhibitor," *In preparation*.

7. S. VLAANDEREN, "The use of substrate biasing during plasma-enhanced atomic layer deposition of tin for area-selective deposition," Thesis, EINDHOVEN UNIVERSITY OF TECHNOLOGY, 2019.

8. Q. Xie, Y.-L. Jiang, C. Detavernier, D. Deduytsche, R. L. Van Meirhaeghe, G.-P. Ru, B.-Z. Li, and X.-P. Qu, "Atomic layer deposition of tio2 from tetrakis-dimethyl-amido titanium or ti isopropoxide precursors and h2o," *Journal of Applied Physics* **102,** 083521 (2007).

9. X. Liu, S. Ramanathan, and T. E. Seidel, "Atomic layer deposition of hafnium oxide thin films from tetrakis(dimethylamino)hafnium (tdmah) and ozone," *MRS Proceedings* **765,** D3.8 (2011).

10. X. Wang, Z. Guo, Y. Gao, and J. Wang, "Atomic layer deposition of vanadium oxide thin films from tetrakis(dimethylamino)vanadium precursor," *Journal of Materials Research* **32,** 37-44 (2016).

11. P. F. Ma, A. Dube, A. S. Killampalli, and J. R. Engstrom, "A supersonic molecular beam study of the reaction of tetrakis(dimethylamido)titanium with self-assembled alkyltrichlorosilane monolayers," *The Journal of Chemical Physics* **125,** 034706 (2006).

12. Y. Hwang, B. M. Nguyen, and S. A. Dayeh, "Atomic layer deposition of platinum with enhanced nucleation and coalescence by trimethylaluminum pre-pulsing," *Applied Physics Letters* **103,** 263115 (2013).

13. V. S. Cvetković, N. Jovićević, J. S. Stevanović, M. G. Pavlović, N. M. Vukićević, Z. Stevanović, and J. N. Jovićević, "Magnesium–gold alloy formation by underpotential deposition of magnesium onto gold from nitrate melts," *Metals* **7,** 95 (2017).

14. Y.-F. Li, X.-Y. Kuang, S.-J. Wang, Y. Li, and Y.-R. Zhao, "Geometries, stabilities, and electronic properties of gold–magnesium (aunmg) bimetallic clusters," *Physics Letters A* **375,** 1877-82 (2011).

15. W. Gan, K. Wu, M. Zheng, X. Wang, H. Chang, and H.-G. Brokmeier, "Microstructure and mechanical property of the ecaped mg2si/mg composite," *Materials Science and Engineering: A* **516,** 283-9 (2009).

16. R. G. Morris, R. D. Redin, and G. C. Danielson, "Semiconducting properties of mg2si single crystals," *Physical Review* **109,** 1909-15 (1958).

17. T. K. Talukdar, S. Liu, Z. Zhang, F. Harwath, G. S. Girolami, and J. R. Abelson, "Conformal mgo film grown at high rate at low temperature by forward-directed chemical vapor deposition," *Journal of Vacuum Science & Technology A* **36,** 051504 (2018).

18. Y. Yang, "Chemical vapor deposition of metal diboride and metal oxide thin films from borohydride-bonded precursors," Thesis, University of Illinois at Urbana-Champaign, 2007.

19. B. D. Clark, C. R. Jacobson, M. Lou, J. Yang, L. Zhou, S. Gottheim, C. J. DeSantis, P. Nordlander, and N. J. Halas, "Aluminum nanorods," *Nano Letters* **18,** 1234-40 (2018).

20. V. S. Marangoni, J. Cancino-Bernardi, and V. Zucolotto, "Synthesis, physico-chemical properties, and biomedical applications of gold nanorods—a review," *Journal of biomedical nanotechnology* **12,** 1136-58 (2016).

21. M. W. Knight, N. S. King, L. Liu, H. O. Everitt, P. Nordlander, and N. J. Halas, "Aluminum for plasmonics," *ACS Nano* **8,** 834-40 (2014).